Experimental investigations of S=1/2 kagome magnets: the search for quantum spin liquids

Ross Harvey Colman

UCL

Degree of Doctor of Physical Chemistry

Declaration

I, Ross Harvey Colman, confirm that the work presented in this thesis is my own. Where information has been derived from other sources, I confirm that this has been indicated.

I wish to dedicate this thesis to all of the people
that have helped me to grow into the person I am today.
Particularly my Mother, Father, Brother and Sister.

Without the people I love, I would be nothing...

Abstract

The search for quantum spin liquids (QSL) is an enduring problem in condensed matter physics. The QSLs are a broad class of highly correlated ground states that feature large quantum fluctuations. The archetypal of which is the RVB (Resonating Valence Bond) ground state, proposed by Anderson to be the state from which the transition to unconventional superconductivity occurs in the high-Tc cuprates. Since the proposal over 20 years ago that a RVB ground-state may be observable in insulators, experimentalists have been searching for model materials to test the properties of such a ground-state. The geometric frustration of a kagome network of spins, coupled with the high weighting of quantum fluctuations of low spin-state ions is thought to provide the key conditions for such a state to occur. Research in the field has been hindered by the scarcity of materials displaying a kagome network of $S = \frac{1}{2}$ ions.

This thesis details efforts to broaden the library of candidate $S = \frac{1}{2}$ kagome materials, with the study of four new compounds: 'Mg-herbertsmithite', kapellasite, haydeeite and vesignieite. Synthetic conditions, detailed structural studies and preliminary magnetic characterizations of each material are given. While no currently known $S = \frac{1}{2}$ kagome magnets fully encapsulate the simplicity of the theoretical models, their deviations from ideality can be used as an opportunity to reveal how these perturbations can affect these exotic types of dynamic ground-state. Thereby providing new insight into this quickly expanding field of condensed matter physics.

Acknowledgements

First and foremost I must thank my principal supervisor Dr. Andrew Wills. For my entire time at UCL Andrew has had my best interests at heart. Both as a scientist and mentor Andrew's door has always been open: ready for scientific discussion, explanation or inspiration. Most importantly, Andrew has never been shy to criticise. Though frustrating at times, I would not have developed into the scientist that I am today without these criticisms: sometimes blunt, but always fair and well-reasoned.

My secondary supervisor, Dr. Desmond McMorrow, has also provided much needed inspiration and insight throughout my Ph.D. The background that Des has in physics has shed light on concepts foreign to most chemists, and without some of our discussions wading through the murky overlap between the physics and chemistry of frustrated magnetism would have been much more difficult.

A huge amount of thanks must also go to the other members of the Wills research group that have been and gone throughout my time at UCL. Both Drs. Amy Poole and Zoso Davies welcomed me into the group warmly when I first appeared on the steps and were always there to point me in the direction of the right textbook, paper or pub. Laura Fenner, with her tireless work ethic and meticulous attention to detail could only ever be a good influence on me. I particularly would like to thank her for talking me out of the many *stupid* ideas I had during the three years we worked together. She is the hardest working person that I have ever known, yet always had time to help me with a problem when I was stuck.

Dr. Ian Watts also played a particularly large part in my education at UCL. Whether it was a diffractometer, SQUID or PC, Ian could take it apart, tell you what's what, and put it back together with ease. Ian deserves great thanks for the small insights that rubbed off on me.

Alex Sinclair and David Boldrin must also get particularly special mentions here. Both of them worked closely with me as part of their undergraduate masters projects, and my 'Mg-herbertsithite' and vesigniete chapters, respectively, would not have been what they are without their help. I also want to take this opportunity to apologise for the large amount of washing-up I forced them into during their time in our labs, I hope it really was 'character building'.

From UCLs wider condensed matter community, Dr. Bob Aldus and Dr. Stuart Calder were always ready for a coffee and discussion. As physicists, their unexpected

questions about Jahn-Teller distortions, powder-grinding best-practices and the principles of“ ‘cellotape’ always kept me thinking. Special thanks also goes to Dr. Tom Fennell for his patience and guidance on my first neutron diffraction experiment at the ILL. I apologise Tom, for never having time to synthesise Spangolite.

Without a number of UCLs other students and postdocs my Ph.D. would not have been half as memorable. I wish to thank some of them for their friendship, kindness and help. In particular Drs. Charlie Dunnill and Caroline Knapp but without forgetting the other main member of ‘coffee club’ Paolo Melgari and the numerous temporary members (you know who you are). I would also like to thank the other students working in G19 throughout my time there, in particular Drs. Rosie Coates and Andy Kerridge as well as many others that came and went. The other students from office 310 and surrounding labs could not go without mention either, thank you all.

Without the large-scale facilities the majority of the work presented in this thesis would also not have been possible. During my time working at these facilities I met and was influenced by a large number of scientists. Of particular note are the instrument scientists that were always there to help, these include but are not limited to: Clemens Ritter and Jacques Olivier from instruments D2b and IN5, ILL; Pascal Manuel and Laurent Chapon from WISH, ISIS; and Simon Baker and Adrian Hillier from MUSR, ISIS.

A large number of collaborations were also started during my Ph.D. some of them fruitfull, some of them are still works in progress. I would particularly like to thank Dr. Fabrice Bert and Prof. Phillipe Mendels for collaborations involving μSR and NMR, and Dr. Bjorn Fåk for his work on the inelastic neutron diffraction spectrum of kapellasite.

There are many names that I have forgotten to mention, or just don’t have space for. These people I apologise to and thank.

Finally, it goes without saying that I could not have achieved any of this without funding from the EPSRC, and thank the ‘powers that be’ for paying me a student stipend.

Publications

The work presented in this thesis has been in part published in the following papers:

- Colman, R. H.; Ritter, C.; Wills, A. S. **Towards perfection: Kapellasite, $Cu_3Zn(OH)_6Cl_2$, a new model $S = \frac{1}{2}$ kagome antiferromagnet**, *Chem. Mater.* **2008**, *20*, 6897.
- Colman, R. H.; Sinclair, A.; Wills, A. S. **Comparisons between Haydeeite, α-$Cu_3Mg(OD)_6Cl_2$, and Kapellasite, α-$Cu_3Zn(OD)_6Cl_2$, Isostructural $S = \frac{1}{2}$ Kagome Magnets**, *Chem. Mater.* **2010**, *22*, 5774.
- Colman, R. H.; Sinclair, A.; Wills, A. S. **Magnetic and Crystallographic Studies of Mg-Herbertsmithite, gamma-$Cu_3Mg(OD)_6Cl_2$ A New $S = \frac{1}{2}$ Kagome Magnet and Candidate Spin Liquid**, *Chem. Mater.* **2011**, *23*, 1811.
- Colman, R.; Bert, F.; Boldrin, D.; Hillier, A.; Manuel, P.; Mendels, P.; Wills, A. **Spin dynamics in the $S = \frac{1}{2}$ kagome compound vesignieite, $Cu_3Ba(VO_5H)_2$**, *Phys. Rev. B* **2011**, *83*, 180416.

Contents

List of Tables

List of Figures

CHAPTER 1

Magnetism, Frustration and Spin-liquids

1.1. Introduction

This chapter introduces many of the fundamental concepts that underpin our understanding of magnetism. A number of magnetic exchange interactions will be discussed, before an overview is given of the wide variety of magnetically ordered ground-states that these interactions can induce. Different types of magnetic 'frustration' are also examined, along with their ability to suppress the transition to an ordered ground-state and to allow exotic types of order to occur. In particular, the highly frustrating geometries of several 2- and 3-dimensional lattices will be looked at and the important case of a spin-liquid ground-state on the kagome lattice will be introduced. With respect to this specific case, the reported properties of several model materials are considered. The remainder of this thesis is focussed on meeting the need for new model materials to experimentally characterise the exotic ground-state physics of the quantum-kagome lattice.

1.2. The origins of magnetism

Here we begin by addressing the question of how the *spin* of an ion arises at the atomic level. We can then follow this using thermodynamic arguments to the macroscopically observable properties of magnetic materials, deriving the Brillouin function of paramagnetic materials in an applied magnetic field, and the Curie law that follows from this. We conclude this section by considering the adjustments to the Curie law that must be made to reconcile a breakdown of the assumption of non-interacting spins, leading to the Curie-Weiss law. For a more complete discussion, the following texts were referred to during the writing of this section.[**1, 2, 3**]

1.2.1. The magnetic moment

When we discuss magnetism we regularly refer to the concept of a magnetic moment, μ. The moment is the fundamental object in magnetism and is most easily visualised

in terms of electron orbits. Orbiting electrons are loops of current and so give rise to a magnetic field, $\mathrm{d}\mu$, dependent on the area of the loop, $\mathrm{d}S$, and the magnitude of the current, I, given by

$$\mathrm{d}\mu = I\mathrm{d}S \tag{1.1}$$

If we consider the moment produced by a single electron orbiting the hydrogen nuclei, with charge $-e$, mass m_e and angular momentum $m_e Vr = \hbar$, we can define the SI unit of magnetic moment, one Bohr magneton, μ_B, as

$$|\mu_\mathrm{e}| = \pi r^2 I = -e\hbar/2m_\mathrm{e} \equiv -\mu_\mathrm{B} = -9.274 \times 10^{-24}\mathrm{Am}^2 \tag{1.2}$$

As well as the magnetic moment introduced by the electronic spin, orbital angular momentum can contribute to the total moment. This is most prominent in the 'f'-block ions, where orbital overlap between the unpaired-electron bearing $4f$ shells is minimal and the orbitals only weakly interact with the crystal field. In contrast, the contribution is relatively small in the transition metals where the $3d$ orbitals interact more strongly with the crystal (ligand) field. This interaction splits the otherwise degenerate orbitals, quenching orbital angular momentum. For heavy elements with large spin-orbit coupling the spin and orbital angular momentum quantum numbers, S and L respectively, are no longer good quantum numbers and must be combined to give a total angular momentum quantum number, J, according to the relationship $J = S + L$.

1.2.2. Magnetic susceptibility

When an applied magnetic field, B, interacts with the magnetic spins in a material, an induced internal field, M, can be observed. If the relationship between applied and measured field is linear (see 1.2.5), $M \propto B$, then we can define the materials magnetic susceptibility, χ, as

$$M = \chi B \tag{1.3}$$

measured per unit volume. The volume susceptibility can be freely converted to molar, χ_m, or mass, χ_g, susceptibilities whenever appropriate.

1.2.3. Diamagnetism

Diamagnetism, is concerned with the paired 'closed-shell' electrons and is a weak repulsive force produced by all materials that acts towards an applied magnetic field ($\chi < 0$). As each core electron orbits within a material, its orbit must cross the applied field. According to Lenz's law, any charge moving with respect to a magnetic field will experience an electromotive force. This force is minimised when the electronic moment aligns anti-parallel with that of the applied field, and as such a small opposing internal field is produced. The diamagnetic susceptibility of most materials is usually a weak effect, of the order of -1×10^{-6} emu mol^{-1}, and is often considered a minor adjustment when discussing materials with unpaired electrons.

1.2.4. Paramagnetism

Open-shell materials, *i.e.* those containing ions, atoms or molecules with unpaired electrons, interact more strongly with an applied magnetic field, and feature magnetic susceptibilities in the order of -1×10^{-4} emu mol^{-1}. They can be thought of as containing a permanent magnetic dipole moment that arises from the unpaired electrons. When no external field is applied, the paramagnetic state of these materials is analogous to the gaseous state of matter. Much like the motion of particles in a gas, the direction of the spin vector is only affected by random thermal fluctuations when there is no applied field, and interactions between spins are small enough on this energy scale to be ignored. In this respect, the spins can be thought of as uncorrelated, freely rotating vectors.

1.2.5. The Brillouin function and Curie-Weiss law

Upon application of a magnetic field, Zeeman-splitting breaks the degeneracy of the spin-states creating an energetic preference for states that are aligned with the direction of the field. Classically, the spins could take any orientation, a continuum of states, but due to the quantum mechanical nature of magnetism this is not the case. For a heavy metal ion where spin-orbit coupling is strong these states are quantised depending on the total angular momentum quantum number, J,(figure 1.1). For light ions and where L is quenched, such as the first row transition metals, spin-orbit coupling is weak and S rather than J is the good quantum-number.

There is a Boltzmann distribution over these energy levels leading to a temperature (T) and field (H) dependent population. The splitting between these energy levels,

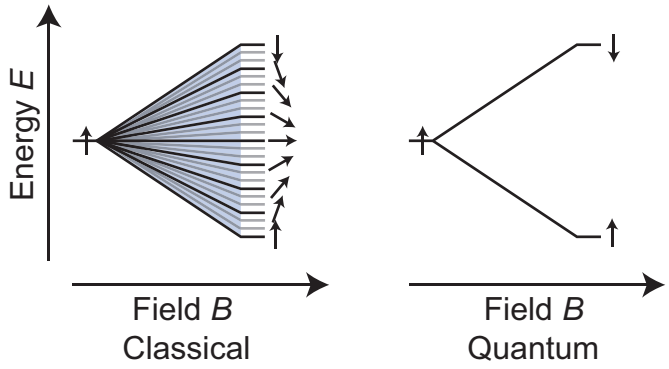

FIGURE 1.1. The Zeeman splitting of degenerate energy states upon application of a field. Left, illustrates the continuum of orientations and states possible in a classical system. Right, shows the Zeeman splitting for a quantised $J = \frac{1}{2}$ state.

E, upon application of a magnetic field, is found to be $E = \pm\mu_{\rm B}B$ for a single spin. This leads to populations of the lower, N_1, and upper, N_2, energy levels according to the Boltzmann distribution:

$$\begin{aligned}\frac{N_1}{N} &= \frac{e^{\mu_{\rm B}B/k_{\rm B}T}}{e^{\mu_{\rm B}B/k_{\rm B}T} + e^{-\mu_{\rm B}B/k_{\rm B}T}} \\ \frac{N_2}{N} &= \frac{e^{-\mu_{\rm B}B/k_{\rm B}T}}{e^{\mu_{\rm B}B/k_{\rm B}T} + e^{-\mu_{\rm B}B/k_{\rm B}T}}\end{aligned} \tag{1.4}$$

where N is the total number of spins ($N = N_1 + N_2$). In any finite field, there will therefore be a population difference between the energy levels, leading to a finite magnetisation. If we now consider N to be the number of spins per unit volume of a material, and $x = \mu_{\rm B}B/k_{\rm B}T$, we can see that the population asymmetry, and hence finite magnetisation, M, will have the form:

$$M = (N_1 - N_2)\mu_{\rm B} = N\mu_{\rm B}\frac{e^x - e^{-x}}{e^x + e^{-x}} = N\mu_{\rm B}\tanh(x) \tag{1.5}$$

.

This relationship is the special case of a $J = \frac{1}{2}$ system. The general form, for $J > \frac{1}{2}$, leading to $2J + 1$ equally spaced energy levels, is found to be

$$M = Ng_{\rm L}J\mu_{\rm B}B_{\rm J}(x), \qquad (x = \frac{g_{\rm L}J\mu_{\rm B}B}{k_{\rm B}T}) \tag{1.6}$$

where B_J is the Brillouin function, and takes the form

$$B_J(x) = \frac{2J+1}{2J}\coth(\frac{2J+1}{2J}x) - \frac{1}{2J}\coth(\frac{1}{2J}x) \tag{1.7}$$

and g_L is the Landé g-factor, defined as

$$g_L = \frac{3}{2} + \frac{S(S+1) - L(L+1)}{2J(J+1)} \tag{1.8}$$

For a free electron, $g_L \approx 2.0023$ (dimensionless). This g-factor can be considered an indicator of how strongly a moment couples to an applied field, or more specifically it is a proportionality constant that relates the spin, orbital and total angular momentum quantum numbers to the observed moment. The corresponding Brillouin functions for several values of J can be seen in figure 1.2.

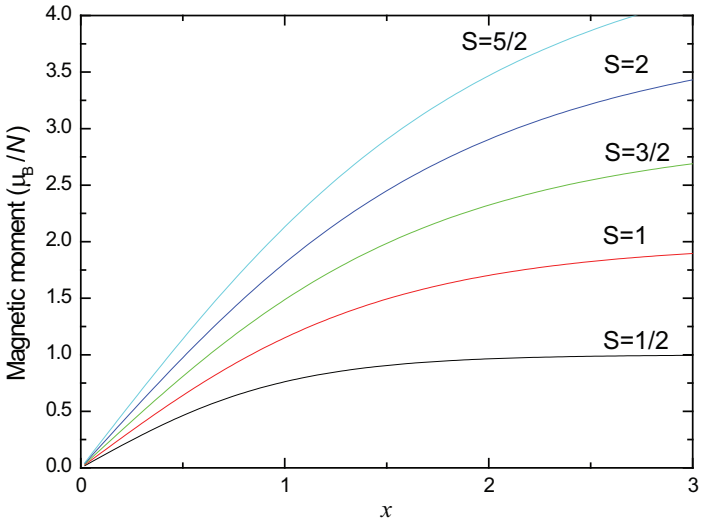

FIGURE 1.2. A plot of magnetic moment *vs.* x (where $x \propto \frac{B}{T}$) for several spin states, calculated using the Brillouin function. The graph shows that with increasing spin state, the saturation magnetisation at high field increases.

It is also worth noting that in the high-temperature, and low-field limit, where $x << 1$

$$\coth(x) = \frac{1}{x} + \frac{x}{3} - \frac{x^3}{45} + \ldots, \tag{1.9}$$

and so the field dependent magnetisation, the susceptibility, is found to be approximately linear with the form

$$\chi = \frac{M}{B} \approx \frac{NJ(J+1)g_{\mathrm{L}}^2\mu_{\mathrm{B}}^2}{3k_{\mathrm{B}}T} = \frac{C}{T} \tag{1.10}$$

Where C is the Curie constant for the material, defined as $C = \frac{N\mu_{\mathrm{eff}}^2}{3k_{\mathrm{B}}}$, with the *effective moment* of the material, $\mu_{eff} = g_{\mathrm{L}}\sqrt{J(J+1)}\mu_{\mathrm{B}}$. This leads to the common observation that, for a paramagnet, a plot of χ^{-1} *vs.* T is linear with a zero intercept, known as the Curie-law. In reality, this is often not the case and a correction term known as the Weiss constant, or Weiss temperature, θ_{W} must be used.

$$\chi^{-1} = \frac{T - \theta_{\mathrm{W}}}{C} \tag{1.11}$$

The correction term in this 'Curie-Weiss' law, accounts for the interactions between spins. The magnitude and sign of θ_{W}, in units of Kelvin, gives an indication of the mean exchange-field experienced by each ion. A positive intercept on the x-axis , from an extrapolation, of χ^{-1} *vs.* T indicates an average positive correlation between neighbouring spins, a ferromagnetic interaction. Conversely a negative intercept indicates a preference for anti-parallel alignment of the spins, antiferromagnetic coupling, resulting in lower net magnetisation (figure 1.3). An overview of the possible magnetic interactions, and the ordered-ground-state structures that these can lead to are discussed in sections 1.2.6 and 1.3.1 respectively.

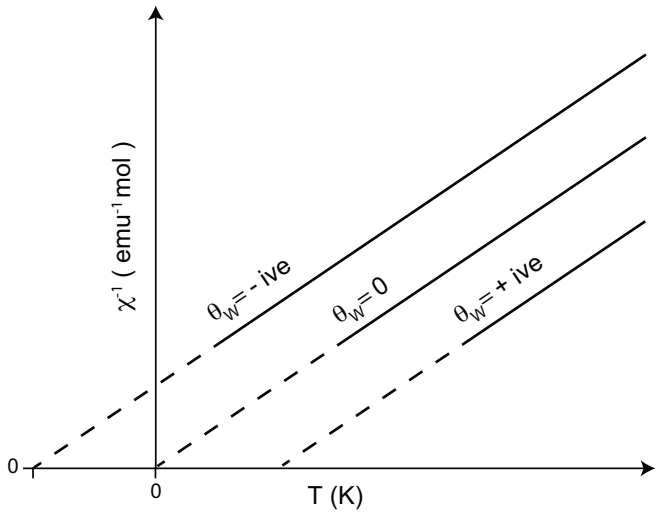

FIGURE 1.3. A plot of χ^{-1} *vs.* T showing the Curie-Weiss behaviour expected for positive, negative, and zero mean-exchange-field interactions, indicative of a ferromagnetic, antiferromagnetic, and zero coupling between ions.

1.2.6. Magnetic interactions

As a magnetic system is cooled from its paramagnetic state, the energy introduced by thermal fluctuations decreases and at some point the energy of one or more types of magnetic interaction can no longer be ignored. The strength and sign of the interaction between any two spins ($\vec{S_i}$ and $\vec{S_j}$) can be represented by a coupling term ($\vec{J_{ij}}$) in the simple Hamiltonian:

$$\mathcal{H} = -\sum_{i,j} J_{ij}(\hat{\vec{S}}_i \cdot \hat{\vec{S}}_j) \tag{1.12}$$

Discussed in the following sections are several ways in which a magnetic interaction, between spins, can be transmitted through a material.

1.2.6.1. *Dipolar interaction.* The simplest form of magnetic interaction is that of the dipolar interaction. All magnetic ions induce a magnetic field that falls in intensity as a function of $\frac{1}{r^2}$ distance from the spin. If two spins have large enough moments and are close enough in space, the interaction between the two induced fields will lead to a reorientation of the spins, and an ordered state (figure 1.4). Long range magnetic order as a result of the dipolar interaction is usually only observed at millikelvin temperatures due to the relatively weak strength of this interaction.

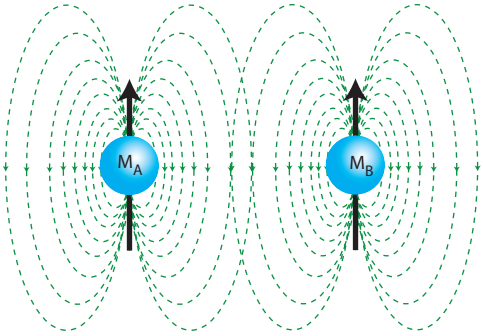

FIGURE 1.4. The interaction between magnetic dipoles, leading to spin polarisation.

1.2.6.2. *Direct exchange.* Direct exchange requires the overlap of electronic orbitals between neighbouring magnetic ions, and as such is most often seen in metals. The Pauli exclusion principle dictates that no two electrons can be in the same quantum mechanical state. Due to the overlap of electronic wave-functions between two neighbouring ions, the Pauli exclusion principle forces a correlation between the electronic spin states (figure 1.5).

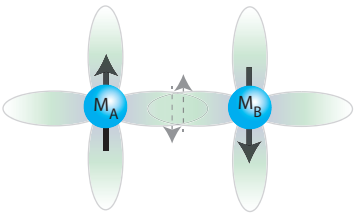

FIGURE 1.5. A representation of orbital overlap, leading to the direct exchange of spin polarisation.

1.2.6.3. *Super-exchange.* Much like direct exchange, super-exchange relies on the overlap of electronic wavefunctions to correlate the spin states of magnetic ions, but super-exchange differs in the degree of the exchange-pathway. Direct exchange is between directly neighbouring ions, super-exchange is mediated by a 3^{rd} (or sometimes more) ion, often oxygen or sulphur (figure 1.6). This is the most common exchange mechanism due to the abundant variety of ionic solids able to accommodate magnetic ions. Understanding the super-exchange pathway is not simple, as overlap of the electronic orbitals is extremely sensitive to distance, angle and hybridisation of the ions involved.[**4**] The simplest example of this effect is best described by the example of two magnetic ions ($M_{A,B}$) bonding through an oxygen, where the exchange pathway is either 90° or 180°. In this simplified picture the observed coupling, through M($3d$)-–O($2p$)–M($3d$) orbitals, will be either ferromagnetic ($J > 0$) or antiferromagnetic ($J < 0$), depending on the angle. Deviation from these extremes further complicates interpretation, and competition between these two mechanisms can reduce the net-exchange.

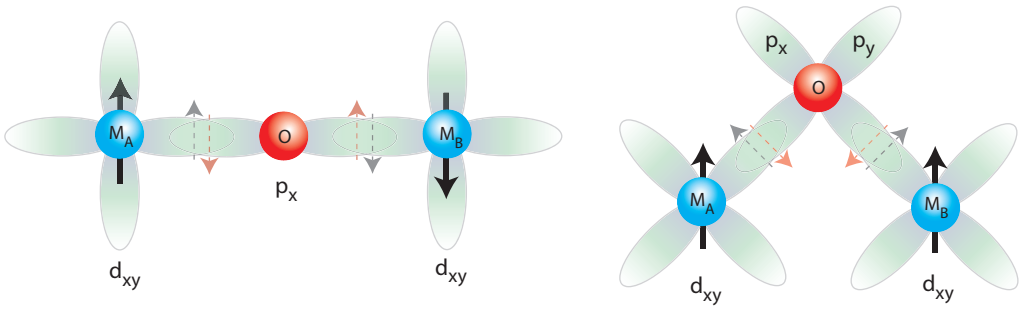

FIGURE 1.6. Anion mediated superexchange paths. Left, the antiferromagnetic exchange common in transition-metal oxides with an oxygen bridge $\sim$ 180°. Right, the ferromagnetic exchange expected for $\sim$ 90° bridged oxides.

1.2.6.4. *Anti-symmetric exchange: the Dzyaloshinskii-Moriya interaction.* Anti-symmetric exchange was first introduced by Dzyaloshinskii as a phenomenological

explanation for weak ferromagnetism noted in some largely-antiferromagnetic materials, and takes the form of an additional exchange term in the ordering Hamiltonian:

$$\mathcal{H} = \vec{D} \cdot [\vec{S_i} \times \vec{S_j}] \tag{1.13}$$

where $\vec{D}$ is a constant vector.[**5**] This phenomenological explanation was later built into a microscopic model by Moriya, showing that the consideration of a spin-orbit coupling mechanism to Anderson's superexchange formalism[**6**] naturally results in an additional exchange term with magnitude $D \sim (\Delta g/g)J$.[**7**] In contrast with the symmetric exchange of equation 1.12, the vector product term in equation 1.13 causes the Hamiltonian to be reversed by exchange of $\vec{S_i}$ and $\vec{S_j}$. For this reason it is often termed anti-symmetric exchange. In many systems, this additional term has been shown to induce a canting between neighbouring antiferromagnetic spins, subject to the symmetry constraints of the system.

1.2.6.5. *RKKY interaction.* The RKKY interaction is an exchange mechanism specific to materials containing conduction electrons. The magnetic field induced by localised electrons polarise the spin of the conducting electrons, and transmit this polarisation to neighbouring magnetic ions.

1.3. Magnetic Ground-states

In most magnets, below a given temperature, the energy of the magnetic interaction will overcome thermal fluctuations to create an ordered magnetic state. The structure of this ordered state is dependent on the different terms present in the magnetic Hamiltonian.

1.3.1. Conventionally ordered magnetic ground-states

When all of the dominant terms in the exchange Hamiltonian can be satisfied, a transition to an ordered ground-state is usually reached at a temperature in the same regime as the Weiss temperature. Over the next four sections several types of *simple* magnetic order are introduced.

1.3.1.1. *Ferromagnetism.* The ferromagnet is considered the simplest case of magnetic order, and involves all spins aligned parallel with their neighbours, $J_{ij} > 0$ (Figure 1.7.a.). In this case, the only symmetry of the parent ion structure that is broken is time-reversal symmetry. Due to the parallel alignment of all spins, a net magnetisation is induced.

1.3.1.2. *Antiferromagnetism.* Another conventional form of magnetic ground-state is that of an antiferromagnet. This structure relies on neighbouring ions to prefer the anti-parallel alignment, $J_{ij} < 0$ (figure 1.7.b.). Simple structures can be thought of as the combination of two ferromagnetically ordered sub-lattices that are aligned anti-parallel. The two sub-lattices produce equal moments in opposite directions, and so cancel to zero net-moment. The magnetic structures of antiferromagnets often have unit cell parameters larger than those of the nuclear crystal structure, although if there is more than 1 atom in the unit cell, the size of the parent cell can sometimes be kept, if the antiferromagnetically coupled moments are on different sites.

1.3.1.3. *Ferrimagnetism.* The ferrimagnet is a twist on the antiferromagnetic structure, and is commonly considered to be made up of two sub-lattices. The difference in this case is that one sub-lattice of ions has a different net moment to the other, seen in figure 1.7.c. This leads to an unequal cancellation between the two sub-lattices, and a finite magnetisation. This type of structure is most commonly seen in materials comprised of ions with two different spin states, such as the Fe^{2+} and Fe^{3+} in the ferrimagnet magnetite.

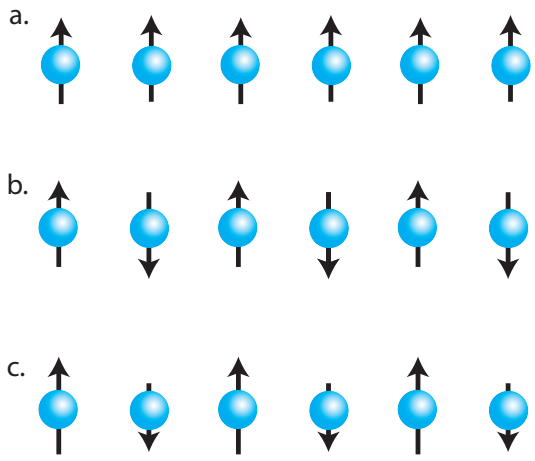

FIGURE 1.7. Conventionally ordered magnetic ground-states: a. The parallel alignment of a ferromagnet; b. The two sub-lattice antiparallel arrangement of an antiferromagnet; c. The two sub-lattice arrangement of unequal moments found in a ferrimagnet.

1.3.1.4. *Spin density waves and non-collinear stuctures.* Increasing in complexity, the next structure to consider is that of a spin-density-wave, illustrated in figure 1.8.a. In the simplest case, the spins are aligned collinear, but the magnitude and sign of the moment along x, of each ion, can be described by a sine-wave propagating through the structure along y. As the area under a sine wave always sums to zero, a spin-density-wave structure will also have zero net moment unless combined with a ferromagnetic moment.

This picture can be complicated further by considering structures that are described by two (or more) spin density waves. Figure 1.8.b. illustrates a cycloidal structure, where the magnitude of the moment in the x and y directions are described by two, out of phase (π-shifted), sine waves propagating along y. If the component of the moment in x and z is described by two π-shifted sine waves propagating along y then a helical spin structure, seen in figure 1.8.c., is produced.

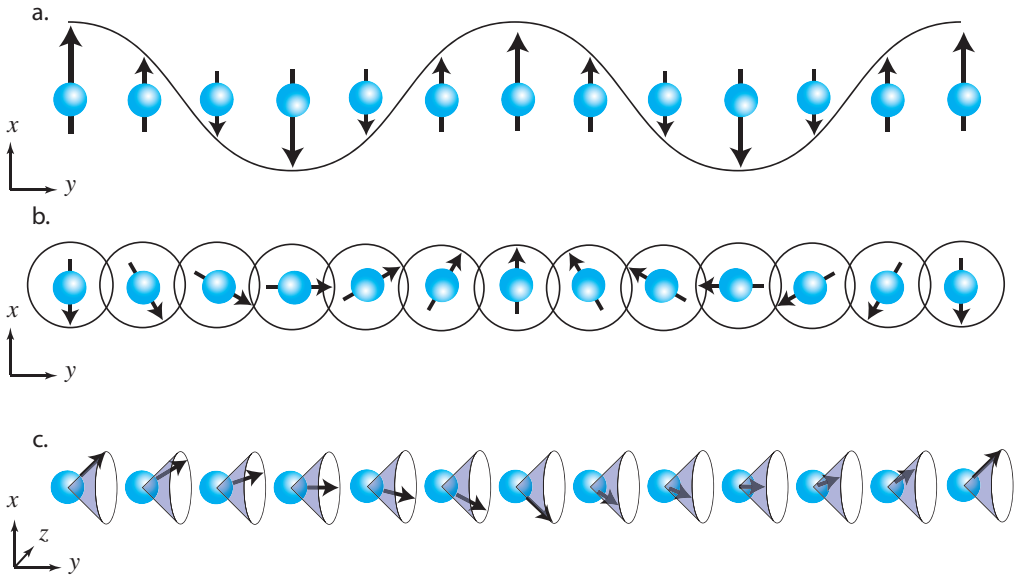

FIGURE 1.8. Illustrations of several magnetic structures built from spin-density waves: a. showing the simplest form of collinear arrangement – a transverse sine wave – where the magnitude of the spin along x is determined by a sine wave propagating along y. b. Shows a cycloidal structure as being the result of two π-shifted sine waves, propagating along y describing the magnitude of the moment along the x and y directions, a cycloidal structure. c. shows a helical structure where the magnitude of the moment along x and z is defined by two orthogonal π-shifted waves propagating along y. The spins in c. are also canted ferromagnetically along y for easier visualisation.

1.4. Highly frustrated magnetism

Simple ferromagnetic and antiferromagnetic configurations are ground-states of *un-frustrated* spin systems. This is the case where the interactions between neighbouring spins can be satisfied, *i.e.* there is no competition between the dominant interactions in the Hamiltonian. In many materials this is not the case and much theoretical and experimental effort has gone into understanding the physics of these frustrated systems. The properties displayed by frustrated spin systems are often poorly understood and provide a fertile playground for the study of new phenomena.

Magnetic frustration is commonly defined as the inability of *all* pair-wise 'magnetic' interactions to be satisfied simultaneously. This means that some terms in the exchange Hamiltonian of a frustrated system compete with each other. Some different types of competition will be introduced in the following sections.

1.4.1. Competing exchange interactions

Due to the numerous possible mechanisms of magnetic exchange in a crystalline material, the interactions that these exchanges give rise to are not always complimentary. This is most easily visualised by considering the interactions on a square lattice of ions, seen in figure 1.9, where the nearest neighbour interaction, J, is antiferromagnetic, and the next-nearest-neighbour interaction, J', is also antiferromagnetic. There is a competition between the configuration of the spins that the two interactions are trying to induce. With respect to the square lattice in particular, this competition has been shown to lead to a rich phase diagram involving ferromagnetic, antiferromagnetic and reentrant paramagnetic states, depending on the ratio of the energies of the two interactions J/J'.[**8**]

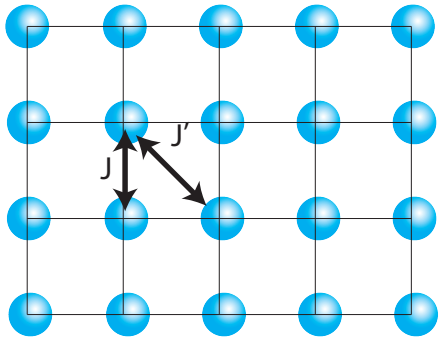

FIGURE 1.9. An illustration of the frustration caused by competing interactions on a single square plaquette. If both nearest-neighbour, J, and next-nearest-neighbour, J', are antiferromagnetic then both interactions cannot simultaneously be satisfied in the ground-state.

1.4.2. Geometric frustration

Geometric frustration is the term used when the symmetry of the underlying lattice, that the magnetic ions are situated on, inherently prevents the satisfaction of all pair-wise interactions. The canonical example of this is seen when the three vertices of a triangle are occupied by antiferromagnetically coupled Ising spins, *i.e.* those that are restricted to point along an axis. Each spin has two neighbours and the energy of

the interactions are minimised when the spin is aligned anti-parallel with both neighbours. It can be seen in figure 1.10.a–c. that if we attempt to minimise the energy of any single spin we are left in each case with two energetically favourable couplings (J_{AF}) and one unfavourable (J_F). Each of these ground-states therefore has the total energy of two favourable and one unfavourable coupling, and the ground-state is triply degenerate. If, for any reason, the symmetry of the lattice or Hamiltonian is lowered, this degeneracy will also be lowered, perhaps allowing the selection of a single ground-state. The simplest way of lowering the symmetry of an equilateral triangle is the compression of one vertex towards the centre, producing an isosceles triangle and selecting a single ground-state (figure 1.10.d.).

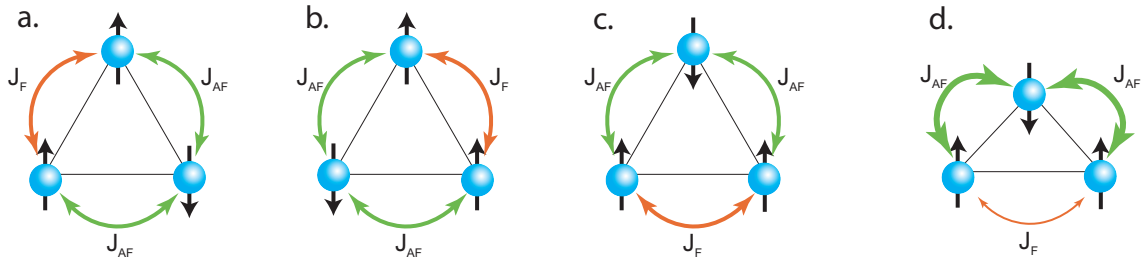

FIGURE 1.10. a–c. An illustration of the triple degeneracy of antiferromagnetically coupled ($E_{\mathrm{J}_{AF}} < E_{\mathrm{J}_F}$) Ising spins on the vertices of a triangle. Where J_{AF} and J_F represent antiferromagnetic and ferromagnetic coupling, respectively. d. The degeneracy breaking, and selection of a single ground-state could occur upon distortion of the triangle away from equilateral geometry.

1.4.3. Geometrically frustrated lattices

Whilst the magnetically frustrating properties of a single triangle are theoretically interesting, it is the emergent phenomena, seen when this frustration is extended across larger lattices that are of most interest. The frustration present in the extended lattices that can be built from triangular units often leads to highly degenerate ground-states. The following subsections give a *brief* overview of the exotic properties that can be found within materials brought about by this large ground-state degeneracy.

1.4.3.1. *The pyrochlore lattice.* The pyrochlore lattice is a 3-dimensional lattice built from triangular plaquettes. It consists of vertex-sharing tetrahedral units and can be seen in figure 1.11.a. The pyrochlore group of mineral structures have the general formula $A_2^{3+}B_2^{4+}\mathrm{O}_7$, where A is most commonly a rare-earth ion, and B a transition metal. The flexibility in the occupation of magnetic ions has allowed the observation of a large number of exotic phases in the pyrochlore materials. These exotic

phases range from unconventional spin-glasses seen in $Y_2Mo_2O_7$ and $Tb_2Mo_2O_7$,[**11, 12**] through classical spin-liquid phases in $Tb_2Ti_2O_7$ and $Yb_2Ti_2O_7$,[**13, 14**] and the spin-ice phases observed in $Ho_2Ti_2O_7$ and $Dy_2Ti_2O_7$.[**15, 16**] The spin-ice phase comes about because of the large single-ion anisotropy of Ho^{3+} and Dy^{3+}, along with a ferromagnetic exchange interaction. This leads to the well-known 2-in, 2-out, orientation of spins for each tetrahedral unit, mirroring the hydrogen orientations of water-ice.[**17**] The attention recently received by the spin-ices has increased due to the proposal and observation of defects in this 2-in, 2-out, state that act as magnetically charged quasi-particles known as magnetic monopoles.[**18**]

1.4.3.2. *The face-centred cubic lattice.* This 3-dimensional structure consists of magnetic ions present at the centre of the faces of a cube. This lattice is found in *B*-site ordered double perovskites, a class of materials with the general formula $A^{2+}B'^{(4+x)+}B''^{(4-x)+}O_6$, where *A* is most commonly an alkaline earth ion. The magnetic bonds between these sites can be viewed as an arrangement of edge-sharing tetrahedral sub-units seen in figure 1.11.b. The geometric frustration has been shown to suppress magnetic order well below the Weiss temperature in several of these double perovskites [**19**], as well as give rise to exotic ground-state properties such as the valence bond glass (VBG) state proposed in the double perovskite Ba_2YMoO_6.[**20**]

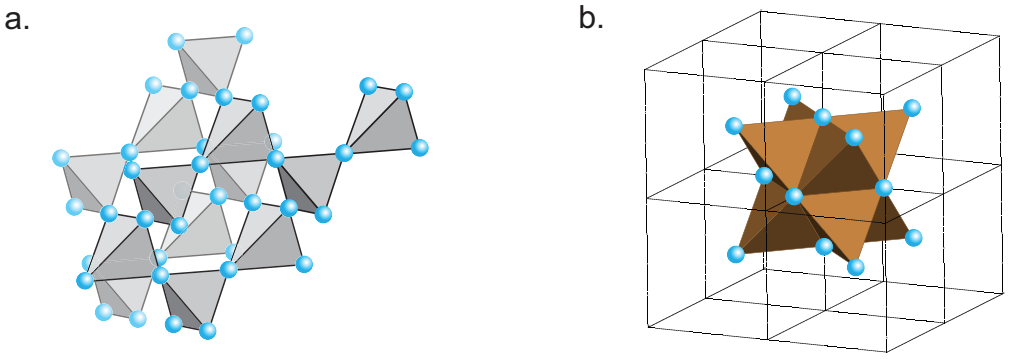

FIGURE 1.11. Examples of three dimensional lattices built from triangular (tetrahedral) building blocks: a. the corner sharing geometry of the pyrochlore lattice; b. the edge sharing of the face centred cubic lattice.

1.4.3.3. *The triangular lattice.* The triangular lattice, seen in figure 1.12.a., is the simplest 2-dimensional structure that can be built from triangular sub-units. The lattice consists of edge sharing triangles and as such each vertex is connected to 6 neighbouring vertices. The geometric frustration inherent in this lattice has been shown to suppress long-range order in high spin-state ions, such as $CsCoCl_3$,[**21**] as well as a number of exotic ground-states found in lower spin-state ions such as the

unconventional spin-freezing seen in $NiGa_2S_4$ [**22**] and the spin liquid ground states of κ-$(BEDT\text{-}TTF)_2Cu_2(CN)_3$ and $Ba_3CuSb_2O_9$.[**23, 24**]

1.4.3.4. *The kagome lattice.* Where the triangular lattice can be thought of as a lattice built from edge-sharing triangles, the kagome lattice is the corner-sharing analogue, seen in figure 1.12.b. The vertex-sharing low-connectivity of this lattice, compared to the edge-sharing of the triangular lattice, gives rise to a significantly more geometrically frustrated ground-states where a macroscopic degeneracy is predicted. Due to this large frustration, the kagome lattice has been extensively studied both theoretically and experimentally as a source of exotic physical properties. A more detailed description will be given in sections 1.5 and 1.6.

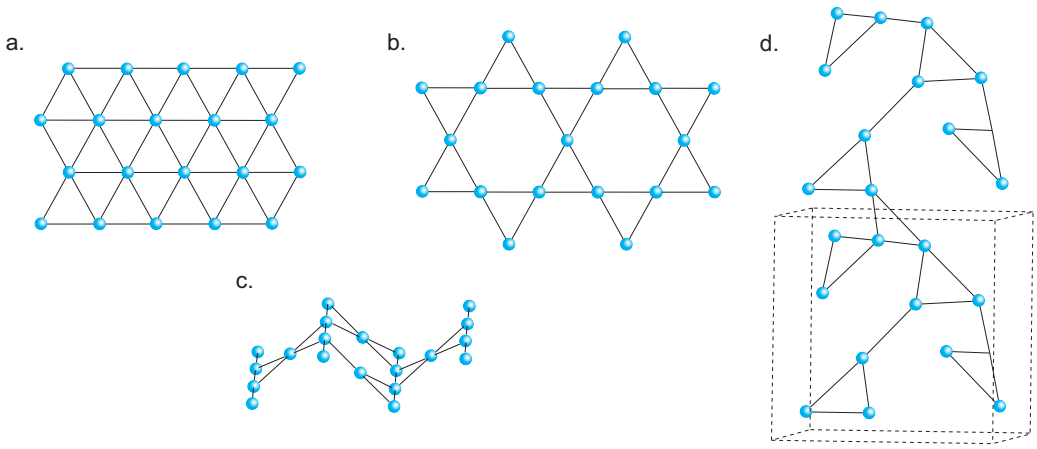

FIGURE 1.12. Two and three dimensional frustrated lattices built from the triangular plaquette: a. the triangular latttice, with edge sharing triangular subunits; b. kagome lattice, built from vertex sharing triangles; c. the kagome stair, consisted of puckered kagome planes; d. the hyper-kagome lattice.

In addition to the 2-dimensional kagome lattice, several analogues that extend into the third dimension are known. These include the *kagome staircase* structure of $Co_3V_2O_8$ and $Ni_3V_2O_8$ seen in figure 1.12.c.,[**25, 26, 28, 29**] as well as the *hyper-kagome* lattice of $Na_4Ir_3O_8$ seen in figure 1.12.d.[**30, 31**] Each of these 3-dimensional analogues display the corner-sharing triangular motif of the 2-dimensional kagome lattice and benefit from the same low connectivity that is expected to lead to the macroscopic degeneracies required for the existence of exotic ground-state behaviours.

1.5. Magnetic ground-state of a quantum kagome antiferromagnet

The search for spin-liquid ground-states was first brought into the limelight in the early 1980s when Anderson proposed that a specific type of quantum spin liquid, coined the resonating valence bond (RVB) state,[**10**] could provide insight into the transition to *unconventional* superconductivity seen in the high-T_c cuprates.[**9, 35**] Anderson's original work predicted that the geometric frustration of a *triangular* lattice of spins, coupled with the quantum fluctuations of an $S = \frac{1}{2}$ state could fully suppress conventional ordering and at some point the spins will form singlet dimers with their neighbours to lower their energy. Due to the large number of possible dimer configurations across the lattice, Anderson proposed that the ground-state of the lattice would be a quantum-mechanical superposition of all possible dimer configurations, a resonance structure.

It has since been found that the degeneracy of a dimer configuration on the kagome lattice is orders of magnitude larger than that on the triangular lattice, thanks to its corner sharing, low connective nature. Whilst it is agreed that conventional Néel order will be suppressed in the $S = \frac{1}{2}$ kagome lattice, the exact nature of the ground-state has been under considerable debate for over two decades.

The proposed ground-states fall roughly into two groups: valence bond crystals (VBC) and quantum spin liquids (QSL). In both of these cases, the spins are expected to dimerise into non-magnetic singlet pairs, with the VBC family of ground-states forming static dimer configurations, whilst the proposed QSL ground-states remain dynamic even at $T = 0$ K. Even within these groups there is conjecture over the exact properties, with several proposed lowest energy dimer configurations across the lattice.[**32**] These different configurations will each lead to loss of translational or lattice symmetries and so should give rise to specific and identifiable scattering properties.[**33, 34**]

Within the group of proposed QSL ground-states there are also a number of parameters possible that would lead to very different ground-state physics. An important question that is still to be addressed is whether or not the ground-state is gapped. Several theoretical works suggest a continuum of singlet excitations bridging the gap to the first triplet state,[**36, 37**] whilst others find a gapped ground-state.[**38**] Additionally, the nature of the dimer couplings is also under debate as it is not yet known whether dimer formation will be limited to nearest-neighbours or if further-neighbour pairings are possible and how this would effect the physics of the system.

There have also been calculations showing the possibility that entropy (fluctuations) will select an ordered state, crystallising it from the resonance state, known as *order by disorder.*[**39**]

In order to resolve these questions model materials must be studied, but of course nature is never that simple. Experimental models are never as pure as the theoretical constructs they are being used to test and the kagome lattice is no exception. A number of additional parameters can further complicate this picture in materials, such as: further neighbour exchange, important in the discussion of the magnetic properties of kapellasite and haydeeite (chapters 4 and 5 respectively); additional exchange terms in the Hamiltonian such as the antisymmetric Dzyaloshinsky-Moriya interaction, important for the discussion of spin-freezing in vesignieite (chapter 6); the possibility of 3-dimensional exchange pathways, key in a discussion of the properties of 'Mg-herbertsmithite' (chapter 3); incomplete occupation (dilution) of the kagome lattice; structural distortions away from the ideal lattice, present in vesignieite (chapter 6); crystal-electric field (CEF) effects and so on. Several attempts have been made to include these perturbations in theoretical calculations but without physical models to guide and refine these calculations; the results may be far from the truth.

1.6. Model kagome antiferromagnetic materials

In this section, a brief overview of some of the developments in model materials will be discussed. Initially the properties of some of the higher spin state jarosite structures will be considered, moving on to the properties of $SrCr_8Ga_4O_{19}$, the material that spurred much of the initial interest in frustrated systems. Following on from this the most recently studies examples of $S = \frac{1}{2}$ kagome antiferromagnets, volborthite, vesignieite and herbertsmithite, will be considered.

1.6.0.5. *Jarosites.* The jarosites are a group of minerals with the general formula $AM_3(OH)_6(SO_4)_2$, where $A = Na^+$, K^+, Rb^+, NH_4^+, H_3O^+, Ag^+, Tl^+ or $\frac{1}{2}Pb^{2+}$ and $M = Cr^{3+}$, Fe^{3+} or V^{3+}. The variety of magnetic and diamagnetic ions, or groups, available to occupy the structure gives rise to a rich family of model materials. In particular the flexibility of the M^{3+} site allows the study of several spin-states including $S = \frac{5}{2}$, $\frac{3}{2}$ and 1, showing a range of classical and semi-quantum ground-states. The structure of the jarosites can be seen in figure 1.13, showing the potassium-iron material.

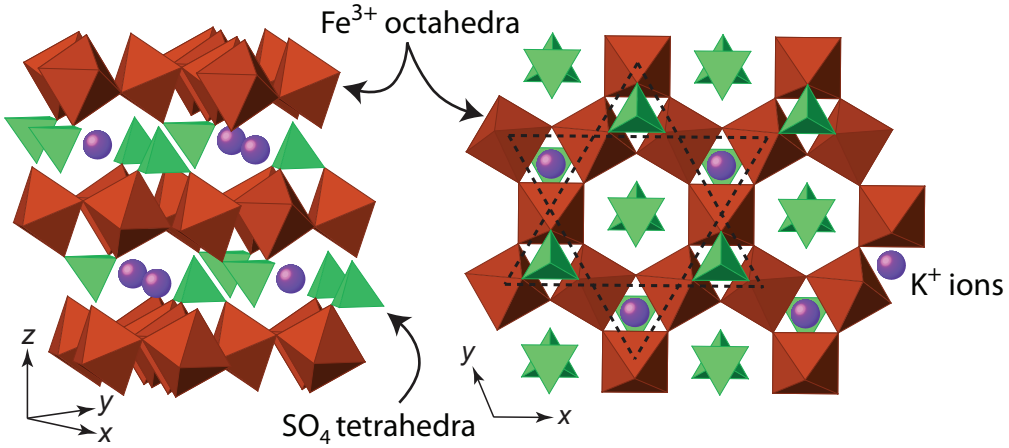

FIGURE 1.13. The crystal structure of potassium jarosite showing the kagome planes of $S = \frac{5}{2}$ Fe^{3+} ions, seperated by diamagnetic K^+ ions and SO_4 tetrahedra.

In the jarosite structure, the kagome planes of magnetically active ions are bound together by SO_4 tetrahedral units as well as interstitial A^+ ions (or groups). The wide variety of analogues available by substitution of both the A and B sites leads to a library of possible structures exhibiting a range of different magnetic responses and ground-states. In all cases the exchange is found to lead to a negative Weiss temperature, indicative of antiferromagnetic interactions. The high spin state $S = \frac{5}{2}$ Fe^{3+} analogues are the most intensely studied and in most cases a transition to a Néel ordered spin configuration is seen.[**40**] This ordered spin configuration is usually antiferromagnetic in nature, although weak ferromagnetism has been observed as a result of out-of-plane spin canting induced by antisymetric Dzyaloshinskii-Moriya exchange.[**42, 43**]

In contrast to the ordered ground-states of most of the iron jarosites, iron-hydronium jarosite, $(H_3O)Fe_3(SO_4)_2(OH)_6$, instead freezes into a topological spin glass state.[**44**] The nature of the retarding interaction that prevents conventional Néel order is still under debate, but recent results have shown that, unlike conventional spin glasses, structural disorder does not play a significant role and spin-anisotropy is the key feature.[**45, 41**]

In the lower spin state $S = \frac{3}{2}$ Cr^{3+} analogues, Néel order is still the dominant ground-state among the materials but reduced saturation magnetisations have been seen, indicating strong quantum fluctuations.[**46**] As with the Fe jarosites, it is the hydronium analogue, $(H_3O)Cr_3(SO_4)_2(OH)_6$, that gives rise to the most exotic physics. Quantum fluctuations are seen to suppress long range order down to 2.2 K, where only 5.4 % of the expected magnetic entropy is recovered.[**47**]

1.6.0.6. *SCGO.* $SrCr_8Ga_4O_{19}$, more commonly refered to as SCGO, was the first material to display anomalous low temperature behaviour that could be attributed to the frustrated geometry of a kagome lattice.[**48**] The magnetically active ions in the SCGO structure are $S = \frac{3}{2}$ Cr^{3+}, occupying three distinct crystallographic sites. Two of these sites make up pyrochlore-like slabs, with the third separating these slabs as dimerised Cr-pairs, seen in figure 1.14.

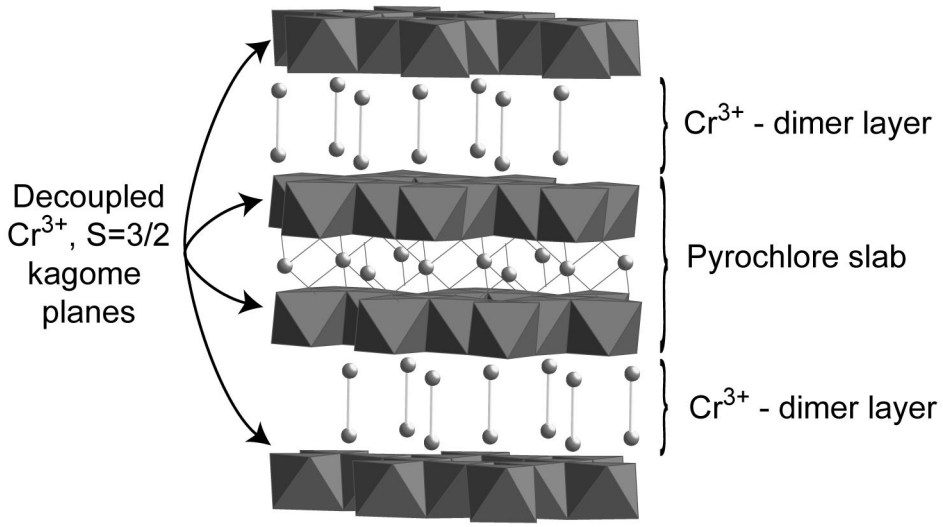

FIGURE 1.14. The crystal structure of SCGO showing the pyrochlore slabs of $S = \frac{3}{2}$ Cr^{3+} ions, seperated by Cr-Cr dimers. Due to predominantly 2-dimensional exchange within the pyrochlore slabs, the material can be considered a model kagome magnet. Only the Cr ions are shown for clarity.

The Cr-pairs are known to be well decoupled from the pyrochlore slabs, and have been shown to condense to singlets at relatively high temperatures.[**49**] The pyrochlore slabs are comprised of triangular-spacer layers, separating highly frustrated kagome planes of Cr^{3+}. Low temperature heat-capacity measurements have shown anomalous T^2 behaviour [**50**] and despite a glassy transition in susceptibility at $T_g = 3.3$ K,[**51**] muon spin rotation measurements have shown that after an initial slowing in spin dynamics, a plateaux is reached at $T \sim 1$ K with no spin freezing seen down to 50 mK.[**52**] The nature of the T^2 dependence is still not fully understood, but the glassy behaviour is attributed to disorder brought about by incomplete occupation of Cr^{3+} within the structure.[**48**] The observation of dynamical behaviour surviving down to the lowest temperatures spurred an increase of interest in frustrated systems, and paved the way for the study of new materials and exotic new properties.

1.6.0.7. *Volborthite.* The mineral volborthite, $Cu_3V_2O_7(OH)\cdot 2H_2O$, was for some time considered the closest approximation to a $S = \frac{1}{2}$ kagome antiferromagnet. First

synthesised in 1990 [**53**], it was not until 2001 that it was reported as a candidate spin liquid material. [**54**] No evidence of a magnetic ordering transition was seen in susceptibility, ^{51}V–NMR or specific heat measurements despite a Curie-Weiss temperature $\theta_W \sim -100$ K, indicating relatively strong antiferromagnetic exchange interactions. Initial synthetic samples, prepared by precipitation of the product from a solution of vanadium pentoxide and copper sulphate by addition of sodium hydroxide, showed relatively broad diffraction patterns indicative of poor crystallinity. This was greatly improved by hydrothermal annealing of the samples under elevated temperatures, and led to a distinct reduction of the Curie-tail and suppression of a weak spin-glass transition to lower temperatures, in the susceptibility data, assigned to crystal defects. [**55**]

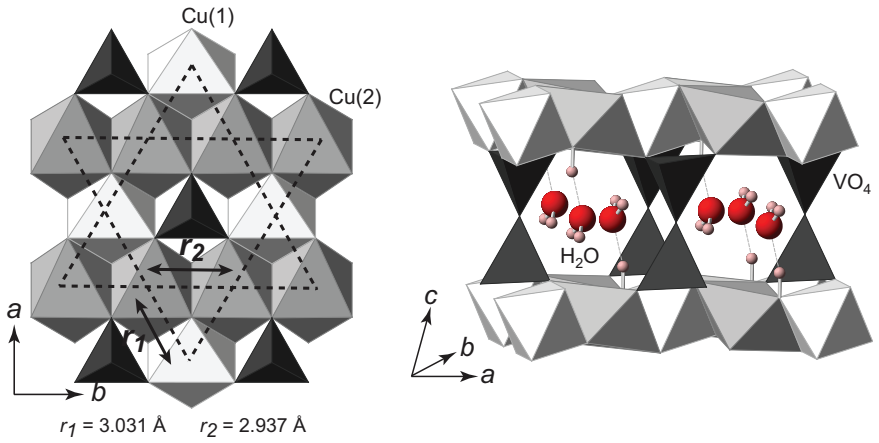

FIGURE 1.15. The crystal structure of volborthite showing well separated kagome planes of $S = \frac{1}{2}$ ions, with an isosceles distortion of the kagome triangles.

The crystal structure of volborthite has well separated kagome planes of CuO_6 octahedra, shown in figure 1.15. The hexagonal hole of the kagome plane is capped above and below by eclipsed pyrovanadate groups joining the planes. The remaining voids in the crystal structure are occupied by hydrogen bonded water molecules. Due to the preference for a Jahn-Teller distortion of the Cu^{2+} ions, the structure is monoclinically distorted, destroying the 3-fold symmetry axis of the kagome planes and resulting in two symmetrically distinct Cu^{2+} sites. This monoclinic distortion is not seen in the non-Jahn-Teller active Zn^{2+} analogue.[**56**] Each kagome-triangle is distorted away from equilateral to isosceles with a distortion of $(\frac{r_1-r_2}{r_1}) \times 100 = 3.01\%$. This symmetry breaking has the possibility of destroying the degeneracy of the magnetic ground-state and allowing the transition to a conventionally ordered state. Despite this perturbation no such ordering is observed, although below 2 K a slowing of the

spin dynamics is seen in muon spin relaxation measurements with a simultaneous freezing of $\sim 40\%$ of the Cu spins. Below this initial slowing, a plateau is seen that shows persistent dynamics down to the lowest temperatures measured, 50 mK.[**5**] Upon chemical dilution of the kagome lattice by diamagnetic Zn^{2+} ions persistent dynamics is seen in all samples up to a dilution of 40 %.[**58, 59**] It is still unknown as to whether both partial spin freezing and the plateau in spin dynamics is intrinsic to kagome physics, but its similarity to the response of the S=$\frac{3}{2}$ kagome magnet SCGO would suggest so.[**52**]

Further enriching the mystery of the ground-state of volborthite, high-field magnetisation measurements give evidence for a number of magnetisation plateaus at unexpected fractions of the saturation magnetisation. [**55**] Plateaus arise at $\sim \frac{1}{6}$ and $\frac{1}{3}$ of the total expected magnetisation of 1 μ_B Cu^{-1}. These fractional magnetisations are not explained by simple spin-configurations, and so it has been proposed that each step corresponds to a new type of spin-liquid phase.

1.6.0.8. *Vesignieite.* Vesignieite, $BaCu_3(VO_5H)_2$, has more recently been proposed as a model quantum-kagome magnet.[**60**] Much like volborthite, vesignieite contains a kagome lattice of $S = \frac{1}{2}$ Cu^{2+} ions that are monoclinically distorted as seen in figure 1.16.[**61**] Studies on minerals suggest that the distortion in vesignieite is notably less than that of volborthite at $\frac{r_1 - r_2}{r_1} = 0.07\%$ and so vesignieite can be considered a better model kagome magnet, this will be discussed in chapter 6. The kagome planes of vesignieite are separated by VO_4 octahedra and interstitial Ba^{2+} ions.

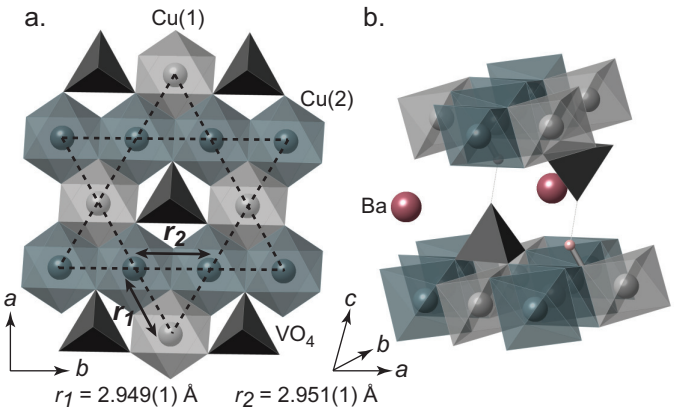

FIGURE 1.16. The crystal structure of vesignieite showing well separated kagome planes of $S = \frac{1}{2}$ ions, with an isosceles distortion of the kagome triangles.

The magnetic susceptibility of vesignieite shows no sign of a magnetic transition down to 2 K despite strong antiferromagnetic correlations evidenced by a Weiss temperatures of $\theta_W = -77$ K.[**60**] High field ESR measurements show evidence of the build up of short-range correlations below 20 K.[**62**] Laboratory X-ray diffraction of the vesigniete samples shows broad diffraction peaks, indicative of poor crystallinity. This poor sample quality is also evidenced in an enhanced Curie-tail in the susceptibility measurements. Attempts to subtract this Curie-tail by low temperature fits, gives rise to a broad hump centred at 20 K in agreement with the ESR results, and indicates an impurity contribution of $\sim 8\%$ free Cu spins.[**60**]

1.6.0.9. *Herbertsmithite.* Herbertsmithite, γ-$Cu_3Zn(OH)_6Cl_2$, is the $x = 1$ end-member of the atacamite family of minerals $Cu_{4-x}M_x(OH)_6Cl_2$ where M=Zn^{2+} or Mg^{2+}.[**63**] At $x = 1$, diamagnetic dilution of the pyrochlore-like lattice leads to well decoupled kagome planes of $S = \frac{1}{2}$ Cu^{2+} ions as seen in figure 3.1. The kagome planes are bound by the MO_6 octahedra as well as through O(H)–Cl bonding.

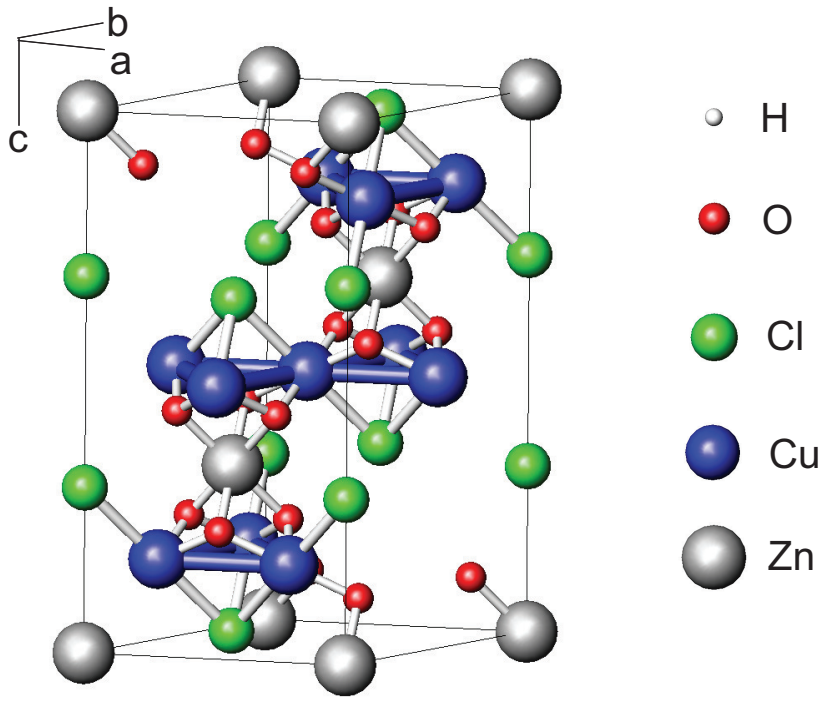

FIGURE 1.17. The crystal structure of herbertsmithite showing well separated kagome planes of $S = \frac{1}{2}$ Cu^{2+} ions, created by the controlled doping of Zn^{2+} onto a pyrochlore-like lattice.

Herbertsmithite was initially heralded as a 'perfect' model $S = \frac{1}{2}$ kagome magnet due to the 3-fold degeneracy of the Cu^{2+} lattice, not present in previous model

materials.[**64**] This 3-fold rotation symmetry means that herbertsmithite should retain the macroscopic ground-state degeneracy of the theoretical kagome lattice and lead to much purer kagome physics. Susceptibility measurements show no sign of a transition to an ordered ground-state down to 2 K, whilst μSR and specific heat measurements extend this to 50 mK.[**65, 66**] Despite these promising signs, several perturbations from ideality have been found in herbertsmithite samples. Neutron diffraction, ^{17}O-NMR and susceptibility measurements all indicate mixing between the Zn^{2+} and Cu^{2+} ions.[**67, 68, 69**] The consequences of this mixing are two-fold: diamagnetic dilution of the magnetic kagome lattice; and population of the interplanar sites by magnetically active ions that can then introduce a 3-dimensional exchange pathway. This mixing is minimised due to the preference of the Jahn-Teller active Cu^{2+} ion to reside in the tetragonally elongated coordination environment of the MO_4Cl_2 site, whilst the diamagnetic Zn^{2+} ion preferentially resides within the symmetric coordination of the MO_6 site.

In addition to the anti-site disorder, ESR measurements have shown a significant antisymmetric Dzyaloshinsky-Moriya component in the exchange Hamiltonian.[**70**] Whilst this has been shown by theoretical calculations to be able to induce conventional Néel order, the $D = 0.08J$ seen in herbertsmithite lies within the predicted spin-liquid regime of the D/J phase diagram.[**71**] Despite its deviations from an ideal model kagome magnet, herbertsmithite is considered a good realisation of the quantum kagome antiferromagnet.

1.7. Conclusion

Although several model $S = \frac{1}{2}$ kagome magnet materials are currently under study, none are without perturbations from ideality that complicate the analysis of their properties. Additionally, with a number of *subtly different* proposed ground-states to the $S = \frac{1}{2}$ kagome antiferromagnet, the problem is far from resolved. No material models have been found that fully encapsulate the simplicity of a theoretical system, and so the only way to differentiate the intrinsic kagome physics of these materials, from the extrinsic properties brought about by these deviations, is by comparing a number of near-ideal materials. Unfortunately with so few examples these comparisons are currently limited and so the search for new $S = \frac{1}{2}$ kagome materials has never been more important. The following chapters present our attempts to broaden this library of materials and further explore the physics of quantum kagome magnets.

References

[1] Kittel, C. *Introduction to solid state physics* John Wiley & Sons, Inc.: New York, Chichester, Brisbane, Toronto, Singapore. *Second Ed.*; **1996**.

[2] Blundell, S. *Magnetism in Condensed Matter*, Oxford University Press: Oxford. **2001**.

[3] Carlin, R. L. C. *Magnetochemistry*, Springer-Verlag. **1986**.

[4] Goodenough, J. B. *Magnetism and the chemical bond*, **1963**, *Wiley, New York*.

[5] Dzyaloshinsky, I. *J. Phys. Chem. Solids*, **1958**, *4*, 241.

[6] Anderson, P. W. *Phys. Rev.*, **1959**, *115*, 2.

[7] Moriya, T. *Phys. Rev.*, **1960**, *120*, 91.

[8] Vaks, V.; Larkin, A.; Ovchinnikov, Y. *Sov. Phys.*, **1966**, *22*, 820.

[9] Anderson, P. W.; Baskaran, G.; Zou, Z.; Hsu, T. *Phys. Rev. Lett.*, **1987**, *58*, 2790.

[10] Anderson, P. W. *Mat. Res. Bull.*, **1973**, *8*, 153.

[11] Greedan, J. E.; Sato, M.; Yan, X.; Razavi, E. S. *Solid State Commun.*, **1986**, *59*, 895.

[12] Greedan, J. D.; Reiners, J. N.; Penny, S. L.; Stager, C. V. *J. Appl. Phys.*, **1990**, *67*, 5967.

[13] Gingras, M. J. P.; den Hertog, B. C.; Faucher, M.; Gardner, J. S.; Dunsiger, S. R.; Chang, L. J.; Gaulin, B. D.; Raju, N. P.; Greedan, J. E. *Phys. Rev. B*, **2000**, *62*, 6496.

[14] Blöte, H. W. J.; Wielinga, R. F.; Huiskamp, W. J. *Physica (Amsterdam)*, **1969**, *43*, 549.

[15] Harris, M. J.; Bramwell, S. T.; McMorrow, D, F.; Zeiske, T.; Godfrey, K. W. *Phys. Rev. Lett.*, **1997**, *79*, 2554.

[16] Ramirez, A. P.; Hayashi, A.; Cava, R. J.; Siddharthan, R.; Shastry, S. *Nature (London)*, **1999**, *399*, 333.

[17] Bramwell, S. T.; Harris, M. J.; den Hertog, B. C.; Gingras, M. J. P.; Gardner, J. S.; McMorrow, D. F.; Wildes, A. R.; Cornelius, A. L.; Champion, J. D. M.; Melko, R. G.; Fennell, T. *Phys. Rev. Lett.*, **2001**, *87*, 047205.

[18] Bramwell, S. T.; Giblin, S. R.; Calder, S.; Aldus, R.; Prabhakaran, D.; Fennell, T. *Nature*, **2009**, *461*, 956.

[19] Martin, L, O-S.; Chapman, J. P.; Lezama, L.; Marcos, J. S.; Rodríguez-Fernández, J.; Arriortua, M. I.; Rojo, T. *Eur. J. Inorg. Chem.*, **2006**, *7*, 1362.

[20] de Vries, M. A.; McLaughlin, A. C.; Bos, J. W. G. *Phys. Rev. Lett.*, **2010**, *104*, 177202.

[21] Mekata, M.; Adachi, K. *J. Phys. Soc. Jpn.*, **1978**, *44*, 806.

[22] MacLaughlin, D. E.; Nambu, Y.; Nakatsuji, S.; Heffner, R. H.; Shu, L.; Bernal, O. O.; Ishida, K. *Phys. Rev. B*, **2008**, *78*, 220403.

[23] Pratt, F. L.; Baker, P. J.; Blundell, S. J.; Lancaster, T.; Ohira-Kawamura, S.; Baines, C.; Shimizu, Y.; Kanoda, K.; Watanabe, I.; Saito, G. *Nature*, **2011**, *471*, 612.

[24] Zhou, D. H.; Choi, E. S.; Li, G.; Balicas, L.; Weibe, C. R.; Qui, Y.; Copley, J. R. D.; Gardner, J. S. *Phys. Rev. Lett.*, **2011**, *106*, 147204.

[25] Wilson, N. R.; Petrenko, O. A.; Chapon, L. C. *Phys. Rev. B*, **2007**, *75*, 094432.

[26] Ramazanoglu, M.; Adams, C. P.; Clancy, J. P.; Berlinsky, A. J.; Yamani, Z.; Szymczak, R.; Szymczak, H.; Fink-Finowicki, J.; Gaulin, B. D. *Phys. Rev. B*, **2009**, *79*, 024417.

[27] Chen, Y.; Lynn, J. W.; Huang, Q.; Woodward, F. M.; Yildirim, T.; Lawes, G.; Ramirez, A. P.; Rogado, N.; Cava, R. J.; Aharony, A.; Entin-Wohlman, O.; Harris, A. B. *Phys. Rev. B*, **2006**, *74*, 014430.

[28] Kenzelmann, M.; Harris, A. B.; Aharony, A.; Entin-Wohlman, O.; Yildirim, T.; Huang, Q.; Park, S.; Lawes, G.; Broholm, C.; Rogado, N.; Cava, R. J.; Kim, K. H.; Jorge, G. A.; Ramirez, A. P. *Phys. Rev. B*, **2006**, *74*, 014429.

[29] Lawes, G.; Kenzelmann, M.; Rogado, N.; Kim, K. H.; Jorge, G. A.; Cava, R. J.; Aharony, A.; Entin-Wohlman, O.; Harris, A. B.; Yildirim, T.; Huang, Q. Z.; Park, S.; Broholm, C.; Ramirez, A. P. *Phys. Rev. Lett.*, **2004**, *93*, 247201.

[30] Okamoto, Y.; Nohara, M.; Aruga-Katori, H.; Takagi, H. *Phys. Rev. Lett.*, **2007**, *99*, 137207.

[31] Micklitz, T.; Norman, M.. R. *Phys. Rev. B*, **2010**, *81*, 174417.

[32] Ritchey, I.; Chandra, P.; Coleman, P. *Phys. Rev. B*, **1993**, *47*, 15342.

[33] Marston, J. B.; Zeng. C. *J. Appl. Phys.*, **1991**, *69*, 5962.

[34] Sing, R. R. P.; Huse, D. A. *Phys. Rev. B*, **2008**, *77*, 144415.

[35] Rokhsar, D. S.; Kivelson, S. A. *Phys. Rev. Lett.*, **1988**, *61*, 2376.

[36] Hastings, M. B.; *Phys. Rev. B*, **2000**, *63*, 014413.

[37] Mambrini, M.; Mila, F. *Eur. Phys. J. B*, **2000**, *17*, 651.

[38] Yan, S.; Huse, D. A.; White, S. R. *Science*, **2011**, *332*, 1201080.

[39] Reimers, J. N.; Berlinsky, A. J. *Phys. Rev. B*, **1993**, *48*, 9539.

[40] Wills. A. S. *Can. J. Phys.*, **2001**, *79*, 1501.

[41] Wills, A. S.; Bisson, W. G. *J. Phys.: Condens. Matter*, **2011**, *23*, 164206.

[42] Elhajal, M.; Canals, B.; Lacroix, C. *Phys. Rev. B*, **2002**, *66*, 014422.

[43] Ballou, R.; Canals, B.; Elhajal, M.; Lacroix, C.; Wills, A. S. *J. Magn. Magn. Mater.*, **2003**, *262*, 465.

[44] Wills, A. S.; Harrison, A.; Ritter, C.; Smith, R. I. *Phys. Rev. B*, **2000**, *61*, 6156.

[45] Bisson, W. G.; Wills, A. S. *J. Phys. Condens. Mat.*, **2008**, *20*, 452204.

[46] Lee, S.-H.; Broholm, C.; Collins. M. F.; Heller, L.; Ramirez, A. P.; Kloc, Ch.; Bucher, E.; Erwin, R. W.; Lacevic, N. *Phys. Rev. B*, **1997**, *56*, 8091.

[47] Wills, A. S. *Ph.D. thesis*, **1997**, *University of Edinburgh, Scotland.*

[48] Obradors, X.; Labarta, A.; Isalguè, A.; Tejada, J. *Solid State Commun.*, **1988**, *65*, 189.

[49] Lee, S.-H.; Broholm, C.; Aeppli, G.; Perring, T. G.; Hessen, B.; Taylor, A. *Phys. Rev. Lett.*, **1996**, *76*, 4424.

[50] Ramirez, A.P.; Espinosa, G. P.; Cooper, A. S. *Phys. Rev. B*, **1992**, *45*, 2505.

[51] Ramirez, A.P.; Espinosa, G. P.; Cooper, A. S. *Phys. Rev. Lett.*, **1990**, *64*, 2070.

[52] Bono, D.; Mendels, P.; Collin, G.; Blanchard, N.; Bert, F.; Amato, A.; Baines, C.; Hillier, A. D. *Phys. Rev. Lett.*, **2004**, *93*, 187201.

[53] Lafontaine, M. A.; LeBail, A.; Ferey, G. *J. Solid State Chem.*, **1990**, *85*, 220.

[54] Hiroi, H.; Hanawa, M.; Kobayashi, N.; Nohara, M.; Takagi, H.; Kato, Y.; and Takigawa, M. *J. Phys. Soc. Jpn.* **2001**, *70*, 3377.

[55] Yoshida, H.; Okamoto, Y.; Toyama, T.; Sakakibara, T.; Tokunaga, M.; Matsuo, A.; Narumi, Y.; Kido, K.; Yoshida, M.; Takigawa, M.; Hiroi, Z. *J. Phys. Soc. Jpn.*, **2009**, *78*, 043704.

[56] Kampf, A. R.; Steele, I. M. *Canadian Miner.*, **2008**, *46*, 687.

[57] Bert, F.; Bono, D.; Mendels, P.; Ladiue, F.; Duc, F.; Trombe, J. C.; Millet, P. *Phys. Rev. Lett.*, **2005**, *95*, 087203.

[58] Bert, F.; Mendels, P.; Bono, D.; Olariu, A.; Ladieu, F.; Trombe, J. C.; Duc, F.; Baines, C.; Amato, A.; Hillier, A. *Physica B*, **2006**, *374*, 134.

[59] Fukaya, A.; Fudamoto, Y.; Gat, I. M.; Ito, T.; Larkin, M. I.; Savici, A. T.; Uemura, Y. J.; Kyriakou, P. P.; Luke, G. M.; Rovers, M. T.; Kojima, K. M.; Keren, A.; Hanawa, M.; Hiroi, Z. *Phys. Rev. Lett.*, **2003**, *91*, 207603.

[60] Okamoto, Y.; Yoshida, H.; Hiroi, Z. *J. Phys. Soc. Jpn.*, **2009**, *78*, 033701.

[61] Ma, Z.; He, R.; Zhu, X. *Acta Crystallogr. Sinica*, **1990**, *64*, 302.

[62] Zhang, W.; Ohta, H.; Okubo, S.; Fujisawa, M.; Sakurai, T.; Okamoto, Y.; Yoshida, H.; Hiroi, Z. *J. Soc. Jpn.*, **2010**, *79*, 023708.

[63] Braithwaite, R. S.; Mereiter, K.; Parr, W. H.; Clark, A. M. *Mineral. Mag.*, **2004**, *68*, 527.

[64] Shores, M. P.; Nytko, E. A.; Bartlett, B. M.; Nocera, D. G. *J. Am. Chem. Soc.*, **2005**, *127*, 13462.

[65] Mendels, P.; Bert, F.; de Vries, M. A.; Olariu, A.; Harrison, A.; Duc, F.; Trombe, J. C.; Lord, J. S.; Amato, A.; Baines, C. *Phys. Rev. Lett.*, **2007**, *98*, 077204.

[66] de Vries, M. A.; Stewart, J. R.; Deen, P. P.; Piatek, J. O.; Nilsen, G. J.; Ronnow, H. M.; Harrison, A. *Phys. Rev. Lett.*, **2009**, *103*, 237201.

[67] Lee, S. H.; Kikuchi, H.; Qui, Y.; Lake, B.; Huang, Q.; Habicht, K.; Kiefer, K. *Nat. Mater.*, **2007**, *6*, 853.

[68] Olariu, A.; Mendels, P.; Bert, F.; Duc, F.; Trombe, J.; de Vries, M. A.; Harrison, A. *Phys. Rev. Lett.*, **2008**, *100*, 087202.

[69] Helton, J. S.; Maton, K.; Shores, M. P.; Nytko, E. A.; Bartlett, B. M.; Yoshida, Y.; Takano, Y.; Suslov, A.; Qui, Y.; Chung, J. H.; Nocera, D. A.; Less, Y. S. *Phys. Rev. Lett.*, **2007**, *98*, 107204.

[70] Zorko, A.; Nelluta, S.; van Toll, J.; Brunel, L. C.; Bert, F.; Duc, F.; Trombe, J. C.; de Vries, M. A.; Harrison, A.; Mendels, P. *Phys. Rev. Lett.*, **2008**, *101*, 026405.

[71] Cepas, O.; Fong, C. M.; Leung, P. W.; Lhuillier, C. *Phys. Rev. B*, **2008**, *78*, 140405.

CHAPTER 2

Experimental techniques

The search for exotic magnetic phenomena takes two branches: theorists that make predictions based on simplified models and theoretical constructs; and the experimentalists that search for, synthesise, and experiment on real materials, looking for these predicted novel phenomena. The work discussed in this thesis is that of an experimentalist, and as such a wide range of experimental tools have been used. In the following section, a brief overview of the different experimental techniques used during this research will be given.

2.1. Scattering techniques

Scattering is the broad term used for the study of the interaction between an incident wave (or particle, using wave-particle duality and de Broglie's formula $\lambda = \frac{h}{mv}$, where λ is the wavelength, h is the Planck constant, m is the particle mass and v is the velocity) and a material of interest. This interaction is termed either elastic or inelastic depending on whether the energy of the incident radiation is equal or unequal, respectively, to that of the scattered beam. The interaction can also be either coherent, or incoherent depending on whether or not there is a well defined phase relation between the scattered and incident beams.

Several types of coherent elastic and inelastic scattering techniques were used to probe the structure and properties of the materials discussed during this thesis. The following texts were used in the preparation of this section and should be referred to for a more complete discussion of the techniques presented here.[**1, 2**]

2.1.1. Elastic scattering: Diffraction

Bragg diffraction refers to the coherent-elastic scattering of an incident wave from a regularly repeating lattice, and is a result of interference between the scattered waves. For crystalline solids, where the unit cell periodicity is usually in the 1–100 Å range,

the wavelength must also be in the order of angstroms (0.1 nm), corresponding to X-rays when using electromagnetic radiation as the probe.

Constructive interference of the diffracted waves leads to the observation of strongly enhanced scattering in specific directions, dependent on the repeating planes of the crystal being probed. These repeating planes within a 3-dimensional lattice, are indexed according to the way in which the plane cuts the three unit cell axes. The index for each reflection is known as its Miller index and given the notation (hkl), where h, k and l are the inverse of the fraction that the plane cuts each of the unit cell axes a, b and c. For each (hkl)-reflection, a d-spacing, the distance between consecutive planes, can be calculated using the unit cell lattice geometry (figure 2.1). From considering the trigonometry of this simplified model it can be shown that in order for constructive interference to occur the following rule known as Braggs law must be fulfilled

$$n\lambda = 2d\sin\theta \tag{2.1}$$

where n is a positive integer, λ is the wavelength of the incoming radiation, d is the d-spacing of a specific reflection and θ is the scattering angle normal to the reflection plane.

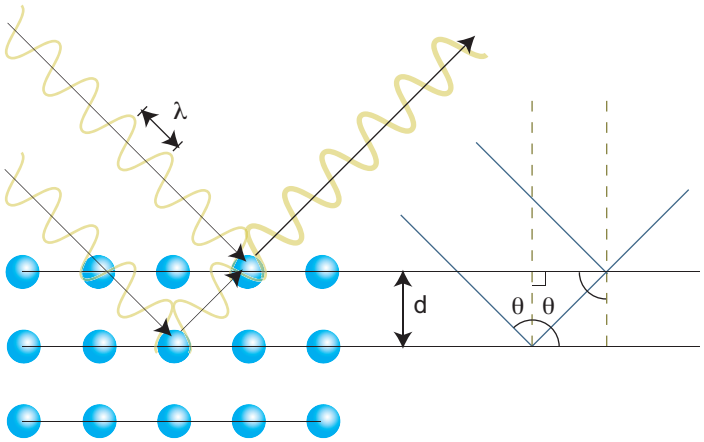

FIGURE 2.1. An illustration of the constructive scattering of incoming radiation from separated planes of atoms within a crystalline solid. The waves interfere constructively when the difference in path length travelled by the waves is a multiple of the wavelength.

When a monochromatic beam of X-rays, neutrons or electrons are scattered, peaks of intensity at positions in 2θ will be observed corresponding to each (hkl) reflection. If the probing particles have mass, such as neutrons or electrons, their wavelength

is dependent on their momentum and hence speed, v. Using massive particles as radiation an entire pattern can be obtained by probing the sample with a short pulse of a polychromatic beam and collecting a time-dependent pattern at a single point of known distance from the sample. As the *time-of-flight* from source to sample and from the sample to detector is particle-speed (wavelength) dependent the d-spacing for any Bragg peaks can be written with respect to particle travel time (*time-of-flight*).

2.1.2. Inelastic scattering

This broad definition covers all forms of spectroscopy where the energy difference between incident and scattered beams corresponds to the excitation or de-excitation of a molecule, crystal or electron between different-energy states. Each spectroscopic technique probes specific classes of transitions such as the bond stretching and bending excited by infra-red spectroscopy, or the electronic transitions probed in UV-vis spectroscopy.

In order to probe magnetic excitations, inelastic neutron scattering is the technique of choice. When interacting with the sample, a neutron can gain or lose energy, changing its momentum. In order to measure this the energy of the neutron must be known before and after the scattering process. This measurement can be done in two ways: *triple-axis* measurements use a *constant beam* of monochromatic neutrons, where after scattering a second monochromator is used to sweep specific energy ranges of interest for detection; alternatively if a *single pulse* of monochromatic neutrons are scattered by a sample, the neutrons will spontaneously separate according to their scattered momentum (speed), allowing time-dependent detection. This method is known as *time-of-flight*, *tof*, neutron spectroscopy.

Due to the extremely low weighting of inelastically scattered neutrons relative to elastic scattering, care must be taken to minimise background and noise that could obscure the spectrum. In order to do this, modern *tof* spectrometers, such as IN5 at the ILL, are built within vacuum chambers to reduce air scattering, and internal surfaces are coated with strongly neutron absorbing material to prevent contamination by reflected neutrons and secondary scatterers.

The magnetic moment of the neutron enables them to interact with and probe the magnetic excitations of a material. These excitations are directly dependent on both the type and strength of magnetic interactions present in the material. In addition to magnetic excitations, the neutrons are also capable of exciting cooperative structural

vibrations, phonons, although a characteristic phonon Q-dependence can often allow for satisfactory subtraction.

2.2. Diffraction instrumentation

A number of diffractometers, optimised for different uses, were used during the research presented in this thesis. Each class of diffractometer is discussed in the following section.

2.2.1. Laboratory powder X-ray diffraction

For routine characterisation of polycrystalline samples laboratory X-ray diffractometers are commonly used. The X-rays are generated by acceleration of electrons towards a metal target. Upon impact with the target, core electrons are excited to high energies that decay and produce a spectrum of X-rays, specific to the choice of target metal. For all laboratory X-ray diffraction patterns discussed in this thesis a Cu source was used, giving a characteristic spectrum of $K_{\alpha 1} = 1.5406$ Å, $K_{\alpha 2} = 1.5444$ Å and $K_{\beta} = 1.3923$ Å radiation. The K_{β} is then removed using a thin foil of Ni, and the $K_{\alpha 2}$ is often (but not in all cases) removed by aligned monochromating mirrors.

A number of different optic configurations, can be used to optimise the instrument for specific characteristics and functionality. The most common orientations used are the transmission-capillary, and flat-plate reflection geometries. Transmission-capillary geometry is often used with small sample mass, and so is less prone to texture issues. It is also easier for use with air sensitive samples. Flat-plate reflection geometry is more common and allows easier loading and the use of larger samples.

Additional optic components can also be used to eliminate unwanted characteristics of the pattern but usually at the cost of flux leading to increasing collection times. Common components include: primary monochromator, eliminating $K_{\alpha 2}$ from the X-ray spectrum; secondary monochromator, eliminating $K_{\alpha 2}$ and fluorescence effects; primary and secondary soller-slits, reducing background from air scattering as well as reducing low angle axial divergence broadening; primary and secondary slits to reduce background scattering. All laboratory diffraction patterns shown within this thesis were collected on either a Bruker D8 Advance or a Bruker D4 Discover diffractometer. The optic configurations of these two diffractometers are shown in figure 2.2.

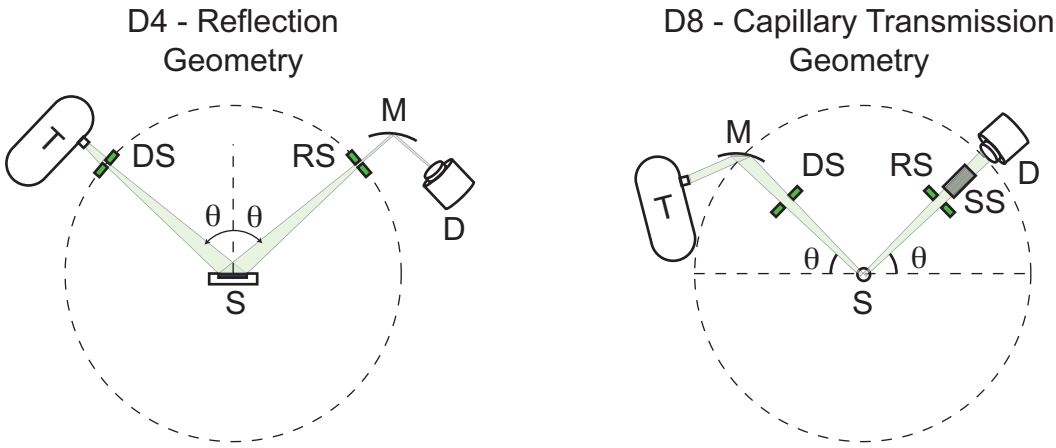

FIGURE 2.2. An illustration of the of the instrumental geometries of UCLs D4 and D8 X-ray diffractometers. T, S and D labels represent the X-ray tube, sample and detector respectively. M represents a focusing/monochromating mirror. DS, RS and SS are the divergence, receiving and soller slits respectively.

2.2.2. Synchrotron powder X-ray diffraction

Whilst laboratory X-ray diffractometers can provide diffraction patterns suitable for Rietveld refinement, laboratory instruments often lack the resolution and signal-to-noise ratio for resolving many more specific structural problems. This is where synchrotron X-ray diffraction is the structure characterisation method of choice.

Magnets can be used to alter the path of electrons travelling at *ultra-relativistic* speeds (close to the speed of light). As electrons are charged particles any change in their momentum will cause them to emit electromagnetic radiation and in a synchrotron this effect is exploited to produce a high intensity beam of X-rays. Beam-line 11-BM at the Advanced Photon Source (APS) was used for the collection of several diffraction patterns presented in this thesis. The beam-line schematic is shown in figure 2.3a, reproduced from Wang *et al.*[**9**] The multiple focusing and monochromating optics gives rise to minimal instrumental broadening of the diffraction patterns, as well as extremely low background. Coupled with the high resolution, energy resolved detector used on 11-BM, these properties lead to extremely sharp diffraction patterns with minimal peak overlap even in high-Q regions that are not accessible using any other technique (figure 2.3b.). The high flux of the synchrotron allows a good signal to noise ratio in this region increasing dramatically the information content with respect to laboratory X-ray sources.

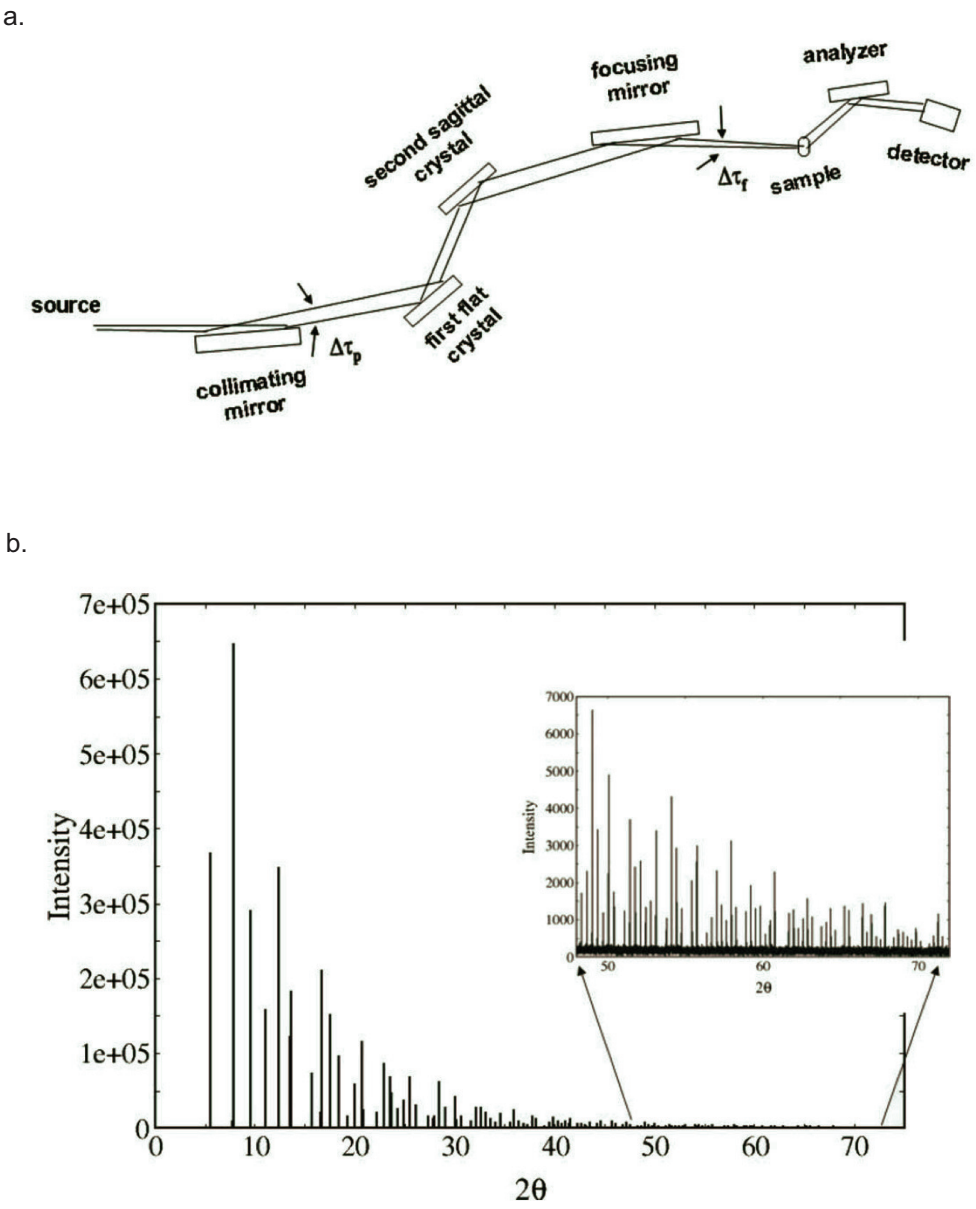

FIGURE 2.3. a. The optics configuration of the 11BM beam-line of the APS. b. An example diffraction pattern from NIST standard LaB_6 (SRM660a) using $\lambda = 0.4012435$ Å, showing the high instrument resolution, leading to clearly resolved peaks with good signal to noise even at high angle.[**9**]

2.2.3. Constant wavelength powder neutron diffraction

Complimentary to the use of X-ray radiation as a diffraction probe, neutrons of suitable wavelength are also diffracted by a crystalline solid. In contrast to the interactions of electromagnetic radiation with the electron density of a crystalline solid, neutrons are scattered by the nuclei of atoms. Scattering properties vary for each isotope and are not dependent on mass or charge so can be used for confident

refinement of light atoms such as lithium when an X-ray diffraction pattern would be dominated by heavier atoms, with greater core electron-density.

As well as probing the nuclear structure of a solid, the intrinsic magnetic moment a neutron makes it sensitive to the magnetic fields present within a material. If the material is in a magnetically ordered state the magnetic structure will give rise to Bragg scattering in an identical manner to that of the nuclear structure, and so can be refined using similar methods.

Diffraction patterns collected on the high resolution powder neutron diffractometer D2b, at the *Institute Laue Langevin* (ILL) will be be presented within this thesis. The ILL uses a nuclear-fusion reactor as a high-flux source of neutrons and as such the majority of instruments operate in *constant wavelength* collection modes. For D2b, the polychromatic thermal neutrons produced in the reactor are monochromated using the [111] reflection from a graphite single crystal. The beam is then diffracted from the sample and collected using a wide 2-dimensional detector. To obtain a 1-dimensional powder diffraction pattern for refinement, the 2-dimensional Debey-Scherrer cones are summed over in either high-intensity (full detector) or high-resolution (central 3^{rd} of detector) modes. An illustration of the instrument setup can be seen in figure 2.4, reproduced from the ILL *Yellow Book*.[**10**]

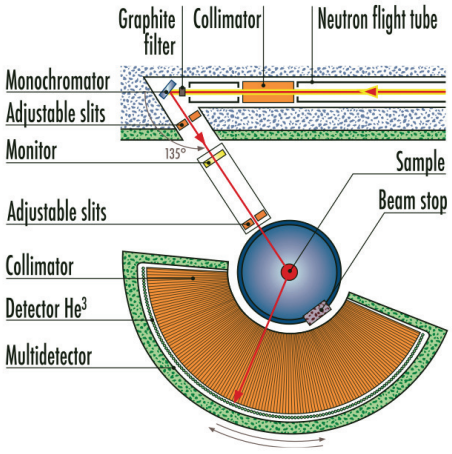

FIGURE 2.4. The instrument layout of powder neutron diffractometer D2b, ILL. Showing the incoming polychromatic beam of neutrons from the reactor, followed by monochromator, sample, collimator and detector array, reproduced from the ILL *Yellow Book*.[**10**]

2.2.4. Time-of-flight powder neutron diffraction

As previously mentioned in section 2.1.1, the intrinsic mass of the neutron allows a diffraction pattern to be collected as a function of time if a single pulse of polychromatic neutrons are used. This is the case when the neutrons are produced by a spallation-source due to the pulsed nature of the neutron generation. This method of collection maximises the count-per-pulse of neutrons, as losses due to monochromation are avoided, but flux at sample is still lower than that of an average reactor-source beam-line. As such all neutrons are precious and collection is maximised by using large detector banks. The neutron momentum-distribution at each beam-line is regulated by a moderator that thermalises the neutron pulse. Common moderator materials are deuterium oxide or deuterated methane, and create a pulse with a well defined distribution of neutron wavelengths. This distribution must then be incorporated into the Rietveld refinement process to correct for systematic intensity changes across the pattern.

2.2.5. Rietveld refinement

The diffraction pattern from a crystalline sample contains a vast amount of information about the structure of that sample. Unfortunately, when diffracting from a polycrystalline (powder) sample the averaging that takes place due to the random orientations of the crystallites destroys much of this information. In most cases there is no longer a single, unique, structural solution to a fit of the diffraction data and so chemical knowledge must be used when attempting a refinement. Typical analysis proceeds from a starting structural model, close to the expected crystal structure. This starting model can then be refined using the fit to the diffraction data as a guide. The progression of the fit must be coupled with a knowledge of chemistry and bonding as refinements can commonly fall into minima with unphysical structural parameters. For a more complete discussion of the topic, please refer to the following texts.[**3, 2**]

The most common method of refining a crystallographic model from powder diffraction data relies on the minimisation of a least squares matrix of all the free parameters to improve the fit to the experimental data, a technique first developed by H. Rietveld.[**4**] When performing this type of structural refinement there are a number of different classes of parameters that can be refined, including: peak shape, the theoretical delta-functions of reflections from a perfect crystal are broadened by both sample and instrument effects and as such must be modelled using mathematical

functions; background, incoherent sample scattering, air scattering and stray particles can all add to the background of the pattern and therefore must be modelled independently from any structural parameters; lattice parameters, that give rise to the reflection positions; atomic structural parameters such as atomic positions and thermal displacement parameters for each atom. Each of these parameters will have a different, often very subtle, effect on the model diffraction pattern and can sometimes be correlated with one another. As such, a careful considered approach must be taken to the order in which these parameters are *switched on* to refine, constantly reviewing the fit to the model and checking that the refinement variables remain physically meaningful and reasonable.

Several Rietveld refinement software packages are currently available, including the freeware programs GSAS[**5**] and FullProf[**6**], as well as the commercially available Topas.[**7**] Each of these programs have their strengths and weaknesses and as such throughout this thesis each have been used when appropriate. A less common technique for refinement uses the *derivative difference* method.[**8**] Programs utilising this type of refinement algorithm were not used in the preparation of this thesis and will not be discussed here.

2.3. Physical property measurements

Once the atomic structure of a material has been determined and refined we can move on to determining the magnetic properties of a material. This section discusses the techniques used during this thesis for the measurement of the physical properties of the studied samples.

2.3.1. DC SQUID magnetometry

When probing the magnetic properties of a material, a measure of its bulk magnetisation in response to an applied magnetic field provides information about the state of its unpaired electrons. A DC-SQUID magnetometer is an ideal instrument for this form of measurement. The magnetometer is comprised essentially of three components: a superconducting magnet for applied field (H) generation; a sample transport for generating a response; and a pick-up coil for measurement of this response seen in figure 2.5a. Additionally, the sample space is usually coupled with some form of temperature control system such as cryogenic cooling, or sample heating. The superconducting magnet can be charged with a current that gives rise to a static, homogeneous, (DC) field. The sample is moved through the pick-up coils

using the sample transport and Lenz's law dictates that any charge being subjected to a field gradient will feel a force. This force generates a measurable potential in the pick-up coil that is dependent on the size of the moment in the sample.

In order to minimise detection error, the pick-up coil is wound in a '–++–' loop configuration that gives rise to a characteristic current profile as the sample is moved through the coils, that can then be fitted and integrated to give the bulk sample moment (figure 2.5b.).[**11**]

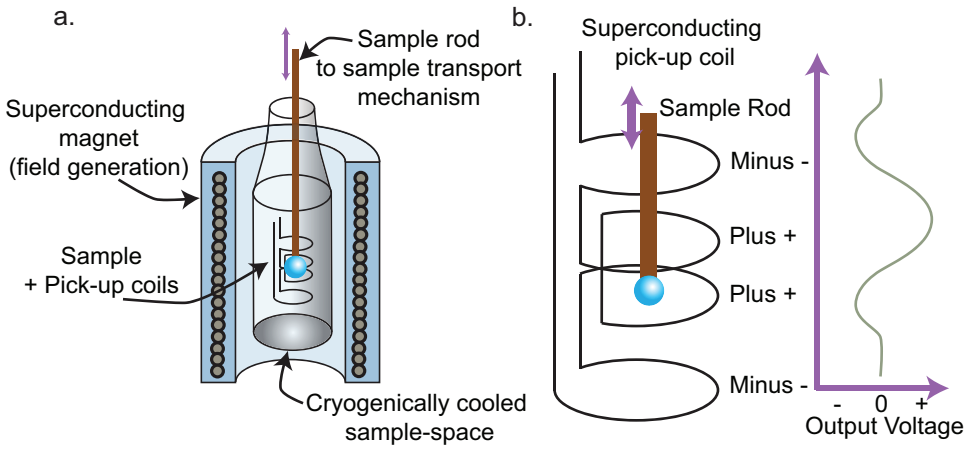

FIGURE 2.5. a. A schematic representation of the internal components of a DC-SQUID magnetometer, showing the cryogenically cooled sample space, superconducting magnet, pick-up coils and sample rod. b. The loop configuration of the pick-up coil gives rise to a characteristic voltage output as the sample travels through it.

For insertion into the magnetometer, a sample of known mass is loaded into a gelatin capsule, inserted into a clear plastic straw then mounted onto the brass sample rod. This configuration gives rise to minimal background and sample holder diamagnetism, whilst remaining cheap and easily repeatable.

The sample space is housed within a liquid helium cryostat that is capable of stable temperature variation across a wide range (2–400 K). Using a DC-SQUID there are two common experiment modes: measurements of magnetisation *vs.* temperature (M *vs.* T), where the magnetic susceptibility of a sample, in a single field, can be followed as a function of temperature; and measurements of magnetisation *vs.* applied field (M *vs.* H).

These measurements can be used to determine a number of properties related to magnetic materials such as magnetic transition temperatures, saturation magnetisation, Weiss temperature and a number of other parameters discussed in chapter 1.1.

Alternative to DC-SQUID measurements, further information can be gained from the use of an AC-SQUID. This method employs a dynamically-modulated applied field that gives additional information about the in phase (χ') and out-of-phase dynamic susceptibility (χ") that can help differentiate alternative types of magnetic order. A further alternative method of magnetisation measurement is that of a vibrating sample magnetometer (VSM), that uses a vibrating sample to generate a signal in the pick-up coils. As these methods were not used in any of the experiments presented in this thesis they will not be discussed further here.

2.3.2. Heat capacity

The heat capacity of a material is a measure of the energy released (or absorbed) upon cooling (or heating) at a specific temperature. A measurement of this value gives a direct indication of the density of states of the material at that moment. An integration over this value across a change in field or temperature equally gives a measure of the change in entropy. The total entropy of a system is a combination of several components: any conduction electron degrees of freedom; vibrational and phonon degrees of freedom; and spin degrees of freedom.

In a purely insulating material this is simplified to just lattice and magnetic degrees of freedom. If the magnetic contribution is of interest subtraction of the phonon component is best performed by comparison with a diamagnetic analogue. This is not always possible and so an approximate fit to the lattice contribution can be made using Debye or Einstein solid equation fits to the higher temperature region, where the heat capacity is dominated by the phonon contribution.[**12**]

For measurement of heat capacity a known mass of sample is mounted on a suspended platform, using a thin layer of thermally conductive lubricant to ensure good contact, such as *Apiezon-N* grease (figure 2.6). The platform is suspended by four wires that allow sample heating and temperature measurement. This platform is then mounted within a puck that acts as a thermal bath, and is mounted within a high-vac cryostat to minimise thermal effects from exchange gases. The sample is then heated whilst recording the temperature change as a function of heating power, followed by cooling whilst measuring. This heating-cooling cycle can then be fitted to give a total heat capacity of sample and platform, C_{total}, according to the following expression:

$$C_{\text{total}}\frac{dT}{dt} = -K_{\text{w}}(T - T_{\text{b}}) + P(t) \tag{2.2}$$

where K_w is the thermal conductance of the support wires; T_b is the temperature of the puck (thermal bath); and $P(t)$ is the supplied heating power (during the heating phase)[**13**]. The sample-only heat capacity can then be found by subtracting the platform contribution from a previously measured calibration table.

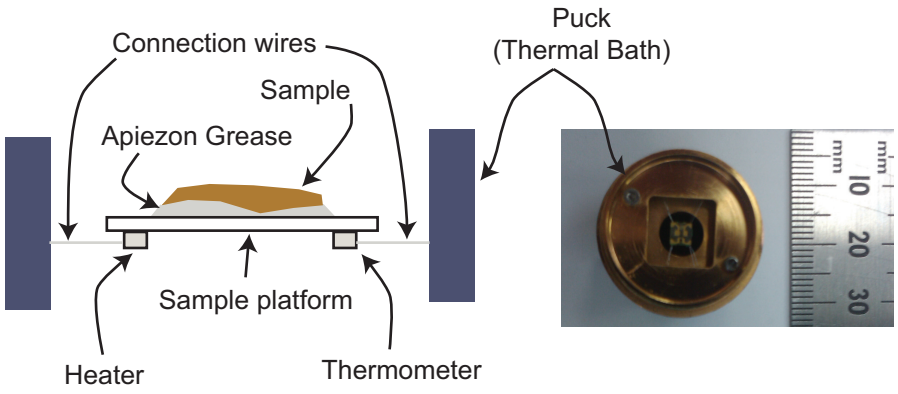

FIGURE 2.6. A schematic representation and phototograph of the sample platform and measurement puck used for heat capacity measurements within a Quantum Design PPMS.

2.4. Microscopy

In the study of the properties of solid state materials the degree of long range structural order is an important consideration. Microscopy can be an important tool in the determination of structural disorder in a polycrystalline material, or to gain insight into crystallite morphology. In this section the microscopy techniques used in the production of this thesis will be discussed.

2.4.1. Scanning electron microscopy

Scanning electron microscopy is an extremely powerful technique for imaging nanometre scale micro-structure. The instrument relies on the scattering of a focused beam of high energy electrons that are scanned across the surface of a sample, producing high resolution images. Due to the nature of the technique, the sample must be held under high vacuum for image acquisition. Additionally, to prevent charge build-up, insulating samples must be coated with a conducting layer of sputtered carbon or gold.

The electron beam is usually focussed to a size of $\sim$ 1 nm and scanned across the surface of a sample, detecting secondary scattered electrons emitted from the sample. An image is created by collecting a raster-scan pattern as the beam is quickly scanned

across the surface of interest. Due to the size of the focusing spot, a large depth of field is achieved providing images with a characteristic 3-dimensional appearance to them. This property is extremely useful when attempting to characterise the surface structure of a sample.

As well as being used for imaging, SEMs can also be fitted with energy dispersive X-ray detectors for compositional analysis. Due to the characteristic emission wavelengths of each element (briefly discussed in section 2.2.1), energy dependent analysis of the emitted X-rays upon excitation by the beam can give information about the elements present. For quantitative analysis the instrument must first be calibrated using standards and the spectrum is best collected from a flat, polished sample surface. When the elements of interest have similar electron counts, Z, emission-line overlap can complicate analysis. This method is also considerably less sensitive for the lighter elements with low Z.

For the images produced in this thesis a Jeol JSM-6480LV microscope was used under high-vacuum and at room temperature.

References

[1] Hahn, T. (Ed.) *International Tables of Crystallography Volume A: Space-Group Symmetry* Kluwer Academic Publishers (London), **2002**.

[2] Dinnebier, R. E. (Ed.); Billinge, S. J. L. (Ed.); Le Bail, A.; Madsen, I.; Cranswick, L. M. D. *Powder Diffraction: Theory and Practice* Royal Society of Chemistry (London), **2008**.

[3] Young, R. A. *The Rietveld Method* Oxford University Press (USA), **1995**.

[4] Rietveld, H. M. *J. Appl. Cryst.*, **1969**, *2*, 65.

[5] Larson, A. C.; Von Dreele, R. B. *Los Alamos National Laboratory Report LAUR*, **2004**, 86.

[6] Rodriguez-Carvajal, J. *Physica B*, **1993**, *192*, 55.

[7] TOPAS (Version 4.1), program available from Bruker AXS, Östliche Reinbruckenstrasse 50, 76187 Karlsruhe, Germany.

[8] Solovyov, L. A.; Astachov, A. M.; Molokeev, M. S.; Vasiliev, A.D. *Acta Cryst.*, **2005**, *B61*, 435.

[9] Wang, J.; Toby, B. H.; Lee, P. L.; Ribaud, L.; Antao, S. M.; Kurtz, C.; Ramanathan, M.; Von Dreele, R. B.; Beno, M. A. *Rev. Sci. Instrum.*, **2008**, *79*, 085105.

[10] Cicognani, G. (Ed.) *The Yellow Book 2008: Guide To Neutron Research Facilities*, Available from:www.ill.eu/instruments-support/instruments-groups/yellowbook/, **2008**.

[11] *Magnetic Property Measurement System: DC-SQUID User's Manual*, Available from: Quantum Design, 11578 Sorrento Valley Rd., San Diego, CA 92191-1311, USA **2000**.

[12] Kittel, C. *Introduction to Solid State Physics, 7th Ed.* Wiley (London), **1996**.

[13] *Physical Property Measurement System: Heat Capacity Option User's Manual, 11th Ed.*, Available from: Quantum Design, 11578 Sorrento Valley Rd., San Diego, CA 92191-1311, USA **2004**.

CHAPTER 3

'Mg-herbertsmithite', γ-$MgCu_3(OH)_6Cl_2$

3.1. Introduction

Despite long-standing questions over the ground-state of the $S = \frac{1}{2}$ kagome lattice no model material has yet been found that truly encapsulates the simplicity of the theoretical models. In order to resolve this enduring problem of solid-state physics the challenge lies with the experimental chemists. It could be that in reality there is no material that is completely free from some form of deviation from the ideal model, but in either case the only way to resolve this issue is to build a library of materials for study. With this library it will eventually be possible to identify the underlying properties that are intrinsic to the physics of the $S = \frac{1}{2}$ kagome lattice, differentiating these from the properties induced in each material by the different deviations from ideality.

At present the candidate material considered to be the best approximation to an ideal kagome lattice is herbertsmithite, γ-$ZnCu_3(OH)_6Cl_2$, furthermore referred to as 'Zn-herbertsmithite' for clarity.[**1**] 'Zn-herbertsmithite' is a member of the paratacamite family of minerals which has the general formula $Zn_x[Cu_{4-x}(OH)_6]Cl_2$, where x lies in the range $0 < x < 1$. Herbertsmithite is defined as the $x = 1$ end-member, with near ideal kagome planes, whilst the $x = 0$ end-member clinoatacamite contains a pyrochlore-like lattice of Cu^{2+} ions, also of interest as a frustrated magnet.[**2, 3, 4, 5**] The intermediate region, where $0.33 < x < 1$ is referred to as paratacamite and contains both kagome lattice occupation, and partial occupation of the inter-planar site by magnetically active Cu^{2+}.[**6, 7**] This occupation provides a 3-dimensional exchange pathway, potentially coupling the kagome planes.

To increase our library of kagome magnets it is worth considering the chemical flexibility of the herbertsmithite crystal structure (shown in figure 3.1), and the possible substitution of alternative ions or groups within this lattice. Herbertsmithite is built from Cu^{2+}, Zn^{2+} and Cl^- ions as well as $(OH)^-$ groups. The Cu^{2+} ions make up the $S = \frac{1}{2}$ kagome lattice and so must not be exchanged. The Cl^- group can be exchanged for alternative halides, such as Br^- or I^-, but the 3-dimensionally bound

herbertsmithite structure is too constrained for these larger ions and a more flexible 2-dimensional structure is chosen.[**8, 9**] This 2-dimensional structure is discussed further in chapters 4 and 5. Alternatively, the $(OH)^-$ groups could be exchanged for some other ion or group such as F^-, but attempts at this substitution are yet to be performed. Finally, the remaining group to be discussed is the diamagnetic Zn^{2+} group. Mineralogical studies of the paratacamites suggest that several different ions are capable of residing on the site, including Ni^{2+}, Co^{2+}, Fe^{2+}, Cd^{2+} and Mg^{2+}.[**6, 10**] The first three of these are magnetically active and so would further complicate the magnetism, rather than leaving an ideal $S = \frac{1}{2}$ kagome lattice. The 4^{th}, Cd^{2+}, has not yet been studied, and due to its impracticality for study with neutron techniques from the large absorption effects of Cd, has not been attempted here. This leaves substitution of Mg^{2+} for the Zn^{2+} ions. The extremely similar ionic radii of octahedral Mg^{2+} to both Cu^{2+} and Zn^{2+}, with 0.72, 0.73 and 0.74 Å respectively,[**11**] suggests a compatibility with the site, and recently published studies show its incorporation into the paratacamite crystal structure, with occupancies in the range $0.33 \leq x \leq 0.75$.[**12**]

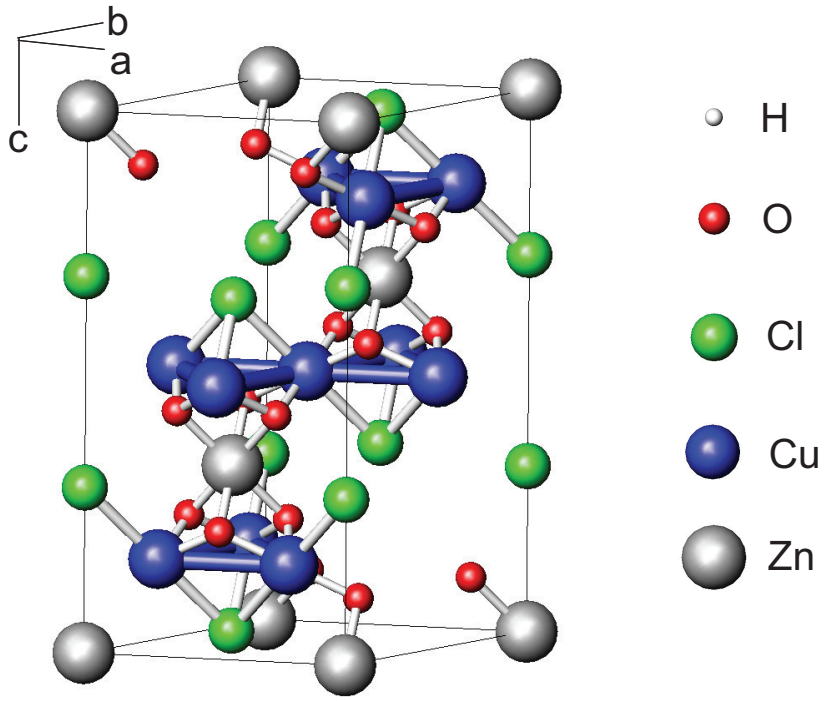

FIGURE 3.1. The crystal structure of herbertsmithite showing well separated kagome planes of $S = \frac{1}{2}$ Cu^{2+} ions, created by the controlled doping of Zn^{2+} onto a pyrochlore-like lattice.

This chapter presents synthesis, structural refinements and preliminary magnetic characterisation of the $x \sim 1$ end-member, 'Mg-herbertsmithite' γ-$MgCu_3(OH)_6Cl_2$.

The work was carried out by myself together with the M.Sci. student Alex Sinclair (UCL), whom I supervised.

3.2. Synthesis

Taking inspiration from its Zn-based analogue herbertsmithite,[**1**] and the lower-doped 'Mg-paratacamites', [**12**] 'Mg-herbertsmithite' is synthesised by hydrothermal reaction of basic-copper carbonate with an aqueous solution of magnesium chloride according to the following scheme:

$$3Cu_2(OH)_2(CO_3)_{(s)} + 2MgCl_{2(aq)} + 3H_2O \rightarrow 2Cu_3Mg(OH)_6Cl_{2(s)} + 3CO_{2(g)} \quad (3.1)$$

The aqueous solution of magnesium chloride was prepared by dilution of a 3 M stock solution. A 10 ml aliquot of the magnesium chloride solution was then added to 660 mg (2.7 mmol) of finely ground $Cu_2(OH)_2(CO_3)$ in a 20 ml PTFE-lined, steel hydrothermal reaction bomb. The bomb was heated to 190°C at a rate of 0.1°C min^{-1}, left for 24 hrs, then cooled to room temperature at 0.1°C min^{-1}. The resultant polycrystalline product was washed with water (3 × 10 ml) and acetone (3 × 10 ml) before being dried in air. This process was repeated with magnesium chloride solution strengths in the range $0.25 < [MgCl_2] < 4$ M, and each product was analysed by laboratory X-ray diffraction for phase purity and Mg-content, using the department's *Bruker D8 Advance* diffractometer.

3.3. Structural characterisation

3.3.1. Laboratory X-ray diffraction

Qualitative phase analysis of the collected diffraction patterns found that below $[MgCl_2] = 0.7$ M the reaction products were increasingly dominated by a CuO impurity phase. Conversely, above $[MgCl_2] = 3$ M, a crystallographic polymorph of herbertsmithite, haydeeite α-$MgCu_3(OH)_6Cl_2$, contaminated the product.[**13, 14**] In the intermediate region, the product was found to be single phase within the resolution of the instrument, and could be fitted to the structure of the desired product 'Mg-herbertsmithite', α-$Mg_xCu_{4-x}(OH)_6Cl_2$ with $x \sim 1$. The resolution of the collected diffraction patterns (figure 3.2a.) are seen to be instrument-limited, indicating a highly crystalline, well ordered product.

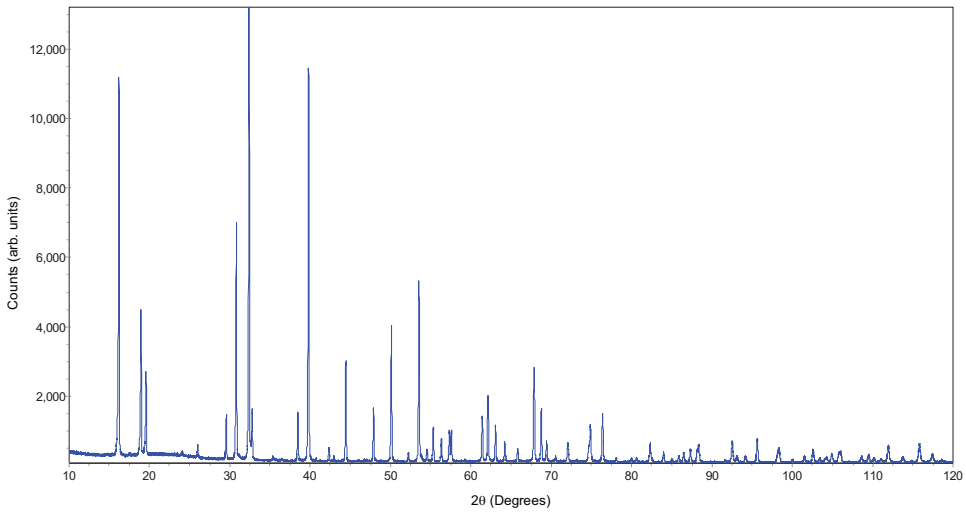

FIGURE 3.2. A representative laboratory X-ray diffraction pattern of a Mg-herbertsmithite sample, using a *Bruker D8 Advance* diffractometer with a monochromated Cu K_α source, showing instrument-limited resolution as well as Mg-herbertsmithite phase purity.

3.3.2. Scanning Electron Microscopy

To confirm the crystallinity, phase purity and crystal morphology; a sample of 'Mg-herbertsmithite' was examined by Scanning Electron Microscopy (SEM). The resultant images show 3-dimensional crystallites with well defined facets (figure 3.3). The crystallites vary in size, ranging from 0.5 – 10 μm^3, and there is no evidence of amorphous phase-impurities that would be otherwise unobservable by diffraction techniques.

3.3.3. Synchrotron powder X-ray diffraction

Analysis of the laboratory X-ray diffraction patterns found samples prepared using reaction solutions with the range $0.8 < [MgCl_2] < 1.8$ M showed refined Mg contents closest to the idealised $x = 1$ required for a structurally perfect kagome lattice (figure 3.2). High resolution diffraction patterns, of several samples across this range, were collected using the synchrotron X-ray beamline 11-BM at the Advanced Photon Source.[**15**] Samples labelled **1**–**6** represent products crystallised from solutions of $[MgCl_2]$ = 0.8, 1.0, 1.2, 1.4 and 1.6 respectively. All samples were loaded into 0.8 mm (ID) *Kapton* tubes and attached to the sample stubs. The patterns were then collected at $T = 295$ K with an incoming, monochromated, X-ray wavelength of $\lambda = 0.412260$ Å. Rietveld refinements of each samples structural parameters, using this high-resolution data, are discussed in section 3.3.5.

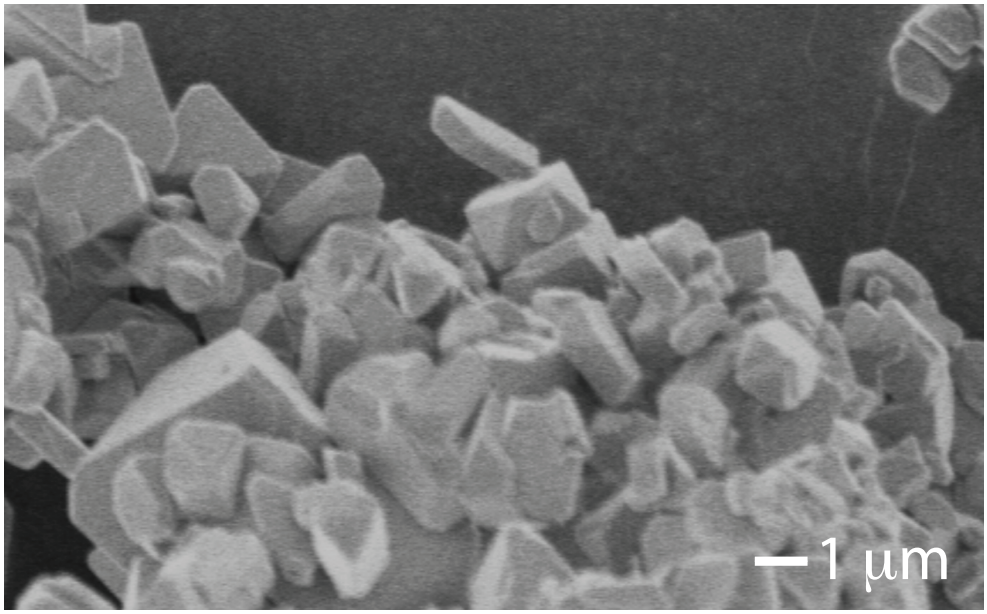

FIGURE 3.3. SEM images of 'Mg-herbertsmithite', showing good 3-dimensional crystallinity and no sign of amorphous impurity phases.

3.3.4. Powder neutron diffraction

One sample, prepared using deuterium oxide in place of water with a $[MgCl_2] = 1.2$ M (referred to as $\mathbf{2_D}$), was used for the collection of temperature-dependent time-of-flight neutron diffraction data. This complimentary technique allows: a high quality refinement of the deuterium (hydrogen) positions, an important site when considering hybridisation of the oxygen mediating the Cu–O(H/D)–Cu superexchange pathway[**16, 17**]; the observation of any temperature-driven structural changes that could affect the magnetic lattice; and any changes in the magnetic scattering that could evidence the build up of short-range correlations, or long-range magnetic order. The WISH *time-of-flight* diffractometer at ISIS, UK was used for pattern collection (prior to commissioning of the solid-methane moderator). A 1 g sample of $\mathbf{2_D}$ was loaded into a thin-walled, 6 mm, vanadium sample can and inserted into a standard Oxford-Instruments ^{4}He cryostat. Diffraction patterns were then collected at $T = 2, 10$ and 50 K. The structural refinements and results are discussed in section 3.3.5.

3.3.5. Structural refinement

In order to gain structural information from the diffraction data, Rietveld refinements were performed using the programs TOPAS and FullProf for synchrotron X-ray and and neutron data-sets respectively.[**18, 19**] A representative example of the achieved

fit and refined structural parameters, for sample **2**, are shown in figure 3.4 and table 3.1. The fit and structural parameters achieved from refinement of the $T = 1.5$ K powder neutron diffraction pattern are shown in figure 3.5 and table 3.1 (Fits and refined structural parameters for synchrotron X-ray refinements of all samples **1**–**6** are presented in appendices A and B respectively).

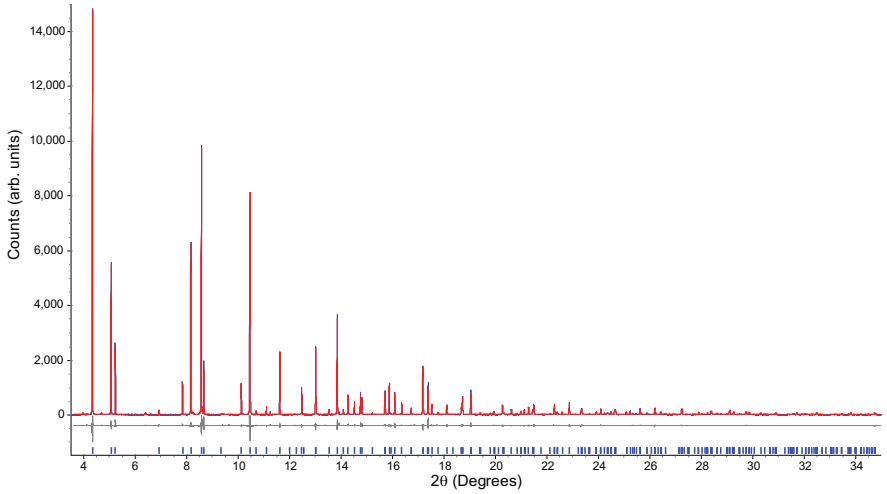

FIGURE 3.4. Rietveld refinement, using TOPAS, of synchrotron powder X-ray diffraction data for Mg-herbertsmithite, α-$Mg_xCu_{4-x}(OH)_6Cl_2$, sample **2**, at $T = 295$ K using X-rays of wavelength $\lambda = 0.412260$ Å. The red line is the data, blue line the fit, lower grey line the difference and the tick marks represent reflection positions. The final goodness-of-fit merit factor, χ^2, was 2.228.

Just as in Zn-herbertsmithite, the structure is composed of a pyrochlore-like lattice of metal ions, where Cu^{2+} preferentially reside on the Jahn-Teller distorted kagome ($9d$) sites leaving occupation of the triangular ($3a$) sites by Mg^{2+}. Each triangle of the kagome lattice ($9d$ sites) can be thought of as making up the basal unit of a tetrahedron, with the interlayar ($3a$) site at its apex. Capping the face of the basal unit is a μ_3–Cl^- ion, and each other face of the tetrahedron is capped by a μ_3–O(H) group.

Refined structural parameters show only minor variations across the series **1** − **6**, uncorrelated with any changes in [$MgCl_2$] solution concentration. Of particular consideration are the bond lengths and angles involved in Cu–O(H/D)–Cu super-exchange. Figure 3.6 clearly shows no systematic change across the series.

Upon cooling, no evidence was seen of a structural phase transition and table **??** shows only a weak thermal lattice contraction in the c axis, coupled with a minor

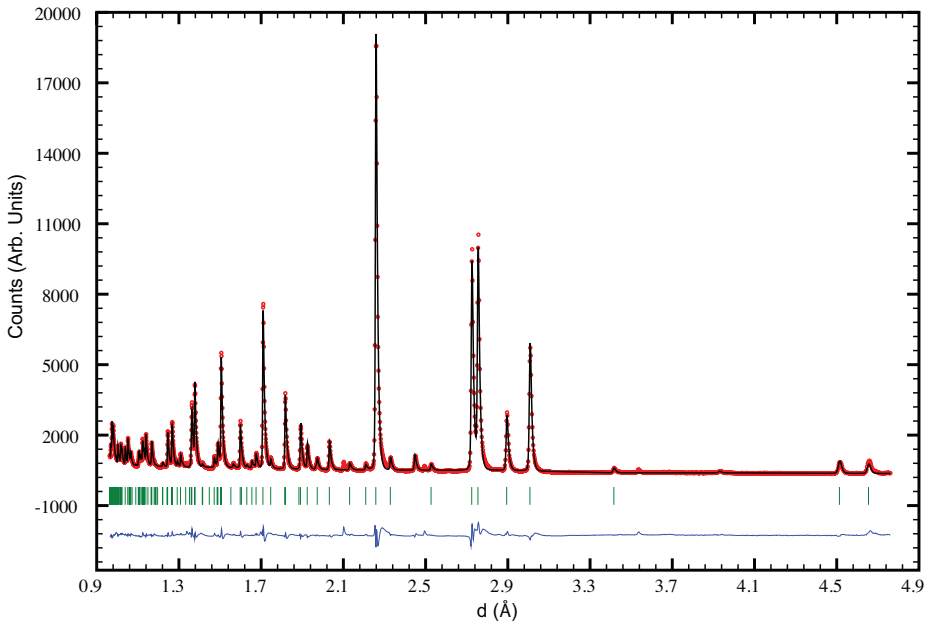

FIGURE 3.5. Rietveld refinement, using Fullprof, of powder neutron diffraction data for deuterated Mg-herbertmithite, α-$Mg_xCu_{4-x}(OD)_6Cl_2$, sample $\mathbf{2_D}$, at $T = 1.5$ K using the WISH time-of-flight diffractometer. The red line is the data, black line the fit, lower blue line the difference and the tick marks represent reflection positions. The final goodness-of-fit merit factor, χ^2, was 9.95.

expansion of the a axis. Only a minimal perturbation to the crystal structure upon hydrogen/deuterium exchange was noticed.

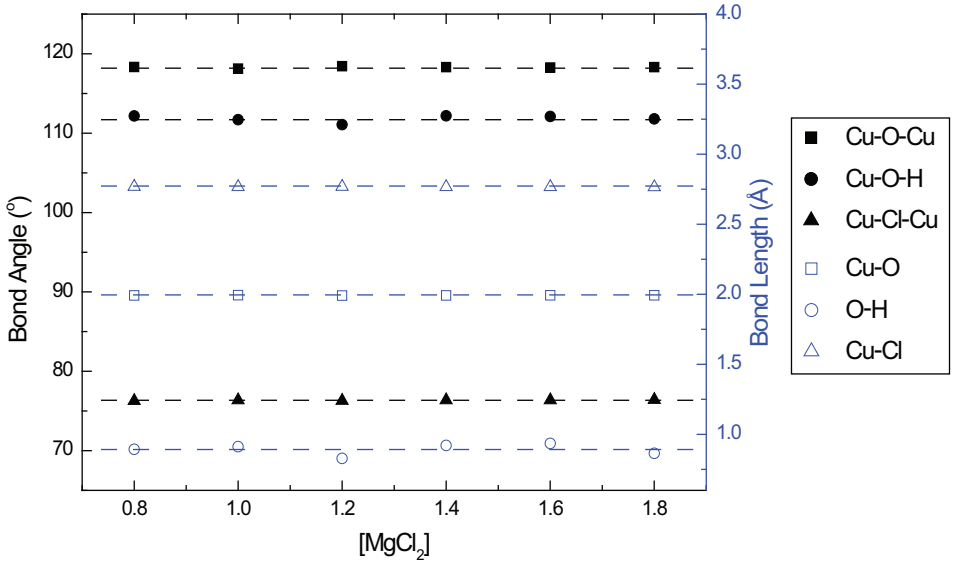

FIGURE 3.6. Selected bond lengths and angles for Mg-herbertsmithite, γ-$Cu_{4-x}Mg_x(OH)_6Cl_2$, samples **1**–**6**, showing no systematic change across the series.

TABLE 3.1. The refined crystallographic parameters for: top, 'Mg-herbertsmithite' sample **2** in the hexagonal setting of the space group $R\bar{3}m$ at T = 295 K, using synchrotron X-rays of λ = 0.412260 Å. The final goodness-of-fit merit factor, χ^2, was 2.228; middle, anisotropic thermal parameters for the synchrotron refinement and * showing U_{iso} for hydrogen; and bottom, deuterated-'Mg-herbertsmithite' sample $\mathbf{2_D}$ at T = 1.5 K, using data collected on the WISH time-of-flight diffractometer. The final goodness-of-fit merit factor, χ^2, was 9.95.

Wyckoff Site	Atom Name	x	y	z	Occupation
9d	Cu, Mg	$\frac{1}{3}$	$\frac{1}{6}$	$\frac{1}{6}$	0.955(3), 0.045(3)
3a	Mg, Cu	0	0	0	0.827(9), 0.173(9)
6c	Cl	0	0	0.30483(4)	1
18h	O	0.12778(6)	0.25557(12)	0.10396(6)	1
18h	H	0.2021(11)	0.404(2)	0.0870(10)	1

Site	U_{11} (U_{iso}*)	U_{22}	U_{33}	U_{12}	U_{13}	U_{23}
Cu , Mg	0.00536(6)	0.00536(6)	0.00816(11)	0.00268(3)	0	0
Mg , Cu	0.0064(2)	0.0064(2)	0.0011(4)	0.0032(1)	0	0
Cl	0.0163(17)	0.0163(17)	0.00100(3)	0.0082(9)	0	0
O	0.0078(3)	0.0078(3)	0.0129(5)	0.0039(2)	0	0
H*	0.049(5)	-	-	-	-	-

Site	x	y	z	Occupation	B_{iso}
Cu, Mg	$\frac{1}{3}$	$\frac{1}{6}$	$\frac{1}{6}$	0.86(3), 0.14(3)	0.060(7)
Mg, Cu	0	0	0	0.78(4), 0.22(4)	0.012(14)
Cl	0	0	0.30516(13)	1	0.026(7)
O	0.1275(4)	0.2550(9)	0.10443(16)	1	0.019(5)
D, H	0.2029(4)	0.4058(8)	0.07648(16)	1.000(4), 0.000(4)	0.0464(9)

TABLE 3.2. A comparison of the refined unit cell parameters for Mg-herbertsmithite (**2**) and deuterated Mg-herbertsmithite ($\mathbf{2_D}$), γ-$Cu_{4-x}Mg_x(OH/D)_6Cl_2$, as a function of temperature.

Sample	Temperature (K)	Cell parameter (Å)	
		$a = b$	c
2	295	6.838861(11)	14.02125(3)
$\mathbf{2_D}$	50	6.83688(18)	13.9792(4)
$\mathbf{2_D}$	10	6.83689(18)	13.9792(4)
$\mathbf{2_D}$	1.5	6.83703(18)	13.9780(4)

Refined bond lengths and angles for samples **2** and $\mathbf{2_D}$ can be seen in tables 3.3 and 3.4, respectively. For comparison, 3.2 and 3.4 also contain literature structural information for deuterated Zn-herbertsmithite, refined using high-resolution powder neutron diffraction data.[**7**]

TABLE 3.3. A comparison between selected refined bond lengths for protonated, H (sample **2**), and deuterated, D (sample $\mathbf{2_D}$) 'Mg-herbertsmithite', γ-$Cu_3Mg(OH)_6Cl_2$, with those of Zn-herbertsmithite.[**7**]

Bond	Length (Å)		
	Mg-herbertsmithite		Zn-herbertsmithite[**7**]
	(H)	(D)	
$Cu–Cu_{intra\text{-}plane}$	3.41943(5)	3.41848(9)	3.419
$Cu–Cu_{inter\text{-}plane}$	5.07360(8)	5.06014(12)	5.084
Cu–O(H/D)	1.9933(4)	1.988(3)	1.985
Mg(Zn)–O(H/D)	2.1014(8)	2.100(2)	2.109
O–H/D	0.954(13)	0.975(3)	0.975
Cu–Cl	2.7659(4)	2.7646(13)	2.763

TABLE 3.4. A comparison of selected refined bond angles for protonated, H (sample **2**), and deuterated, D (sample $\mathbf{2_D}$) 'Mg-herbertsmithite', γ-$Cu_3Mg(OH)_6Cl_2$, with those of Zn-herbertsmithite.[**7**]

Bond	Angle (°)		
	Mg-herbertsmithite		Zn-herbertsmithite[**7**]
	(H)	(D)	
Cu–O(H/D)–Cu	118.12(4)	118.59(12)	118.89
Cu–O(H/D)–Mg(Zn)	96.64(2)	96.60(11)	96.82
Cu–O–H	111.7(4)	114.6(3)	114.88

The sizeable differences in the atomic scattering factors of Cu^{2+} and Mg^{2+} allow the metal site occupancies to be reliably refined using X-ray and neutron diffraction data. With only the assumption that the total site occupation was unity, the X-ray refinements were found to be stable but not to give unique solutions. Additional constraints were therefore applied to fix the total Mg-Cu ratios to be the same as those determined by ICP-AES elemental analysis for samples $\mathbf{1}-\mathbf{6}$ (3.7a). The site occupancies of the deuterated sample (sample $\mathbf{2_D}$) refined to stable, unique values without this constraint. Refined occupancies for samples $\mathbf{1}-\mathbf{6}$ of the kagome ($9d$) and intra-layer triangular (3a) sites are shown in (3.7b). Just as in 'Zn-herbertsmithite',[**7, 1**] the Jahn-Teller active Cu^{2+} ions display a preference for the distorted octahedron of the kagome ($9d$) sites over the symmetric coordination of the triangular anti-prism sites ($3a$) that separate the kagome planes. The deuterated sample ($\mathbf{2_D}$) shows a larger deviation from ideality despite being synthesised identically to that of **2**, suggesting that D/H isotopic effects may be at play during crystallisation.

The crystallographic refinements indicate that the kagome sites ($9d$) are occupied by ~ 95 % Cu^{2+}, with a small increase in the dilution of the kagome sites by Mg^{2+} across samples **1** - **6**, from 4.39(4) % to 5.45(4) %. Quite different behaviour is seen for the

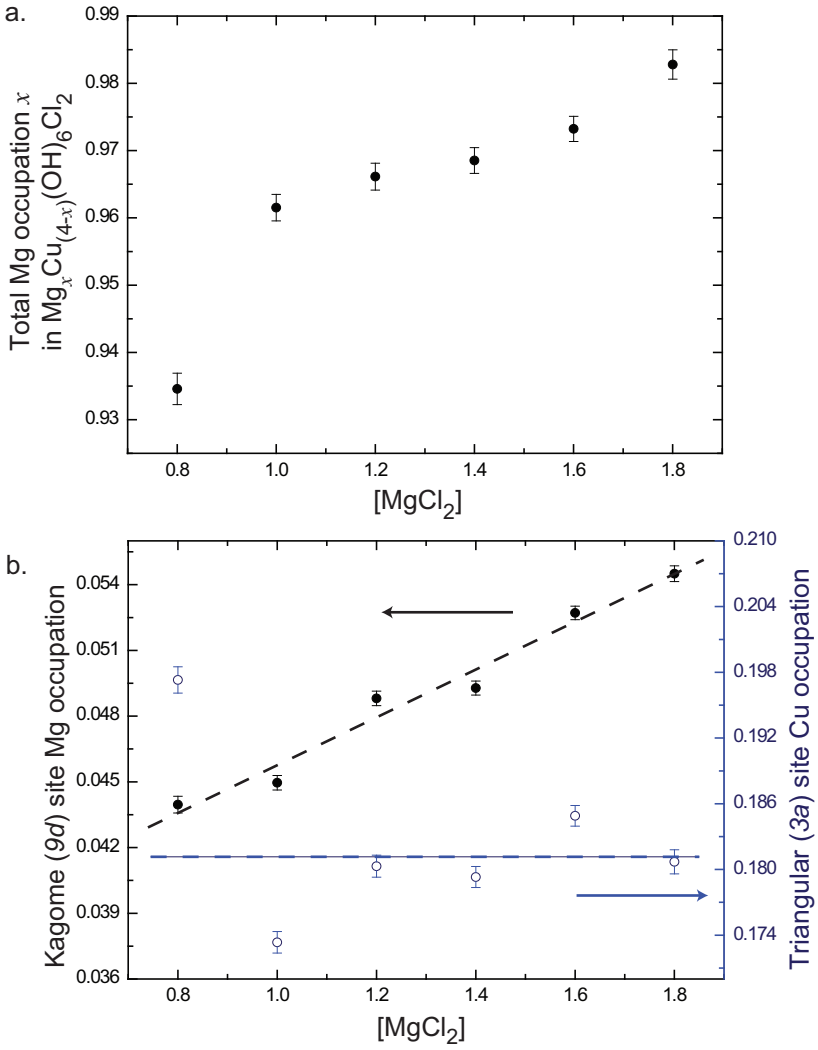

FIGURE 3.7. a. The total Mg occupation, x, in the formula γ-$Cu_{4-x}Mg_x(OH)_6Cl_2$, shows a slightly lower than idealised $x = 1$ occupation of diamagnetic Mg^{2+} onto the $S = \frac{1}{2}$ Cu^{2+} pyrochlore-like lattice, with a trend of increasing x as [$MgCl_2$] concentration is increased towards the $x = 1$ idealised stoichiometry. b. Refined Mg^{2+} occupation on the kagome (9d) site (left) and Cu^{2+} occupation of the triangular (1a) site (right). A positive trend can be seen in diamagnetic dilution of the kagome lattice upon increasing solution concentration. Conversely there is no systematic change, upon increasing solution concentration, in the Cu^{2+} occupation of the triangular (3a) site.

refined occupancy of the triangular (3a) site: this shows little variation across the series; the occupation by Cu^{2+} has an average value of 18.3(8) %. This occupation value of the triangular (3a) site by the magnetic ions is important when considering the dimensionality of the magnetism in the herbertsmithites, as it is the presence of Cu^{2+} on this site that can lead to coupling between the kagome planes, destroying

the local 2-dimensionality. We note that our refined diamagnetic occupation of the triangular ($3a$) site in 'Mg-Herbertsmithite' is within the range reported for the isomagnetic 'Zn-herbertsmithite'.[**7**]

These results contrast to those recently reported from laboratory X-ray refinements of small single crystals of Mg-paratacamites, γ-$Cu_{4-x}Mg_x(OH)_6Cl_2$, with total Mg occupancies that range from $x = 0.33$ to 0.75.[**12**] For the three samples of this series, only variation in the Mg^{2+} occupation of the triangular ($3a$) site was seen; the kagome ($9d$) site remained completely occupied by $S = \frac{1}{2}$ Cu^{2+} ions for all values of [$MgCl_2$]. The difference in the occupations of our powder samples of 'Mg-herbertsmithite' and the single crystals of the 'Mg-paratacamites' is likely to be a consequence of the dissimilar reaction conditions: our powder samples were prepared over a 48 hr period, while the single crystals were grown over 45 weeks.[**12**] The latter would therefore be expected to display occupancies that are closer to the thermodynamic limit.

3.3.6. Magnetic scattering

No sign of magnetic Bragg peaks, diffuse scattering, or changes in the background paramagnetic scattering were seen across the entire temperature range. The absence of any changes in the magnetic scattering is suggestive of the material remaining in a magnetically-dynamic, spin-liquid state through this entire temperature regime. Changes to the scattering from the $S = \frac{1}{2}$ moments could simply be too weak to observe, but recently published data on a similar $S = \frac{1}{2}$ kagome magnet, vesignieite, displays a clear loss of paramagnetic scattering upon cooling, suggesting that a magnetic transition in 'Mg-herbertsmithite' would be observable.[**20**]

3.4. DC SQUID magnetometry

3.4.1. Susceptibility *vs.* temperature measurements

Zero-field-cooled (ZFC) and field-cooled (FC) magnetic susceptibility (χ) measurements, of samples **1** − **6**, were taken in a field of 100 Oe with a Quantum Design MPMS-7 SQUID magnetometer (3.8). Fits of the linear region of the inverse susceptibility, over the temperature range $100 < T < 300$ K, yielded large negative Weiss temperatures of $\theta_W \simeq -284(23)$ K, a value that is close to those that have been found in 'Zn-herbertsmithite', $\theta_W = -301$ K (Curie-Weiss fits for the entire series are given in appendix C).[**22, 1**] On cooling below $T \sim 100$ K, downwards curvature develops in $\chi^{-1}(T)$ indicating the formation of ferromagnetic spin-spin

correlations, such behaviour is a familiar characteristic of both classical and quantum kagome systems.[**13, 23, 24, 25, 26, 27**] It is only upon cooling to far lower temperatures that a transition is observed as a rapid increase in χ below $T_C \simeq 4.5$ K, accompanied by bifurcation of ZFC and FC data. If this transition were from the herbertsmithite phase, its strong suppression, $|\theta_W|/T_C \sim 66$, would indicate that 'Mg-herbertsmithite' is indeed a highly frustrated magnet.[**28**] However, the apparently random value of the low temperature magnetisation plateau in $\chi(T)$ (inset of figure 3.8a.), with respect to [$MgCl_2$], Cu/Mg site mixing, or other crystallographic parameters raises the question of whether this transition is from an impurity rather than the 'Mg-herbertsmithite' phase.

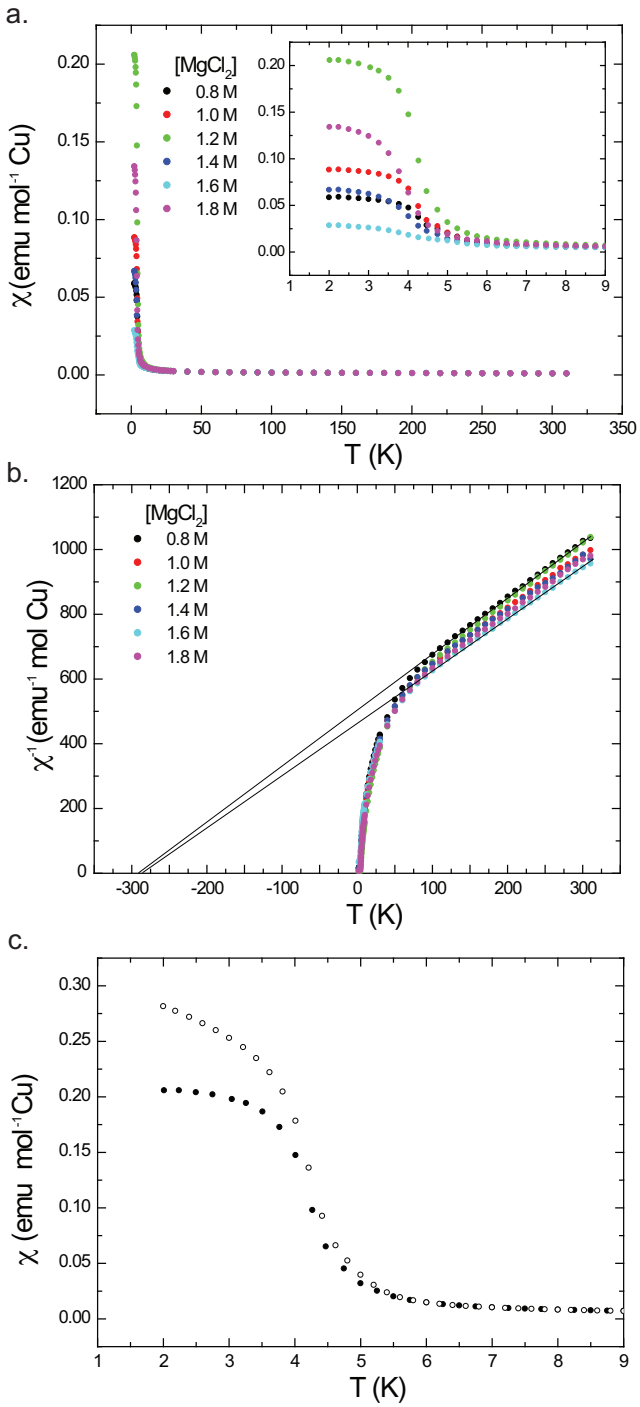

FIGURE 3.8. a) Zero-field-cooled magnetic susceptibility of samples **1** − **6** measured in a 100 Oe field. A rapid increase is seen below $T_C \sim 4.5$ K, suggestive of a ferromagnetic transition. Inset shows a blow-up of the low T region, where the saturation value does not appear to follow a trend across the series of samples. b) Inverse susceptibility, showing a large-negative intercept of Curie-Weiss fits to the high temperature region ($100 > T > 300$ K), with all samples giving similar values of $\theta_W = -284(23)$ K. c) Zero-field-cooled (•) and field-cooled (○) susceptibility for sample **3** showing bifurcation during the transition at $T_C \sim 4.5$ K.

3.4.2. Magnetisation *vs.* field measurements

In an effort to determine the nature of the ferromagnetic component, measurements of the magnetisation, M, were recorded for each of the samples **1** − **6** in fields, H, between -7 and 7 T at several temperatures above and below the $T_C \sim 4.5$ K transition. All data exhibit a typical paramagnetic-like response, with the development of an additional ferromagnetic hysteresis opening below $T_C \sim 4.5$ K.

The paramagnetic response was fitted with a $S = \frac{1}{2}$ Brillouin function, $B_f(x)$.[**29**] Above the saturation field of the ferromagnetic component ($|H| > 1$ T), fits to $M = M_f + M_p B_f(x)$, where $B_f(x) = \mu_m(\coth(\frac{2J+1}{2J}x) - \frac{1}{2J}\coth(\frac{1}{2J}x))$, $x = \mu_m H/k_B T$ and $\mu_m = g_L \mu_B J$, g_L is the Landé g-factor, k_B is the Boltzmann constant, $J = \frac{1}{2}$ in the case of Cu^{2+}, and $M_{p,f}$ are the fitted saturation magnetizations of the paramagnetic and ferromagnetic components respectively. As can be seen in figure 3.9, the fit gave excellent agreement with the data, and allowed extraction of the ferromagnetic component (The resultant fits for all samples **1** − **6** can be found in appendix D).

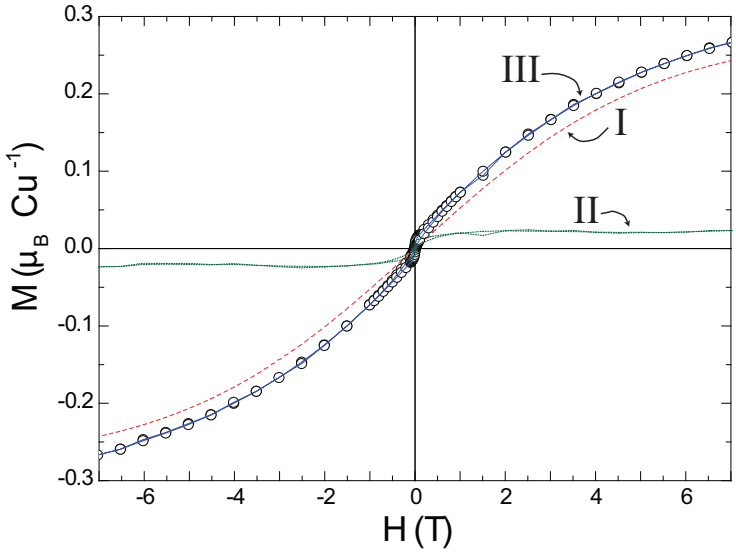

FIGURE 3.9. Magnetisation, M, against field, H, sweep at 2 K showing paramagnetic-like behaviour (○) for sample **1**, (I) fit to the $S = \frac{1}{2}$ Brillouin function, (II) the extracted ferromagnetic component, (III) and paramagnetic + ferromagnetic components showing excellent fit to the data.

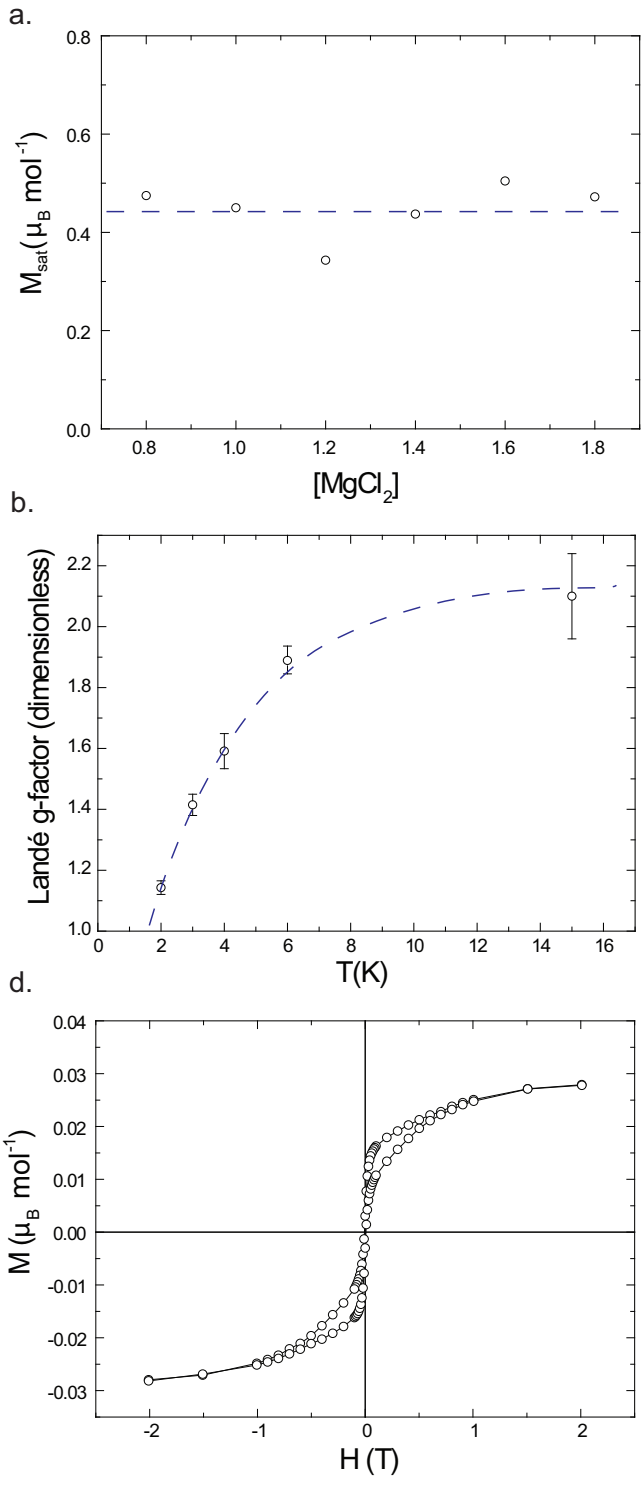

FIGURE 3.10. a. Fraction of the total spins showing paramagnetic behaviour as a function of [$MgCl_2$] for samples **1 - 6** at $T = 2$ K with a guide to the eye in blue, showing little composition dependence. b. The fitted Landé g-factor as a function of temperature, for sample **1**, showing the build-up of correlations below $T = 6$ K, with guide to the eye in blue indicating a high temperature limit of $g_L \sim 2.1$. c. The extracted ferromagnetic hysteresis for sample **1**, at $T = 2$ K, believed to be caused by a parasitic impurity phase.

The fit yielded a saturation magnetization of the paramagnetic component, M_p, at 2 K of ~ 0.45 $\mu_B mol^{-1}$(3.10a), well below the 3 $\mu_B mol^{-1}$ expected for the formula unit $Cu_3Mg(OH)_6Cl_2$ if all Cu^{2+} spins were contributing. At high temperature, ($T \geq$ 15 K) the fitted g-factor tends towards $g_L \sim 2.1$, a value similar to those seen in 'Zn-herbertsmithite',[**30, 31, 32**] but upon cooling below 6 K, the form of the Brillouin function changes and the fitted values of g_L reduce rapidly (3.10b.), indicating that below this transition the paramagnetic-like spins are no longer coupling to the field, but instead weakly coupled to neighbouring spins. The paramagnetic-like curvature was fitted with an alternative modified Brillouin function,[**33**] where the Landé g-factor was held at the value of a free electron and the temperature replaced with an effective temperature, $T_{eff} = T - T_W$. In all cases, the variable T_W (comparable to a Weiss temperature θ_W) refined to ~ -1.5 K, suggesting weakly antiferromagnetic interactions, in agreement with the reduction in g_L when the standard Brillouin function is used.

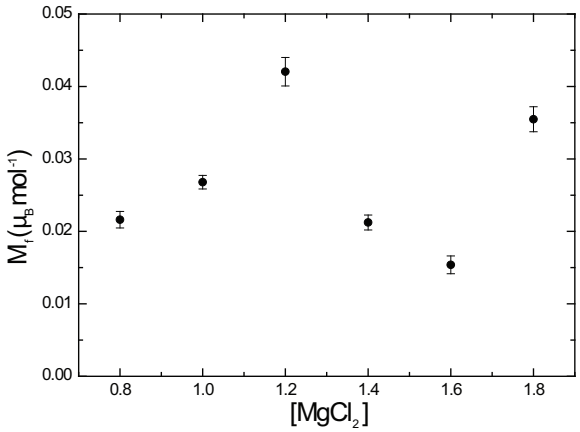

FIGURE 3.11. A plot of the fitted saturation value of the ferromagnetic component, M_f, across the series $\mathbf{1-6}$. The apparently random fluctuation in values suggests that this component is not related to changes in the crystal structure of the bulk sample, and as such may be from an additional ferromagnetic impurity phase.

Subtraction of the Brillouin function from the field-dependence of the magnetisation reveals a weak hysteresis that has a saturation value of $\sim 2.5 \times 10^{-2}$ $\mu_B.mol^{-1}$ and a coercive field of $\sim$ 100 G at $T = 2$ K (3.10d). This saturation value indicates that the ferromagnetic component represents only $\sim 1-2$ % of all Cu^{2+} in the sample. The apparently random variation in the size of the saturated ferromagnetic moment (seen in figure 3.11) supports the hypothesis that it is from varying amounts of an impurity rather than changes in the crystal structure, as the crystallographic refinements indicate that the latter correlate well with the synthesis conditions. The continued presence of the Brillouin function characteristic of paramagnetic-like spins

below the ferromagnetic transition requires that the two responses have different origins and is also compatible with the presence of a small amount of a ferromagnetic impurity. The constancy of the ferromagnetic ordering temperature across the 'Mg-herbertsmithite' (and paratacamite[**12**]) series suggests that the same impurity is involved in all these systems and explains why the samples of the Mg-paratacamite phases with $x = 0.33 - 0.75$, which feature far greater occupation of the triangular Mg^{2+} site by Cu^{2+}, also have transitions close to those found in 'Mg-herbertsmithite', $T_C \sim 4.5$ K *despite* featuring a large variation in Weiss temperatures.[**12**]

Looking now at the fits to the Brillouin function, comparison with 'Zn-herbertsmithite' [**30**] leads to the expectation that spins on the inter-plane triangular layer will be only weakly coupled with the spins of the kagome layer, creating a paramagnetic-like component, M_p, yet the size of M_p is close to 2.5 times that which would be expected if the spins involved were solely due to *free* Cu^{2+} on the triangular sites. It follows that if the Cu^{2+} ions on the triangular site are responsible, then they are ferromagnetically coupled to some of the spins in the neighbouring kagome layers to create superparamagnetic clusters of spins. In the 'Mg-herbertsmithites' presented in this study there are few such clusters, but larger quantities of Cu^{2+} on the triangular site will correspondingly lead to a lessening of the antiferromagnetic mean field and a reduction in the magnitude of the Weiss temperature, a behaviour that has been seen in the 'Mg-paratacamites'.[**12**] The reduction in g_L at low temperature indicates that these clusters cannot be considered as free, but instead are weakly antiferromagnetically coupled. Extension of the clusters beyond the spins of the triangular site requires that they are coupled to the spins of the kagome lattice. The coupling between spins on the triangular sites is far weaker than the value of $\theta_W = -284(23)$ K, observed from the high-temperature bulk susceptibility that involves all of the spins within the structure. The retention of Brillouin-like behaviour at all temperatures indicates that this coupling stiffens the fluctuations of the superparamagnetic clusters but does not freeze them – a behaviour that requires the kagome spins to remain dynamic at low temperature and for these to be in a quantum spin liquid state.

3.5. Conclusions

This chapter presents the crystallographic and magnetic studies of the new model kagome magnet 'Mg-herbertsmithite', γ-$Cu_{4-x}Mg_x(OH)_6Cl_2$. High resolution diffraction studies using both synchrotron X-rays and neutrons find the samples to have near-ideal Mg content in the range $0.93 < x < 0.98$, with no significant changes in the crystal structure across this doping range. Measurements of the temperature

dependence of the magnetic susceptibility show a large negative Weiss temperature $\theta_W = -284(23)$ K, comparable to that of 'Zn-herbertsmithite', suggesting strong antiferromagnetic superexchange. Despite this, a small ferromagnetic ordering is observed at $T_C \sim 4.5$ K in all samples. By fitting measurements of magnetisation *vs.* temperature, this ferromagnetic ordering component is confidently assigned to an impurity phase. The extracted response from the 'Mg-herbertsmithite' phase shows no evidence of a magnetic transition down to 1.8 K and low-temperature magnetometry measurements suggest the formation of a quantum-spin-liquid ground-state.

3.6. Future work

To further characterise the ground-state of this material, local probes will be key to definitively assign the origin of each discussed response. Muon spin relaxation (μSR) is a particularly powerful local-probe technique for determining low temperature spin dynamics, and in collaboration with Prof. P. Mendels and Dr. F. Bert (University of Orsay), analysis of measurements performed on these samples is currently under way. Additionally, ^{17}O-NMR measurements have been shown to be a direct probe of the local kagome susceptibility of 'Zn-herbertsmithite',[**34**] but prior to synthesising suitably enriched samples the synthesis must be considerably scaled down due to the high cost of ^{17}O-enrichment. Further probing the exotic physics of the quantum-spin-liquid ground-state within this material, inelastic neutron scattering could be an insightful technique. Ultimately, a huge amount more information could be learnt from each of these techniques if they were performed on single crystals, without the complications of powder averaging. As such a concerted synthetic effort should be made to optimise conditions for their growth. This has recently been achieved with 'Zn-herbertsmithite', although samples are still too small for detailed neutron scattering experiments.[**35**]

References

[1] Shores, M. P.; Nytko, E. A.; Bartlett, B. M.; Nocera, D. G. *J. Am. Chem. Soc.* **2005**, *127*, 13462.

[2] Zheng, X.; Kawae, T.; Kashitani, Y.; Li, C.; Tateiwa, N.; Takeda, K.; Yamada, H.; Xu, C. N.; Ren, Y.*Phys. Rev. B* **2005**, *71*, 052409.

[3] Wills, A. S.; Perring, T. G.; Raymond, S.; Fåk, B.; Henry, J. Y., *J. Phys.: Conf. Ser.*, **2009**, *145*, 012056.

[4] Wills, A. S.; Henry J. Y., *J. Phys. Condens, Mater.*, **2008**, *20*, 472206.

[5] Wills, A. S.; Raymond, S; Henry, J. -Y. *J Magn. Magn. Mater.*, **2004**, *272*, 850-851.

[6] Braithwaite, R.S.; Mereiter, K.; Paar, W. H.; Clark, A. M. *Mineral. Mag.* **2004** *68*, 527.
[7] Pollard, R. A.; Thomas, R. G.; Williams, P. A. *Mineral. Mag.* **1989**, *53*, 557.
[8] Zheng, X. G.; Yamashita, T.; Hagihala, M.; Fujihala, M.; Kawae, T. *Physica B: Cond, Mat.* **2009**, *404*, 680.
[9] Zheng, X., G.; Mori, T.; Nishiyama, K.; Higemoto, W.; Yamada, H.; Nishikubo, K.; Xu, C., *Phys. Rev. B*, **2005**, *71*, 174404.
[10] Clissold, M. E.; Leverett, P.; Williams, P. A.; Hibbs, D. E.; Nickel, E. H. *Can. Mineral.* **2007**, *45*, 317.
[11] Shannon, R. D. *Acta Cryst. A* **1976**, *32*, 751.
[12] Chu, S.; McQueen, T. M.; Chisnell, R.; Freedman, D. E.; Müller, P.; Lee, Y. S.; Nocera, D. G. *J. Am. Chem. Soc.* **2010**, *132*, 5570.
[13] Colman, R. H.; Sinclair, A.; Wills, A. S. *Chem. Mater.* **2010**, *22*, 5774.
[14] Schluter, J.; Malcherek, T. *N. Jb. Miner. Abh.* **2007**, *184*, 39.
[15] Wang, J.; Toby, B. H.; Lee, P. L.; Ribaud, L.; Antao, S. M.; Kurtz, C.; Ramanathan, M.; Von Dreele, R. B.; Beno, M. A. *Rev. Sci. Instrum.*, **2008**, *79*, 085105.
[16] Janson, O.; Richter, J.; Rosner, H. *Phys. Rev. Lett.* **2008**, *101*, 106403.
[17] Janson, O.; Richter, J.; Rosner, H. *J. Phys. Conf. Ser.* **2008**, *145*, 012008.
[18] Rodriguez-Carvajal, J. *Physica B*, **1993**, *192*, 55.
[19] TOPAS (Version 4.1), program available from Bruker AXS, Östliche Reinbruckenstrasse 50, 76187 Karlsruhe, Germany.
[20] Colman, R.; Bert, F.; Boldrin, D.; Hillier, A.; Manuel, P.; Mendels, P.; Wills, A. *Phys. Rev. B* **2011**, *83*, 180416.
[21] Lee, S. H.; Kikuchi, H.; Qiu, Y.; Lake, B.; Huang, Q.; Habicht, K.; Kiefer, K. *Nature Mater.* **2007**, *6*, 853.
[22] Helton, J. S.; Matan, K.; Shores, M. P.; Nytko, E. A.; Bartlett, B. M.; Yoshida, Y.; Takano, Y.; Suslov, A.; Qiu, Y.; Chung, J. H.; Nocera, D. G.; Lee, Y. S. *Phys. Rev. Lett.* **2007**, *98*, 107204.
[23] Colman, R. H.; Ritter, C.; Wills, A. S. *Chem. Mater.* **2008**, *20*, 6897-6899.
[24] Obradors, X.; Labarta, A.; Isalgue, A.; Tejada, J.; Rodriguez, J.; Pernet, M., *State Commun.*, **1988**, *65*, 189.
[25] Wills, A. S.; Harrison, A., *J. Chem. Soc. Faraday. Trans.*, **1996**, *92*, 2161-2166.
[26] Wills, A. S.; Oakley, G. S.; Visser, D.; Frunzke, J.; Harrison, A.; Andersen, K.H., *Phys. Rev. B*, **2001**, *64*, 094436.
[27] Oakley, G. S.; Visser, D.; Frunzke, J.; Andersen, K.H.; Wills, A. S.; Harrison, A., *Physica B*, **1999**, *267*, 142-144.
[28] Ramirez, A. *Annu. Rev. Mater. Sci.* **1994**, *24*, 453.
[29] Kittel, C. *Introduction to solid state physics*, 7th ed.; John Wiley & Sons, Inc.: New York, USA, **2004**; pp. 417–422.
[30] de Vries, M.; Kamenev, K.; Kockelmann, W.; Sanchez-Benitez, J.; Harrison, A. *Phys. Rev. Lett.* **2008**, *100*, 157205.
[31] de Vries, M. A.; Stewart, J. R.; Deen, P. P.; Piatek, J. O.; Nilsen, G. J.; Ronnow, H. M.; Harrison, A. *Phys. Rev. Lett.* **2009**, *103*, 237201.
[32] Trombe, J.; De Vries, M.; Harrison, A.; Mendels, P. *Phys. Rev. Lett.* **2008**, 026405.
[33] Gaj, J. A.; Planel, R.; Fishman, G. *Solid State Commun.*, **1979**, *29*, 435.

[34] Olariu, A.; Mendels, P.; Bert, F.; Duc, F.; Trombe, J. C.; de Vries, M. A.; Harrison, A. *Phys. Rev. Lett.* **2008**, *100*, 087202.

[35] Chu, S.; McQueen, T. M.; Chisnell, R.; Freedman, D. E.; Muller, P.; Lee, Y.S.; Nocera, D.G. *J. Am. Chem. Soc.* **2010** *132*, 5570.

CHAPTER 4

Kapellasite, α-$ZnCu_3(OH)_6Cl_2$

As chemists we have a number of sources of inspiration to help guide our synthetic efforts. The most obvious being the body of literature and experiments described by previous generations of chemists. Less obvious is the inspiration that can be drawn from nature. Nature has for many hundreds of years been combining chemicals under a wide array of conditions and the fruits of these reactions are the variety of minerals found in the environments around and below us.

The databases produced through the study of these minerals can be an excellent starting point when searching for specific crystal structure properties. The localities and environments that these minerals were formed in can also provide inspiration for controlled synthesis in the laboratory.

This chapter details efforts to further increase the library of $S = \frac{1}{2}$ kagome antiferromagnets, namely the synthesis and magnetic characterise of the mineral kapellasite, α-$ZnCu_3(OH)_6Cl_2$, a crystallographic polymorph of the previously discussed γ-phase herbertsmithite,[**1, 2**] γ-$ZnCu_3(OH)_6Cl_2$.

4.1. Introduction

Figure 4.1a shows the crystal structure of kapellasite, a highly 2-dimensional brucite-like network of $Zn(OH)_6$ and $Cu(OH)_4Cl_2$ octahedra, weakly joined in the 3rd dimension through O–H–Cl hydrogen bonding (figure 4.1b). The metal ions reside on a triangular lattice, and effective segregation of the Jahn-Teller active Cu^{2+} ions to the tetragonally elongated $M(OH)_4Cl_2$ sites creates a sublattice of $S = \frac{1}{2}$ kagome ions with 3-fold rotation symmetry. Complete occupation of the triangular lattice by Cu^{2+} leads to a rearrangement of the Cl^-/OH^- groups and the mineral botallackite, α-$Cu_2(OH)_3Cl$, seen in figure 4.1c.

Considering the kagome planes, kapellasite has a shorter intra-planar Cu–Cu when compared to herbertsmithite, 3.17 Å *vs.* 3.42 Å respectively, and a larger interplanar

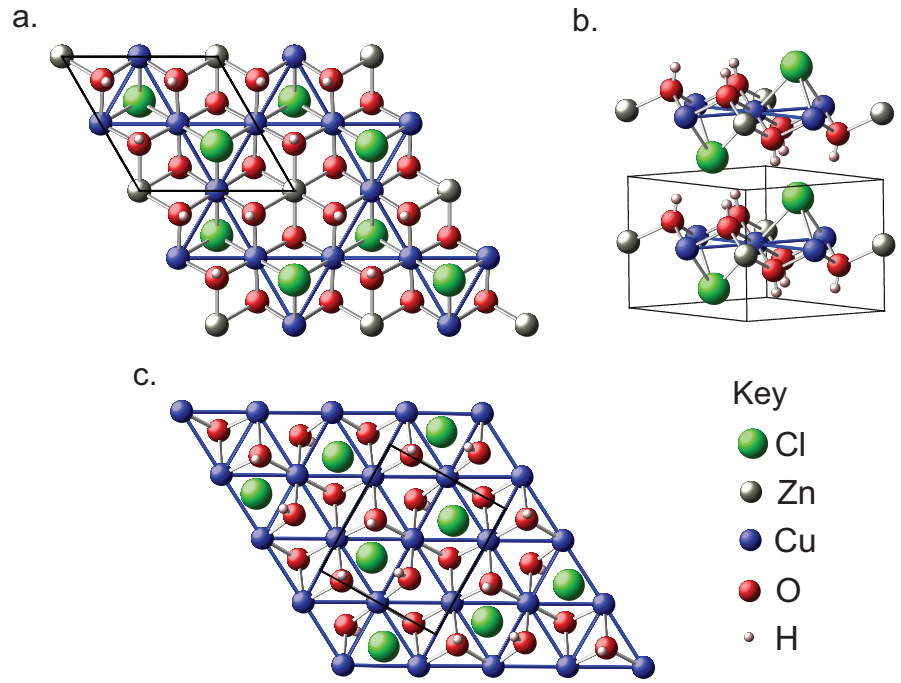

FIGURE 4.1. The crystal structure of: a. kapellasite, α-$ZnCu_3(OH)_6Cl_2$, with a kagome lattice of $S = \frac{1}{2}$ Cu^{2+} ions, created by the controlled diamagnetic doping of Zn^{2+} onto a triangular lattice; b. showing well separated planes of kapellasite; and c. botallackite, α-$Cu_2(OH)_3Cl$, fully occupied by Cu^{2+}, with triangular planes and a rearranged Cl^-/OH^- structure.

Cu–Cu distance of 5.68 Å *vs.* 5.08 Å.[**3**] These would naively suggest that kapellasite may have stronger in-plane exchange with a larger 2-dimensional character but superexchange pathways will also be sensitive to oxygen hybridisation and bond angles.

Like herbertsmithite, the lattice of kapellasite exhibits the possibility of Cu/Zn intersite exchange, but unlike herbertsmithite this exchange does not lead to the possibility of inter-layer exchange pathways, as the layers in kapellasite are linked only by hydrogen bonding. Instead, the exchange introduces local triangular defects that would themselves be expected to be frustrated. This leads to the expectation that kapellasite will be a better model kagome magnet in the search for quantum spin-liquid ground-states.

4.2. Synthesis

4.2.1. Natural inspiration

The environment in which a mineral has been naturally formed can give inspiration for controlled synthesis in a laboratory. Whilst kapellasite was originally identified as a sample from a copper mine in the Sounion region of Atacama, Chile,[**2**] it is consideration of the closely related mineral botallackite, also found in the Sounion mines, that provides the key to kapellasite's successful synthesis. Botallackite's type locality is a mine situated near Botallack, Cornwall, UK, stretching out far below the Atlantic seabed (figure 4.2a).[**4**] Botallackite is a secondary mineral, formed as halide-containing seawater percolates through the recently mined copper veins. As these aqueous solutions reach the atmosphere of the mine shafts and begin to evaporate, concentrating the liquor, botallackite is precipitated.[**5**] These copper-hydroxide based minerals are easily recognisable due to their bright blue/green colours. Figure 4.2b is a photo of secondary-copper-mineral deposits leaching down a Botallack cliff-side from a mine slag-heap. Botallackite is likely present near sea-level and results from inclusion of chlorides from the sea-water.

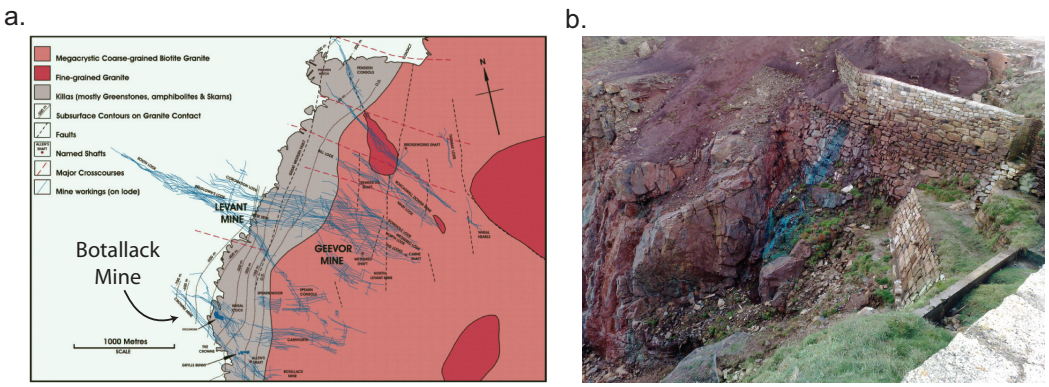

FIGURE 4.2. a. A schematic of the Levant mine, neighbouring the Botallack mine on the coast of Cornwall, UK, showing horizontal drifts stretching out far below the sea floor. Reproduced from [**5**] b. A photo of secondary copper mineral deposits on a Botallack cliff-face, with the likely presence of botallackite near sea-level upon inclusion of chlorides from the sea-water.

4.2.2. Literature inspiration

Whilst no literature exists detailing the successful synthesis of kapellasite, a considerable body of work on the synthesis and structural details of transition-metal hydroxy-halide phases were carried out by F. W. Ostwald and W. Feightnesh in the mid 20th century.[**11, 12, 13**] Included in these works are studies of the mixed-metal

hydroxy-halides of copper and zinc, resulting mostly in the synthesis of paratacamite and herbertsmithite phases, but with mention of an additional unstable phase reported with C6-symmetry and a 1:3 ratio of Cu:Zn.[**13**] Whilst no further structural characterisation was carried out, the reported X-ray diffraction peak positions match those of kapellasite, suggesting that this work could provide a good starting point for synthesis attempts.

4.2.3. Synthesis optimisation

The proposed synthesis reported by Ostwald and Feightnesh[**13**] suggests kapellasite can be formed by the slow bubbling of oxygen through an aqueous solution of 0.25 M zinc chloride and metallic copper powder at reflux for 24 hrs. The parallels between this reported synthesis and the formation environment of the botallackite mineralogical specimens are immediately apparent.

Attempts at this synthesis yielded green polycrystalline samples that were characterised by laboratory powder X-ray diffraction as phase-pure paratacamite. Luckily, unlike the hydrothermal synthesis of herbertsmithite in sealed steel vessels,[**1**] this reaction is performed in glassware allowing observation of the solution with time. Throughout the 24-hour reaction period, the solution and suspended product goes through several distinct colour changes, particularly over the first hour, an observation that prompted further investigation of the reaction profile.

Extracted portions of the precipitate at 5 minute intervals during the first hour of the reaction made it possible to identify the species evolution that gives rise to the distinct colour changes. The isolated precipitates showing the distinct colour changes are shown in figure 4.3a, together with a selection of collected X-ray diffraction patterns from the precipitates.

During the early stages of the reaction, the solution colour is dominated by the suspended red metallic copper powder. This red colour then gives way to a grey phase that was identified as the zinc-based mineral simonkolleite, $Zn_5(OH)_8Cl_2{\cdot}H_2O$. At $\sim$ 30 minutes this phase quickly disappears and the desired kapellasite product is formed. For the following 10 minutes kapellasite is found to be the only product present. However, upon leaving the reaction to continue a parasitic paratacamite phase develops. The paratacamite phase fraction grows with time at the expense of the kapellasite fraction and after $\sim$ 1.5 hours no kapellasite product is detectable by laboratory X-ray diffraction. Isolating the kapellasite must be done by hot filtration

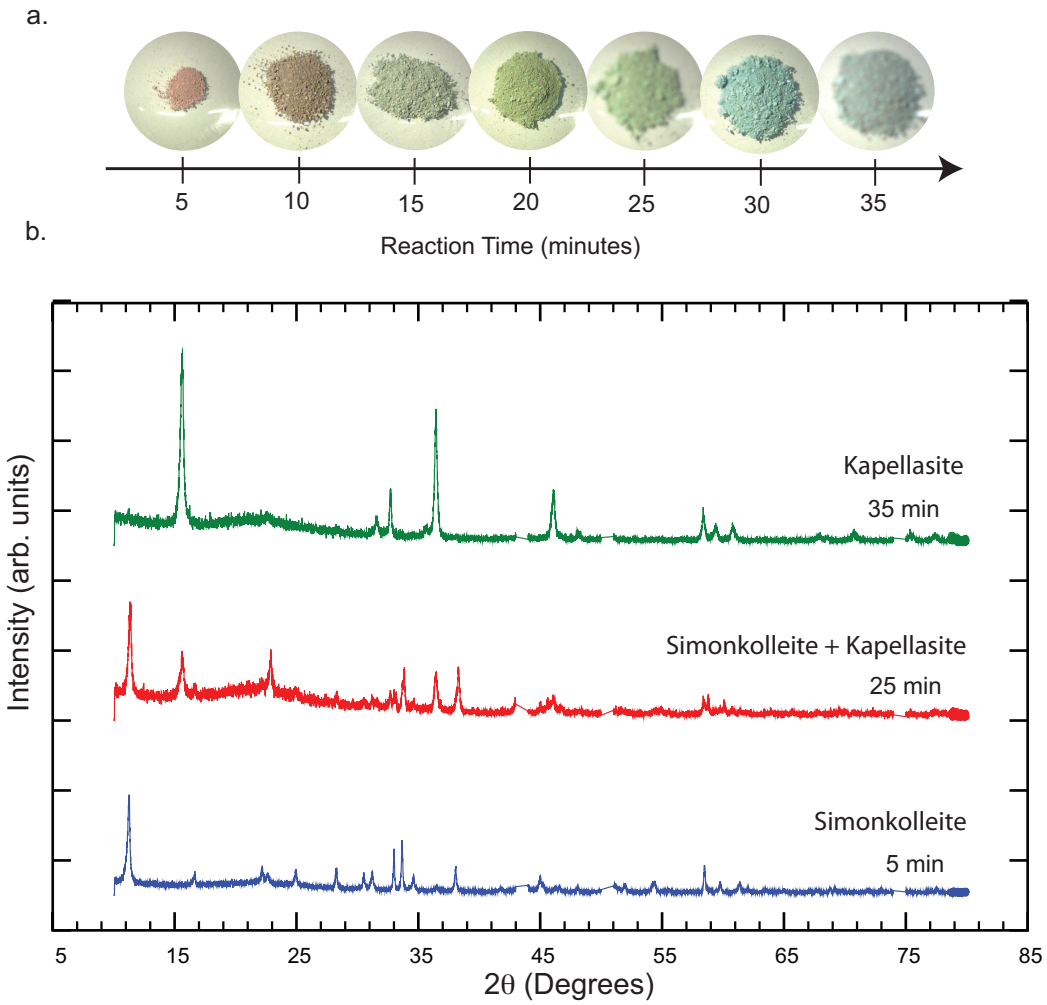

FIGURE 4.3. a. Left to right, the isolated reaction precipites during the synthesis of kapellasite. Extracted at 5 minute intervals. Left showing strong red colouration due to the presence of metallic copper, followed by the grey of the Zn-based mineral Simonkolleite and finally, right, the blue colouration of the desired kapellasite product. b. Selected diffraction patterns showing the formation of kapellasite over a 10 minute period, collected using a D8 diffractometer with λ = Cu K_α. Reactant copper peaks are excluded for clarity.

as cooling of the mother liquor was also found to lead to the precipitation of the paratacamite impurity phase.

This competitive behaviour between the two polymorphs indicates that kapellasite is the kinetic product under these reaction conditions, forming quickly over a short time period. Despite the initial formation of kapellasite, if the material is allowed to remain in the mother liquor the thermodynamically more stable product, herbertsmithite, is preferentially formed, consuming the kinetic product, kapellasite.

To further complicate the situation, this reaction is not found to be repeatable without an etched glass surface to nucleate kapellasite crystallite formation. The addition of ground glass beads to the reaction solution provided the surface required to allow the reaction to be repeatable in all glassware.

4.2.4. Optimised synthetic procedure

After extensive experimentation, the following synthetic procedure was found optimal for the repeatable synthesis of phase pure kapellasite.[**11, 12**] Copper powder (635 mg, 10 mmol) was refluxed in a 0.25 M aqueous solution of $ZnCl_2$ (100 ml) with 2×2 mm ground glass beads (as a nucleation surface) and slow oxygen bubbling. After 15 minutes a grey precipitiate (identified as simonkolleite) had formed and after 25 minutes this precipitate quickly turns blue. This blue precipitate was collected by hot filtration under vacuum and washed with distilled water (3×20 ml). A suspension of the collected product in distilled water (50 ml) was then sonicated (5 min) before allowing the unreacted metallic copper to settle to the bottom (5 min). The top 40 ml of suspension was then collected and the precipitate isolated from the suspension by centrifugation before drying under vacuum. The collected kapellasite (190 mg, 13 % yield) was found to be phase pure by laboratory X-ray diffraction. For the preparation of a deuterated sample, deuterium oxide (99.9 atom %) was used in place of water in all steps.

4.2.5. Scanning electron microscopy

In order to investigate the product crystallinity and crystallite morphology, samples of kapellasite were imaged using a Jeol JSM-6480LV scanning electron microscope (SEM), under high-vacuum and at room temperature. The crystallites were found to be extremely anisotropic in shape, growing as rough platelet (figure 4.4). The platelet cross-sections varied widely in the range $0.01 < r_{\text{platelet}} < 10$ μm, with thicknesses smaller than resolvable using the instrument (< 10 nm). This type of crystallite morphology is not surprising considering the highly 2-dimensional crystal structure. Strong bonding in the *ab* plane is likely to give rise to preferential crystallite growth in this dimension compared to the weakly hydrogen-bound *c* axis. Another strong influence on sample crystallinity is the rate at which these crystallites are formed. Following the time-dependence of the reaction by X-ray diffraction showed that the kapellasite product quickly precipitates over the course of a few minutes, giving rise to poorly defined crystallites. Despite this, the crystallite edges are often found to be $\sim 120°$, reflecting the trigonal nature of kapellasite's space-group, $P\bar{3}m1$.

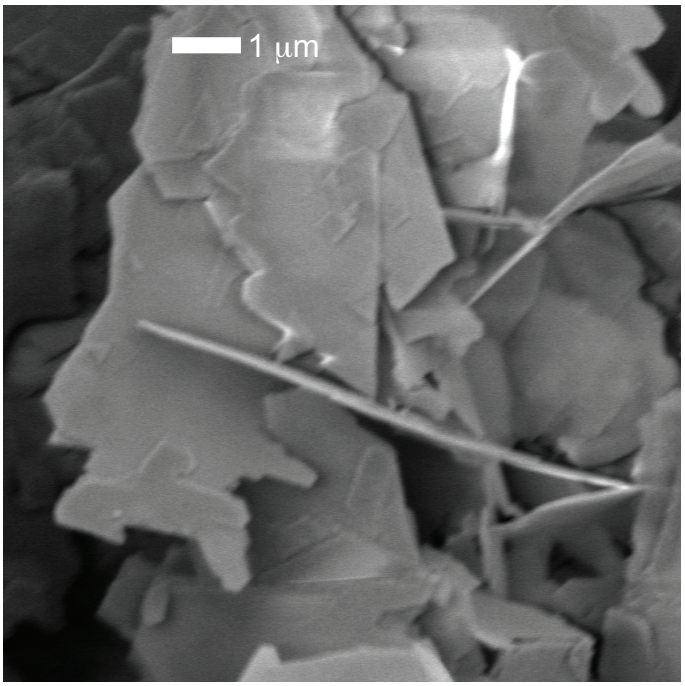

FIGURE 4.4. A representative SEM image of synthetic kapellasite, showing the strong 2-dimensional and rough character of the synthesised kapellasite crystallites.

4.3. Powder neutron diffraction

To investigate the nuclear and magnetic structure of the synthetic protonated and deuterated kapellasite samples diffraction patterns were collected using several powder neutron diffractometers. Throughout this section the different diffraction data collections will be discussed, leading on to Rietveld refined structures and a summary of the changes seen in magnetic scattering across the temperature ranges studied.

4.3.1. Protonated sample, D1a

In an attempt to characterise the structure of protonated kapellasite, a neutron diffraction pattern was collected using the high resolution powder neutron diffractometer D1A, ILL. The refined structural parameters of a protonated synthetic sample are of particular interest to mineralogists for comparison with natural specimens. A 1 g sample of kapellasite was loaded into a 4 mm vanadium sample can, and placed in the beam at room temperature, using neutrons with wavelength $\lambda = 1.909$ Å. The pattern, collected over 22 hrs shows a considerable background due to the large incoherent scattering cross-section of the protons present in the structure. Despite this

limitation, the well defined nuclear Bragg reflections allowed refinement of the nuclear structure. The refined pattern, obtained using the Rietveld refinement program FullProf,[**10**] can be seen in figure 4.5.

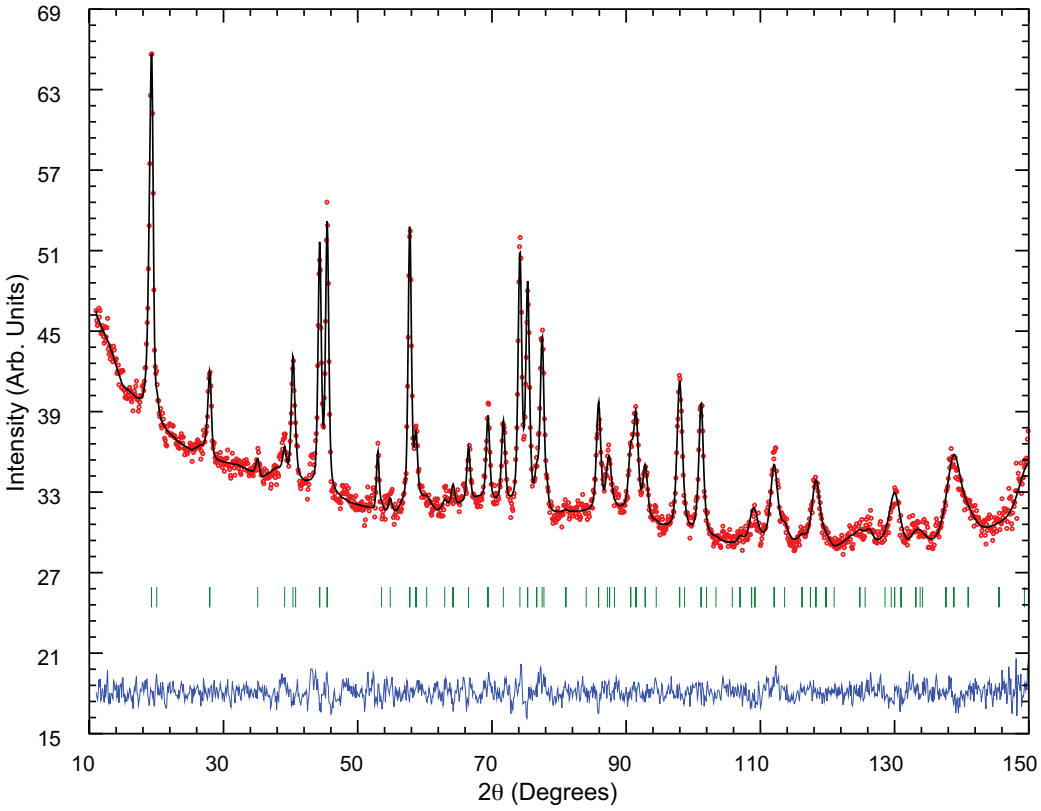

FIGURE 4.5. The neutron diffraction pattern and Rietveld refined structural fit to data collected on protonated kapellasite using the D1A diffractometer at room temperature and wavelength $\lambda = 1.909$ Å. The red marks are the data, black line the fit, blue line the residual difference and the tick marks show reflection positions. The final goodness-of-fit parameter $\chi^2 = 0.99$.

The refined structural parameters are shown in table 4.1. Whilst attempts were made to refine occupancies corresponding to site mixing between the nominally Cu^{2+} and Zn^{2+} positions, the refinement resulted in no unique solution and so site occupancies were left at unity. Of particular value from this refinement is the accurate determination of the proton position. Previous DFT calculations have shown this to be important in understanding the oxygen hybridisation and correspondingly the Cu–O(H)–Cu superexchange,[**8, 9**] but this has been limited due to difficulties found in the analysis of X-ray powder diffraction data.[**17**]

Our refinements show the Cu–O(H)–Cu bond angle in kapellasite is found to have a value of 105.1°, which is in the antiferromagnetic-ferromagnetic exchange crossover

TABLE 4.1. The refined crystallographic parameters for synthetic kapellasite, α-$Cu_3Zn(OH)_6Cl_2$ at room temperature, using data collected on D1A, ILL with neutrons of $\lambda = 1.909$ Å. The refined lattice parameters are $a = b = 6.33020(55)$Å, $c = 5.70167(59)$Å in the hexagonal setting of the space group $P\bar{3}m1$. The fractional occupancies of all sites were left at unity.

Wyckoff Site	Atom Name	x	y	z	U_{iso}
$3f$	Cu	$\frac{1}{2}$	0	$\frac{1}{2}$	0.026(3)
$1b$	Zn	0	0	$\frac{1}{2}$	0.010(4)
$2d$	Cl	$\frac{1}{3}$	$\frac{1}{6}$	0.1539(16)	0.031(3)
$6i$	O	0.3567(21)	0.1783(10)	0.3403(3)	0.031(3)
$6i$	H	0.3979(10)	0.1989(5)	0.185(3)	0.085(4)

range of 101–105° seen in in similar Cu–O(H)–Cu systems.[**18**] Because of this, care must be take when labelling this material as simply ferromagnetic or antiferromagnetic.

4.3.2. Deuterated sample - D2b

In order to reduce the background due to incoherent scattering from the protons, and to gain more detailed structural information, a deuterated sample was used for a temperature dependent study of the powder diffraction pattern. The incoming wavelength, $\lambda = 1.594$ Å, of the D2B diffractometer allows collection of refinable data to shorter d-spacings than available on D1A enabling more reliable refinement of thermal displacement parameters. Additionally the large-area 138-^{3}He tube-detectors provide high-resolution patterns for good quality structural refinements. In this case a 2 g sample was again loaded into a 6 mm vanadium can, before being inserted into a standard orange cryostat. Diffraction patterns were collected for 12 hrs each at 1.5, 10 and 35 K.

Rietveld refinements of the structure were performed for each pattern using the refinement program TOPAS, due to its greater flexibility in the definition of peak profile broadening terms.[**14**] When refining the peak profile, strong *hkl*-dependent anisotropic broadening was found. To successfully model this broadening the *hkl*-dependence of an additional Gaussian broadening term was refined using an 8th order spherical harmonic. This type of *hkl*-dependent broadening is indicative of anisotropic crystallites where poorer crystallinity in the weakly bound c axis, observed in the SEM images (figure 4.4), gives rise to increased broadening of *l*-dependent reflections. The refinement fit to the 1.5 K pattern can be seen in figure 4.6.

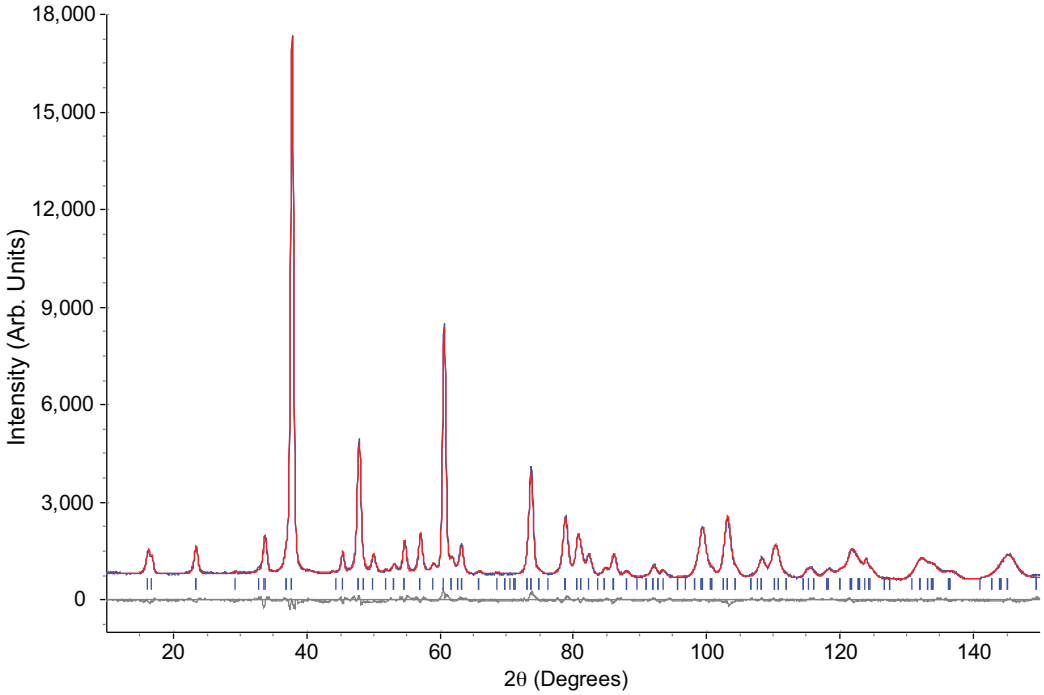

FIGURE 4.6. The neutron diffraction pattern and calculated pattern collected on deuterated kapellasite at 1.5 K using the D2B diffractometer with an incident neutron wavelength $\lambda = 1.594$ Å. The blue line is the data, red line the fit, lower grey line is the residual difference and tick marks show reflection positions. The final goodness-of-fit parameter is $\chi^2 = 3.067$.

No evidence was seen for the development of a magnetic Bragg contribution across this temperature range. The refined structural parameters can be seen in tables 4.2 and 4.3. The level of proton exchange was found to be minimal with the value refining to $> 93\%$. Using this high quality data and difference in neutron scattering lengths, 7.485 *vs.* 4.054 fm for Cu and Zn respectively, site occupancies could also be reliably refined. Substantial exchange between Cu^{2+} and Zn^{2+} on both sites was found: the kagome $3f$ site was occupied with 26.8(40) % Zn showing considerable diamagnetic dilution of the lattice; as well as the hexagonal $1b$ site containing 11.6(36) % Cu introducing localised triangular clusters across the lattice. The refined Cu/Zn ratio was therefore 1.37(12), a notable deviation from the idealised ratio of 3.

Comparisons between protonated and deuterated structures shows only minimal differences suggesting very similar magnetic behaviour can be expected.

TABLE 4.2. The refined crystallographic parameters for synthetic deuterated kapellasite, α-$Cu_3Zn(OD)_6Cl_2$ at 1.5 K, using data collected on D2B, ILL with incoming neutron wavelength $\lambda = 1.594$ Å. The refined lattice parameters are $a = b = 6.34677(13)$Å, $c = 5.68232(18)$Å in the hexagonal setting of the space group $P\bar{3}m1$.

Wyckoff Site	Atom Name	x	y	z	Occupation
$3f$	Cu/Zn	$\frac{1}{2}$	0	$\frac{1}{2}$	0.73(4)/0.27(4)
$1b$	Zn/Cu	0	0	$\frac{1}{2}$	0.88(2)/0.12(2)
$2d$	Cl	$\frac{1}{3}$	$\frac{1}{6}$	0.1467(6)	1
$6i$	O	0.3505(4)	0.1752(2)	0.3424(7)	1
$6i$	D/H	0.3829(3)	0.1914(2)	0.1685(9)	0.94(1)/0.06(1)

TABLE 4.3. The refined anisotropic thermal parameters for synthetic deuterated kapellasite.

Site	U_{11}	U_{22}	U_{33}	U_{12}	U_{13}	U_{23}
Cu/Zn	0.0054(9)	0.0041(13)	0.0084(15)	0.00205(7)	-0.0014(8)	-0.0014(8)
Zn/Cu	0.0055(16)	0.0055(16)	0.007(4)	0.0026(8)	0	0
Cl	0.0141(7)	0.0141(7)	0.0168(16)	0.0078(4)	0	0
O	0.0124(15)	0.0019(19)	0.026(2)	0.0000(10)	-0.0008(18)	0
D/H	0.0280(14)	0.0227(15)	0.0104(2)	0.0114(8)	-0.0039(14)	0

4.3.3. Deuterated sample - WISH

The deuterated sample was also investigated using the WISH diffractometer at ISIS to probe the temperature dependence of the magnetic scattering, searching for diffuse features that could evidence the build up of short-range correlations. Optimised for high-flux at long-wavelength the WISH diffractometer is an ideal instrument for observing changes in the magnetic scattering that fall off quickly with increasing Q (decreasing d-spacing). These measurements were performed prior to commissioning of the solid-methane moderator. This lead to below-optimal flux at long wavelength and was counteracted during the experiment by longer measurement times. The same 2 g sample of deuterated kapellasite was filled into a Cu sample can and loaded into a ^{3}He dilution refrigerator. Measurements taken whilst cooling the sample showed minimal change in scattering other than a small thermal contraction of the crystallographic unit cell. To maximise the chance of observing magnetic features, diffraction patterns were collected for 10 hrs each at 0.06 and 300 K. The collected data from the low-angle bank can be seen in figure 4.7.

The high temperature, high d-spacing (low-Q) scattering (red line of figure 4.7) shows an increase that is unlike the form factor expected for a simple paramagnet, which would be largely flat in this d-spacing range. This suggests that either significant

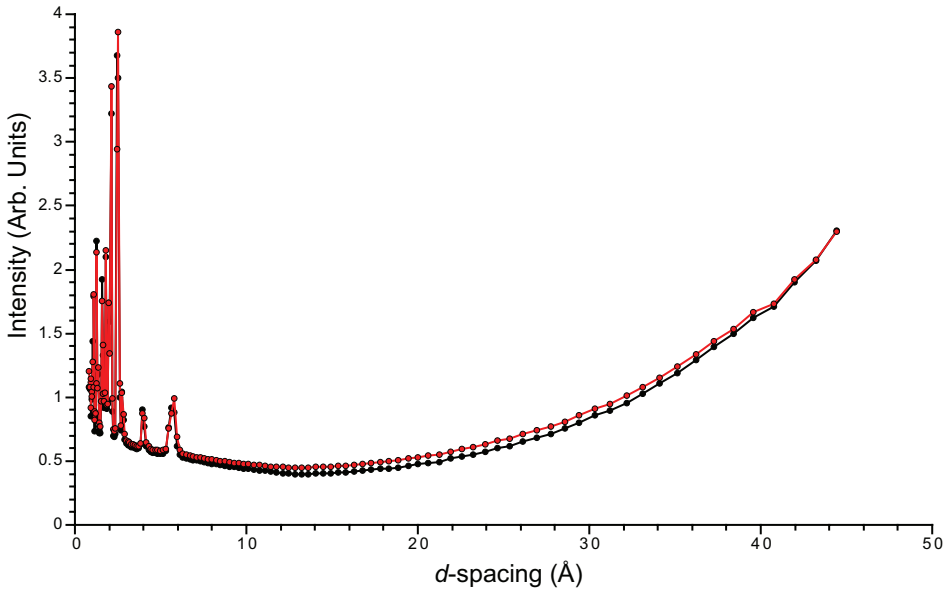

FIGURE 4.7. Neutron diffraction data collected on deuterated kapellasite at 300 (red) and 0.06 K (black).

correlations are present or that the magnetic scattering is on top of a sizeable instrumental background. Upon cooling, no evidence of a magnetic Bragg contribution to the pattern or the development of any broad features characteristic of the formation of short-range order were seen right down to 60 mK. There is, however, a small reduction in the scattering intensity in the $10 < d < 40$ Å range upon cooling that can be explained by a reduction in the magnetic component as observed by WISH. The *tof* inelastic neutron scattering data reported later in this chapter suggest that this change is a direct reflection of an evolution of the inelastic responses of kapellasite. Little more can be said with regards to diffraction data without the use of polarised neutrons to separate the magnetic contribution from the instrumental background.

4.4. DC-SQUID magnetometry

The temperature dependence of the magnetic properties were measured using a DC-SQUID magnetometer. A 50 mg sample of kapellasite was loaded into a gelatin capsule and centrally positionsed in a clear plastic drinking straw, fastened with a minimal amount of kapton tape. The straw was then inserted into the magnetometer using a brass-ended sample rod. The sample was then cooled, either in field (FC) or in zero-field (ZFC), before magnetisation measurements were made whilst warming from 2 to 300 K in a range of applied fields.

A characteristic plot of susceptibility, $\chi(T)$, can be seen in the inset of figure 4.8a showing a typical paramagnetic-like response with no evidence of a magnetic transition down to 2 K and no deviation between FC and ZFC data was seen. Figure 4.8a shows a plot of χ^{-1} *vs.* T. The high-temperature ($200 < T < 300$ K) linear region suggests paramagnetic-like behaviour that can be fitted with the Curie-Weiss law to give a Weiss temperature of $\theta_{\mathrm{W}} \sim -1.5$ K suggesting weak antiferromagnetic exchange, or a mean field that nearly cancels. Despite this low θ_{W} value, deviation from linearity at > 100 K in the plot of χ^{-1} *vs.* T is indicative of the build up of magnetic correlations, supporting the picture that there are strong exchange interactions in kapellasite that are of opposite sign and in a near state of balance.

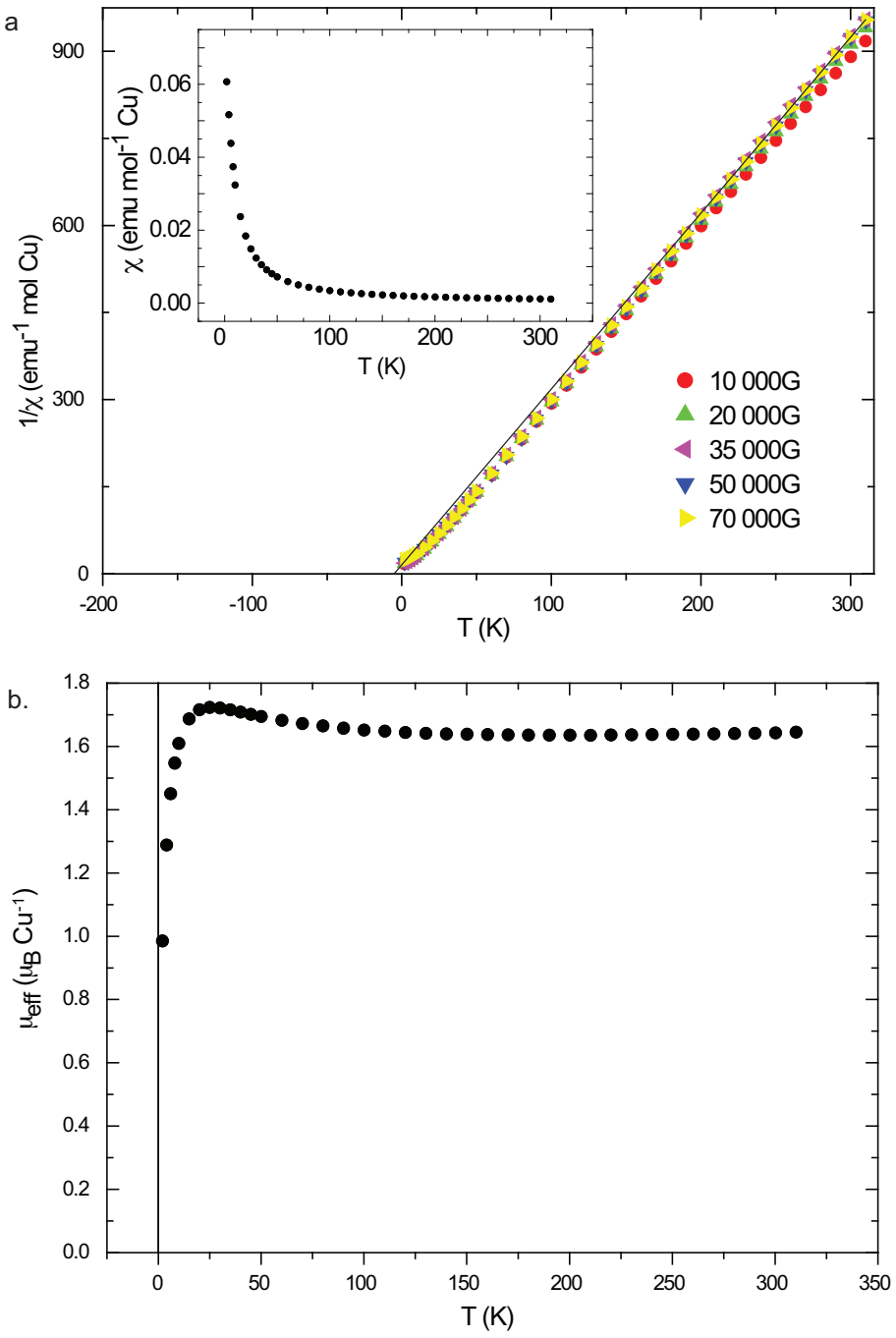

FIGURE 4.8. DC-SQUID magnetisation measurements performed on a 50 mg sample of kapellasite: a. χ^{-1} *vs.* T showing high-temperature linear Curie-Weiss behaviour and an extrapolated fit giving $\theta_W \sim -1.5$ K as well as slight deviations from linearity at ~ 100 K indicative of the build up of magnetic correlations. The inset shows χ *vs.* T with typical paramagnetic curvature and no sign of an ordering transition down to 2 K. b. μ_{eff}, versus T giving high temperature values in the range expected from the spin-only formula for a $S = \frac{1}{2}$ ion. Upon cooling to 30 K a broad hump is observed followed by a sudden reduction of the moment upon further cooling.

Whilst these two observations at first seem contradictory, they can be explained by consideration of further neighbour competing exchange interactions. The nearest-neighbour interaction could be of significant magnitude to cause deviation from Curie-Weiss linearity, whilst a *further neighbour* exchange mechanism of competing sign would reduce the mean-field experienced by the ions resulting in a correspondingly low θ_W. These data support an investigation of kapellasite by density functional theory calculations (DFT)[**8, 9**] that suggested that a cross-diagonal exchange (J_{d1} of figure 4.9) is present and of significant magnitude to perturb the system. Whilst the exact size of this perturbation in kapellasite appears larger than that proposed by DFT for kapellasite, it provides a physical mechanism for explaining these otherwise contradictory observations.

Figure 4.8b shows a plot of the effective moment, μ_{eff}, versus T. Where $\mu_{eff} \approx \sqrt{8\chi T}$ in the low-field, high-temperature limit. At high temperatures the value of $\sim 1.72\mu_B$ Cu^{-1} is in line with that expected for a $S = \frac{1}{2}$ ion using the *spin-only* formula. As the temperature is decreased below 100 K positive deviation is seen with a broad maximum at 30 K followed by a rapid collapse of μ_{eff}. This rapid collapse could be explained by two possible scenarios: a build-up of the antiferromagnetic correlations leading to a reduction in μ_{eff}, with the material condensing into some form of exotic liquid-like ground-state; or alternatively by the formation of singlet-dimers across the lattice as predicted for a resonating valence bond state.[**19**] These singlets would be magnetically invisible and so a corresponding reduction in μ_{eff} is expected.

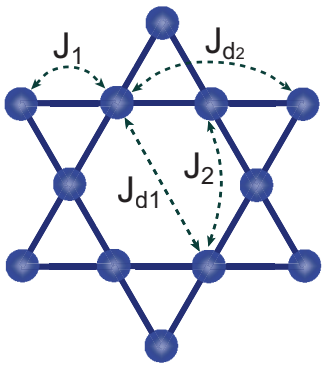

FIGURE 4.9. An illustration of the possible further neighbour exchange pathways within the kagome network.

4.5. Time-of-flight powder neutron spectroscopy

To further probe the nature of the exotic ground-state in this near-ideal $S = \frac{1}{2}$ kagome magnet, inelastic neutron scattering was performed on the previously described deuterated sample using the IN5 time-of-flight spectrometer at the ILL. A 3 g sample was loaded into an annular-geometry aluminium can before being inserted into a standard orange cryostat. Spectra were collected with an incident neutron wavelength $\lambda = 5$ Å , and at temperatures $T = 1.7$, 5, 12, 36, 100, and 300 K to examine the ω/Q landscape.

After subtractions of the elastic line (performed by Dr. B. Fåk), a broad liquid-like magnetic excitation is observed, centred at $Q \approx 0.5$ Å^{-1} (figure 4.10b). Unfortunately this excitation is partially masked by a spurious scattering feature from the sample environment.

Integration over energies $0.15 < \omega < 1.2$ meV (figure 4.10a) shows a temperature-dependent shift to higher Q of the excitation upon cooling. This shift indicates a change in the length-scale of the spins that are being excited by the inelastic neutron scattering process, and probably reflects a change in the balance of competing energy scales that is evidenced by the near zero value of θ_W in magnetisation measurements. Even at 300 K there is a significant inelastic magnetic contribution to the spectrum that would not be expected if the material was a simple paramagnet. This indicates the presence of magnetic correlations that are confirmed by the high temperature deviations from Curie-Weiss behaviour in this material. Upon cooling these liquid-like correlations become stronger and their signature in the inelastic neutron spectra increases in size. The peak is also seen to move away from the $Q = 0$ location on cooling, a change that would lead to a reduction in the magnetisation compatible with that seen by SQUID-magnetometry below ~ 30 K. This movement of inelastic responses away from $Q = 0$ could also be responsible for the reduction in the low angle magnetic scattering seen in the WISH data.

At 1.7 K the excitation centred at $Q = 0.5$ Å^{-1} corresponds to spins with a real-space separation of ~ 12.6 Å. This is significantly larger than the ~ 3.1 Å distance expected for a spin liquid based on nearest-neighbour antiferromagnetic correlations. This observation directly evidences the presence of significant further-neighbour exchange in the magnetic Hamiltonian of this exotic magnet.

No diffuse peak is evident in the WISH data at the scattering vector of this inelastic excitation. This is possibly because these responses reside outside the kinematic

window of the instrument, but it is more likely to be a consequence of a larger instrumental background on WISH when compared with the inelastic neutron spectrometer IN5.

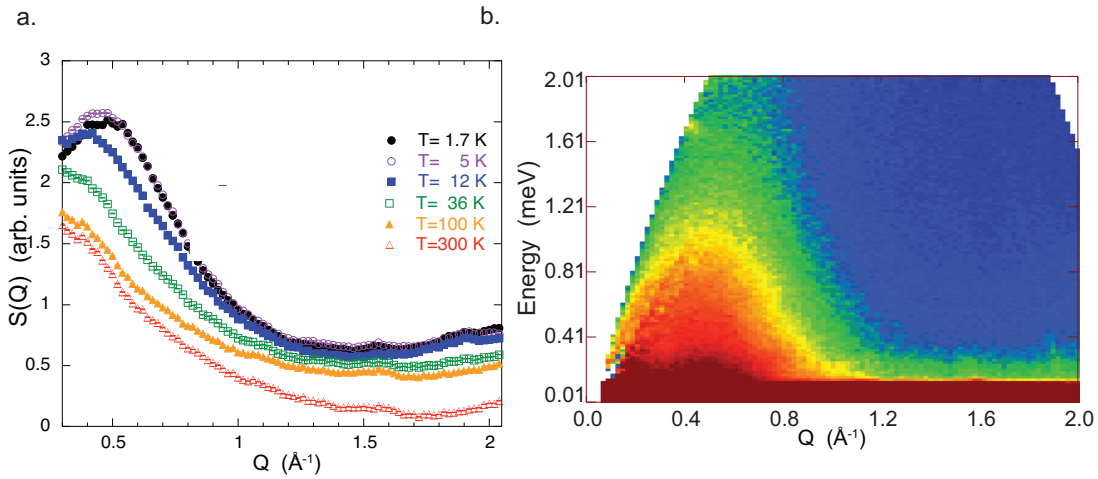

FIGURE 4.10. a. Q dependence of the magnetic scattering summed over energies $0.15 < \omega < 1.2$ meV using $\lambda = 5$ Å neutrons for several temperatures. A diffuse magnetic excitation is clearly present at $Q \approx 0.5$ Å^{-1} with decreasing intensity as the temperature is increased. b. $S(Q, \omega)$ plot at $T = 2$ K using neutrons at $\lambda = 5$ Å showing a magnetic excitation at $Q = 0.4$ Å^{-1}. The excitation has a broad, liquid-like character and appears gapless. Produced using LAMP.[**20**]

4.6. Discussion

The magnetisation measurements show a strong competition between terms in the Hamiltonian leading to a small mean-exchange field, yet deviation is seen from linear Curie-Weiss behaviour at much higher temperatures indicating that these competing terms, although cancelling, are strong. The strength of these interactions is further confirmed by a magnetic contribution to the inelastic spectrum at 300 K, showing that thermal fluctuations have not yet overpowered the correlations. The Q-dependence of the inelastic scattering indicates clearly that the further-neighbour interactions are important in defining the QSL in kapellasite, a phase that appears qualitatively different to that observed in herbertsmithite or the other known QSLs.

4.7. Conclusions

The synthesis and preliminary magnetic characterisation of a new $S = \frac{1}{2}$ kagome magnet, kapellasite has been presented. Kapellasite is found to be a good structural

approximation to a $S = \frac{1}{2}$ kagome, but cannot be considered an ideal model due to appreciably more Zn present in the structure than the ideal case, as well as anti-site disorder between Cu and Zn.

Neutron scattering experiments indicate that strong magnetic interactions are present over the range $1.7 - 300$ K. The inelastic responses and the magnetisation measurements are in agreement with the absence of a magnetic ordering transition down to 2 K. These two types of data also show clearly the presence of significant further-neighbour interactions within the magnetic Hamiltonian of kapellasite. Kapellasite, therefore, provides a unique opportunity to study an entirely new class of QSL within a kagome magnet, driven by competing nearest-neighbour and further-neighbour exchange interactions.

4.8. Future work

To fully understand the exchange Hamiltonian of this complex magnet, inelastic neutron diffraction experiments collected from single crystals will be needed. The difficulties in producing phase-pure powder samples suggests that without a significant synthetic breakthrough this is unlikely.

Measurements to probe the local susceptibility by muon spin relaxation and nuclear magnetic resonance measurements, performed by Prof. P. Mendels and Dr. F. Bert, are currently under analysis. By using these local probe techniques, impurity contributions to the susceptibility can be distinguished from the intrinsic kagome susceptibility.

Further experiments analysing the liquid-like ground-state by inelastic and spin-polarised neutron techniques are currently underway. Using spin-polarised measurements, the magnetic scattering can be fully decoupled from nuclear and background components, making analysis of the liquid-like feature much easier. With cleaner data confident extraction of the liquid-like correlation lengths can be performed.

References

[1] Shores, M. P.; Nytko, E. A.; Bartlett, B. M.; Nocera, D. G. *J. Am. Chem. Soc.* **2005**, *127*, 13462.

[2] Krause, W.; Bernhardt, H-J.; Braithwaite, R. S. W.; Kolitsch, U.; Pritchard, R. *Miner. Mag.* **2006**, *70*, 329.

[3] Lee, S. H.; Kikuchi, H.; Qiu, Y.; Lake, B.; Huang, Q.; Habicht, K.; Kiefer, K. *Nature Mater.* **2007**, *6*, 853.
[4] Frondel, C. *Miner. Mag.* **1950**, *29*, 34.
[5] LeBoutillier, N. D. *Ph.D. thesis*, **2002**, *University of Exeter, England.*
[6] Feitknecht, W.; Maget, K. *Helv. Chim. Acta* **1949**, *218*, 1639.
[7] Ostwald, H. R.; Feitknecht, W. *Helv. Chim. Acta* **1964**, *47*, 273.
[8] Feitknecht, W.; Maget, K. *Helv. Chim. Acta* **1949**, *219*, 1653.
[9] Shannon, R. D. *Acta Crystallogr.* **1976**, *A32*, 751.
[10] Braithwaite, R. S. W.; Mereiter, K.; Paar, W. H.; Clark, A. M. *Miner. Mag.* **2004**, *68*, 527.
[11] Colman, R. H.; Ritter, C.; Wills, A. S. *Chem. Mater.* **2008**, *20*, 6897.
[12] Colman, R. H.; Sinclair, A.; Wills, A. S. *Chem. Mater.* **2010**, *22*, 5774.
[13] Rodriguez-Carvajal, J. *Physica B*, **1993**, *192*, 55.
[14] Janson, O.; Richter, J.; Rosner, H. *Phys. Rev. Lett.* **2008**, *101*, 106403.
[15] Janson, O.; Richter, J.; Rosner, H. *J. Phys. Conf. Ser.* **2008**, *145*, 012008.
[16] TOPAS (Version 4.1), program available from Bruker AXS, Östliche Reinbruckenstrasse 50, 76187 Karlsruhe, Germany.
[17] Malcherek, T.; Schluter, J. *Acta Crystall. B-Stru.* **2007**, *63*, 157.
[18] Hastings, M. B. *Phys. Rev. B* **2001**, *63*, 014413.
[19] Anderson, P. W. *Mat. Res. Bull.*, **1973**, *8*, 153.
[20] Richard, D.; Ferrand, D.;Kearley, G. J. *J. Neutron Research*, **1996**, *4*, 33.

CHAPTER 5

Haydeeite, α-$MgCu_3(OH)_6Cl_2$

This chapter presents the synthesis, structural characterisation and magnetic properties of a diamagnetic analogue of kapellasite, the $S = \frac{1}{2}$ kagome magnet haydeeite α-$MgCu_3(OH)_6Cl_2$.[**1, 2**] Despite the two minerals being isostructural and isomagnetic,[**3**] they display markedly different magnetic ground-states. Upon cooling below 6 K haydeeite goes through a magnetic transition to a ground-state with spin glass-like character. At the same time strong quantum-fluctuations are evidenced by a reduced saturation moment.

5.1. Introduction

As chemists we have a number of tools to help us broaden the library of quantum-spin-liquid candidate materials. Chemical substitution is particularly important as it allows controllable and predictable changes to be made whilst retaining a structural motif. Both the herbertsmithite and paratacamite lattices have been shown suited towards the substitution of the diamagnetic Zn^{2+} ions for Mg^{2+} a property related to their similar charge and ionic radii (0.74 Å *vs.* 0.73 Å respectively). [**4, 5, 6**] This chemical *trick* can also be applied to the kapellasite structure, as evidenced by the recent mineralogical discovery of the Mg-subtituted analogue of kapellasite: haydeeite, α-$MgCu_3(OH)_6Cl_2$.[**1**].

Haydeeite shares the highly 2-dimensional structure of kapellasite. The kagome lattice is created by one quarter diamagnetic dilution of a triangular lattice of metal sites (figure 5.1a). The effective segregation is achieved by the preference for the Jahn-Teller active Cu^{2+} to reside on the tetragonally elongated MO_4Cl_2 sites while the non-Jahn-Teller active, and diamagnetic, Mg^{2+} prefers the more spherically symmetric MO_6 sites. The 2-dimensional magnetism is a result of the contrast between the strongly bound corner-sharing octahedral network of metal ions in the *ab* plane and the weak binding of the Brucite-like sheets by O–H$\cdots$Cl hydrogen bonding in the *c* axis (figure 5.1b). With shorter intra-planar and longer inter-planar Cu–Cu distances than its more widely studied sister-mineral herbertsmithite (3.15 Å and 5.73 Å

vs. 3.42 Å and 5.08 Å respectively)[**7**] haydeeite is an excellent model material for the study of 2-dimensional kagome physics.

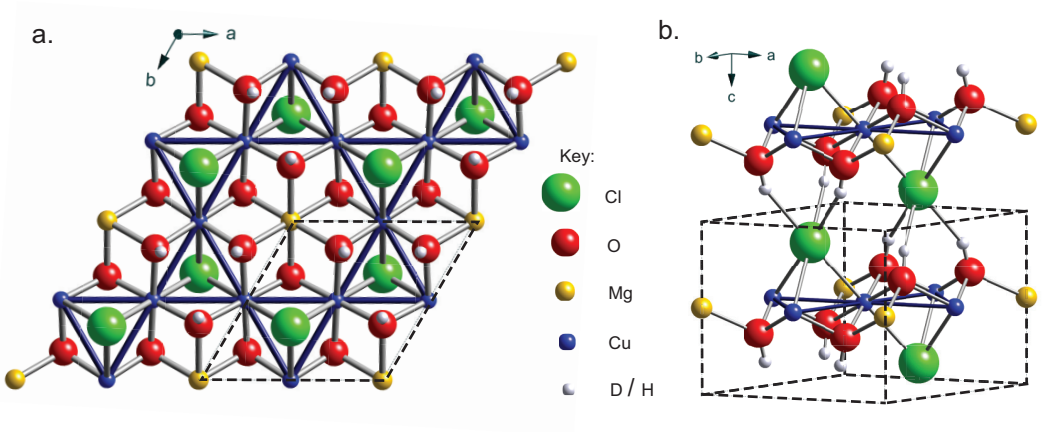

FIGURE 5.1. a. The crystal structure of haydeeite, α-$MgCu_3(OH)_6Cl_2$, with a kagome lattice of $S = \frac{1}{2}$ Cu^{2+} ions, created by the preferential diamagnetic doping of Mg^{2+} onto a triangular lattice; b. showing the well separated planes of haydeeite, with weak inter-layer O–H···Cl hydrogen bonding.

Whilst crystallographically Mg-containing haydeeite and Zn-containing kapellasite are isostructural, recent density functional theory calculations (DFT) have shown that the subtle electronic changes brought about in this substitution may have strong effects on the magnetic ground-states of these two exotic magnets.[**8, 9**] Further-neighbour exchange mediated by the diamagnetic ion is predicted to be notably larger in the Mg-substituted analogue. If strong enough, this additional exchange will destabilise the quantum spin liquid state and select a single, ordered magnetic ground-state. From an experimental perspective, the structure of any resultant ordered-state is important information as it can be used to gain insight into the nature of the correlations in the spin-liquid state from which it was formed.

This chapter highlights the subtle structural differences between haydeeite and kapellasite and preliminary magnetic characterisation of haydeeite using DC-SQUID magnetometry is presented. Distinct differences in magnetic ground-states between these two materials are clearly seen, supporting suggestions from recent DFT calculations.[**8**]

5.2. Synthesis

When considering the synthesis of haydeeite, lessons learnt from the previously discussed synthesis of both 'Mg-herbertsmithite' and kapellasite can be applied.[**10, 5**]

The early work on the mixed-transition metal hydroxy-halide phases by F. W. Ostwald and W. Feightnesh do not report the formation of haydeeite-like products. This is likely to be because their investigations did not use high enough concentrations of $MgCl_2$ solution.[**11, 12, 13**] As found in the synthesis of 'Mg-herbertsmithite', concentrations of Mg^{2+} ions are required to be considerably higher than those of Zn^{2+} for the formation of its isostructural analogue herbertsmithite. With this in mind, an identical experimental set-up to that of kapellasite was used, with the higher $MgCl_2$ concentrations (3.5 M compared to 0.25 M in the synthesis of kapellasite). Under these conditions, haydeeite was repeatably produced.

As with the synthesis of kapellasite, allowing the solution to cool leads to the formation of Mg-paratacamite impurities, yet unlike kapellasite the reaction did not occur over such a short time scale. The formation of haydeeite is extremely slow in comparison, with reasonable yields only being achieved after refluxing for several days.

5.2.1. Optimised synthesis

Copper powder (635 mg, 10 mmol) was refluxed in a 3.5 M aqueous solution of $MgCl_2$ (100 ml) for four days with ground glass beads (4×2 mm diameter) and slow oxygen bubbling. The blue precipitate (haydeeite) was then collected by hot filtration under vacuum and washed with distilled water (3×20 ml). A suspension of the collected product in distilled water (50 ml) was sonicated (5 min) before allowing the unreacted copper to settle to the bottom (5 min). The top 40 ml of suspension was then collected and the precipitate was isolated from suspension by centrifugation before drying under vacuum. The collected haydeeite (194 mg, 5% yield) was found to be phase pure by X-ray diffraction. For the preparation of a deuterated sample, deuterium oxide (99.9 atom%) was used in place of water in all steps.

5.3. DC SQUID magnetometry

In an effort to explore the magnetic properties of the synthesised haydeeite, magnetisation measurements were performed using a DC-SQUID magnetometer. A $\sim$ 100 mg sample of haydeeite was packed in a gelatin capsule, loaded into a clear plastic straw and inserted into the magnetometer. The magnetisation of the sample was measured as a function of both field and temperature.

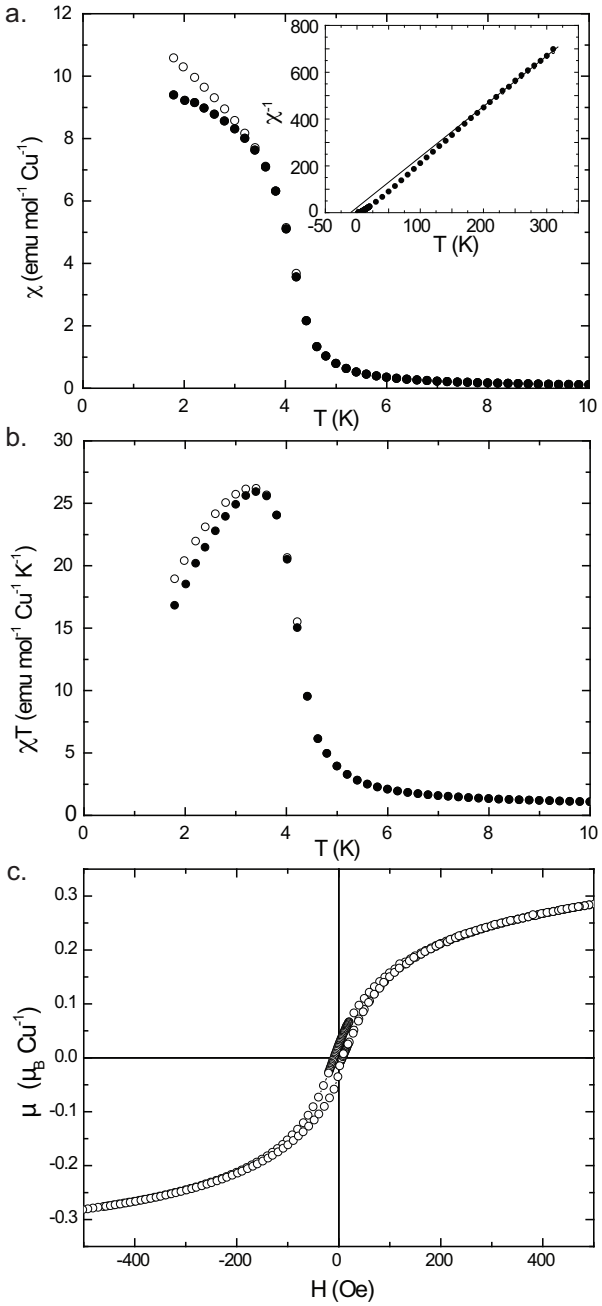

FIGURE 5.2. a. dc-susceptibility, χ, of haydeeite at low temperature, with the temperature dependence of χ^{-1} shown in the inset (calculated assuming an idealised formula). A Curie-Weiss fit to the high temperature region (300-–200 K) gives a Weiss temperature $\theta_{\mathrm{W}} \approx -1.5$ K; the full circles (•) represent the zero-field-cooled data, open circles (◦) represent the field-cooled data. A magnetic transition is seen upon cooling below 6 K, with the maximum in the derivative, $d\chi/dT$, at 4.2 K. b. The temperature dependence of χT shows a downturn below 3 K that is not characteristic of simple ferromagnetic ordering. c. The field dependence of the moment, μ, at 3 K evidences a small hysteresis associated with the transition and an extremely small spontaneous moment of 0.02 μ_{B} Cu^{-1}.

A plot of χ^{-1} *vs.* T, seen in the inset of figure 5.2a, shows a linear high-temperature region that can be fitted to the Curie-Weiss Law to give a Weiss temperature, $\theta_W \sim -1.5$ K. This is comparable to that of its isostructural analogue kapellasite with deviation from linearity in the same ~ 100 K region. From the fitted Curie constant, $C = 0.445(8)$ emu mol^{-1} Cu, the effective moment is calculated to be $\mu_{\text{eff}} = 1.89$ μ_B Cu^{-1}, at the lower end of, but in agreement with, related Cu^{2+} systems.[**15, 16, 17**]

In contrast to kapellasite, data from haydeeite shows a sharp increase in χ, coupled with divergence between field-cooled and zero-field-cooled measurements upon cooling below 6 K. This indicates that these closely related materials have a distinctly different magnetic ground-state (figure 5.2a). In haydeeite this response can be explained by either a ferromagnetic ordering transition, or a spin glass-like freezing. A plot of χT *vs.* T (figure 5.2b) shows a reduction of the moment upon cooling below this transition, an effect that would not be expected for a simple ferromagnetic ordering, making a spin-glass transition the more likely scenario. This hypothesis is further strengthened by the recent report of a frequency dependence in χ' from ac-susceptibility measurements.[**20**]

The weak hysteresis is more clearly seen in a plot of μ *vs.* H at 3 K (figure 5.2c). An extremely small spontaneous moment of 0.02 μ_B Cu^{-1} (calculated using the idealised formula) is seen at 3 K. Additionally, the observed saturation moment of $\sim 0.35\mu_B$ Cu^{-1} is considerably lower than the theoretical value of 1 μ_B atom^{-1} for a typical $S = \frac{1}{2}$ system. This indicates that a a strong perturbation is present within the spin glass-like phase that acts to reduce the saturation moment, such as quantum fluctuations.[**21**]

5.4. Powder neutron diffraction

To fully characterise the structure of haydeeite, and attempt to study any observable changes in magnetic scattering across the magnetic transition, temperature-dependent powder neutron diffraction patterns were collected using the high-resolution diffractometer D2B, ILL, from a deuterated sample.

The chosen incoming wavelength was $\lambda = 1.594$ Å, and due to sample-limited broadening the *high-flux, low-resolution* detector integration routines were used. In this case a 1 g sample was loaded into a 6 mm vanadium can, before being inserted into a standard orange cryostat. Diffraction patterns were collected for 12 hrs each at 1.5, 6 and 35 K.

Rietveld refinements of the structure were performed for each pattern using the refinement program TOPAS.[**14**] When refining the peak profile, an *hkl*-dependent anisotropic broadening was found, but not as pronounced as that seen in the kapellasite diffraction patterns. To successfully model this broadening the *hkl*-dependence of an additional Gaussian broadening term was refined using an 8th order spherical harmonic. This type of *hkl*-dependent broadening is indicative of anisotropic crystallites, where due to the stronger bonding in the *ab* plane of this highly 2-dimensional material preferential crystal growth occurs. Both the *hkl*-dependence and sample broadening as a whole were considerably less than that seen in the kapellasite samples. This is not surprising when considering the reaction timings: kapellasite is formed over a $\sim$ 10 minute period; whilst haydeeite crystallites grow over several days, leading to higher crystallite quality. The refinement fit to the 1.5 K pattern can be seen in figure 5.3a.

5.4.1. Structural refinement

The refined structural parameters can be seen in tables 5.1 and 5.2. These show only minimal differences with the refined parameters of kapellasite.[**10**] A small contraction of the *ab*-plane is seen from 6.34677(13) Å in kapellasite to 6.28853(11) Å in haydeeite, whilst Mg substitution causes an expansion of the *c* axis from 5.68232(18) Å to 5.72711(14) Å. Only small differences are seen in refined bond lengths and angles, with a full table of chemically significant parameters presented in appendix 2. Of particular note are those important to superexchange such as the Cu–O–Cu bond lengths and angles (2.0075(19) Å and 104.45(15)° for kapellasite, 1.9866(16) Å and 104.64(13)° for haydeeite). These appear too close to suggest that they feature different exchange strengths. DFT calculations have focused on the O–H/D bond length in these materials, and indicated that this can play a crucial role in superexchange.[**9**] Unfortunately, the proton position in this class of material is commonly mis-assigned using X-ray diffraction techniques, and so these neutron diffraction pattern refinements are particularly valuable in clarifying its determination.[**18**] Again little difference is seen between deuterated kapellasite and haydeeite O–D bond lengths with 0.9987(65) Å and 0.9838(53) Å, respectively. This suggests a similar hybridisation of the superexchange oxygen, and as such a similar exchange strength.

Refinement of the level of proton/deuterium exchange indicates that the quality of deuteration is good (> 96% D). Using these data and the difference in neutron scattering lengths, 7.485 *vs.* 3.631 fm for Cu and Mg respectively, allows reliable refinement of the metal site occupancies. Like kapellasite, the refinement found

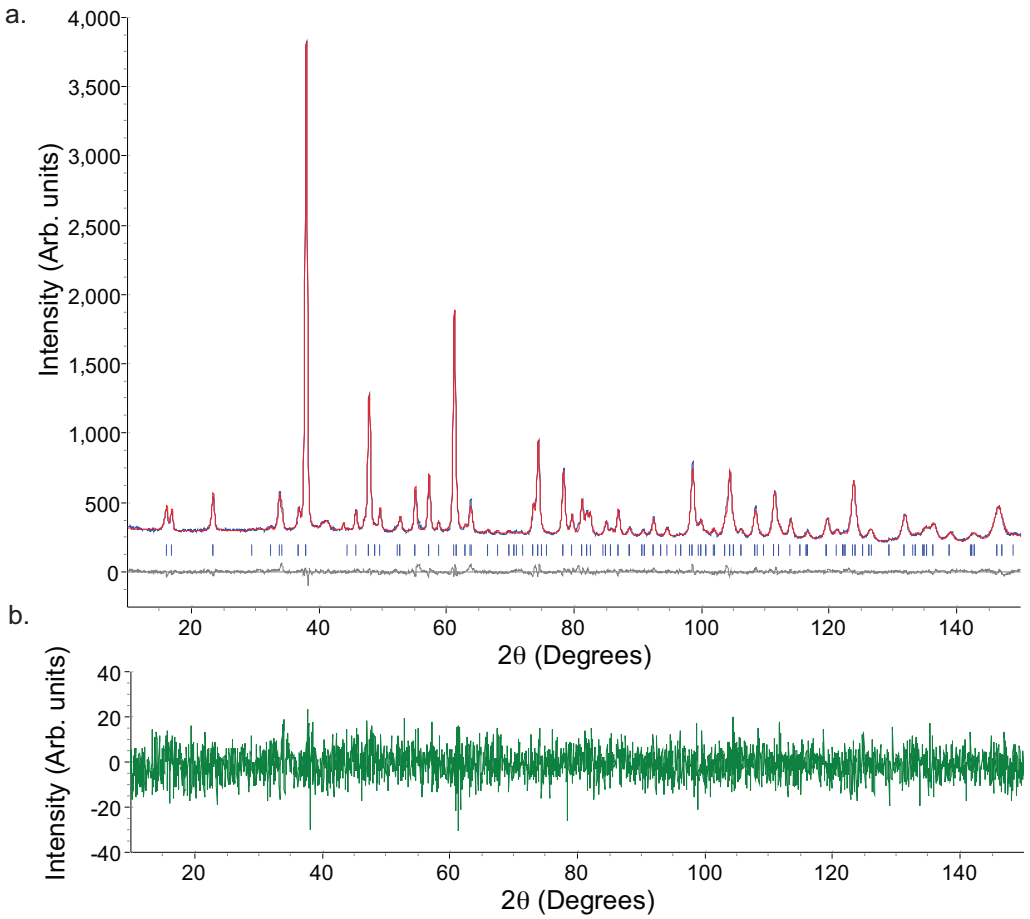

FIGURE 5.3. a. The neutron diffraction pattern and Rietveld refined structural fit to data collected on deuterated haydeeite at 1.5 K using the D2B diffractometer with an incident neutron wavelength $\lambda = 1.594$ Å. The blue line is the data, red line the fit, lower grey line is the residual difference and tick marks show reflection positions. The final goodness-of-fit parameter $\chi^2 = 3.405$. b. The low minus high temperature difference curve (1.5 – 6 K) showing no evidence of magnetic Bragg diffraction despite the apparent magnetic transition seen in the susceptibility data.

there to be substantial dilution by Mg on the kagome $3f$ site (16.4(43) % Mg). The hexagonal $1b$ site reliably refined to 0 % Cu occupation, corresponding to complete Mg occupation. These values lead to a total Cu/Mg ratio of 1.68(1), a notable deviation from the idealised ratio of 3, yet closer than that of kapellasite (Cu / Zn = 1.37(12)). This difference may be caused by the slower crystallisation rate of the haydeeite, leading to a product closer to the thermodynamic limit of complete site segregation.

To confirm these refined occupancies bond-valence calculations of the metal sites were attempted, using the program VaList.[**19**] These gave no additional information due to similarities between Cu–O and Mg–O bond valence parameters. As an alternative

TABLE 5.1. The refined crystallographic parameters for synthetic deuterated haydeeite, α-$Cu_{4-x}Mg_x(OD)_6Cl_2$ at 1.5 K, using data collected on D2B, ILL with incoming neutron wavelength λ = 1.594 Å. The refined lattice parameters are $a = b = 6.28853(11)$Å, $c = 5.72711(14)$Å in the hexagonal setting of the space group P$\bar{3}m1$.

Wyckoff Site	Atom(s)	x	y	z	Occupation
$3f$	Cu/Mg	$\frac{1}{2}$	0	$\frac{1}{2}$	0.84(4)/0.16(4)
$1b$	Mg	0	0	$\frac{1}{2}$	1.00(4)
$2d$	Cl	$\frac{1}{3}$	$\frac{1}{6}$	0.1400(6)	1
$6i$	O	0.3504(4)	0.1752(2)	0.3420(5)	1
$6i$	D/H	0.3907(4)	0.1953(2)	0.1749(7)	0.962(8)/0.038(8)

TABLE 5.2. The refined anisotropic thermal parameters for synthetic deuterated haydeeite.

Site	U_{11}	U_{22}	U_{33}	U_{12}	U_{13}	U_{23}
Cu/Mg	0.001(1)	0.0027(14)	0.0073(17)	0.0014(7)	-0.0013(10)	-0.0013(10)
Mg/Zn	0.017(2)	0.017(2)	0.001(5)	0.008(1)	0	0
Cl	0.0083(9)	0.0083(9)	0.019(9)	0.0042(5)	0	0
O	0.0056(14)	0.001(2)	0.0136(18)	0.0005(1)	0.0039(13)	0
D	0.0264(16)	0.0232(19)	0.001(16)	0.0116(10)	0.0052(15)	0

approach, comparisons between the bond distances and octahedral Jahn-Teller distortion ratio (defined as M–Cl/M–O) for the two metal sites, were considered for all of the materials in this family (table 5.3). With increasing occupation of a site by Jahn-Teller active Cu^{2+} ions, an increased distortion ratio is expected. Whilst the average bond distance, <M–O(Cl)>, for the kagome sites does not vary significantly across the compounds, a difference in the Jahn-Teller distortion ratio M–Cl/M–O is clearly seen. Importantly, this ratio is found to be largest in the herbertsmithites where the highest occupations of Jahn-Teller-active Cu^{2+} is found on the kagome site. Haydeeite is next largest, with kapellasite showing the least distortion. This confirms the trend of increasing diamagnetic dilution of the kagome lattice across the series kapellasite<haydeeite<'Mg-herbertsmithite'<herbertsmithite, as found by X-ray and neutron diffraction refinements. Whilst there is also an increase in the M–O bond distance of the *non-kagome* hexagonal site across this series, the point-group symmetry does not allow a distortion away from a trigonally-distorted anti-prism shape, thereby preventing a Jahn-Teller distortion from being accomodated on this site.

TABLE 5.3. Distortion parameters

Wyckoff Site	Bond	herbertsmithite [**7**]	'Mg-herbertsmithite' [**5**]	kapellasite [**10**]	haydeeite [**2**]
$9d/3f$	M–Cl	2.763 Å	2.765 Å	2.703 Å	2.747 Å
	M–O	1.985 Å	1.988 Å	2.006 Å	1.987 Å
	<M–O(Cl)>	2.24 Å	2.25 Å	2.23 Å	2.24 Å
	M–Cl/M–O	1.392	1.391	1.347	1.382
$3a/1b$	M–O	2.109 Å	2.100 Å	2.118 Å	2.114 Å

5.4.2. Magnetic scattering

Despite evidence of a magnetic transition, discussed in section 5.3, no development of magnetic Bragg peaks was seen across this temperature range. A plot of the 1.5 – 6 K difference curve (figure 5.3b) shows only a minor thermal lattice contraction in the nuclear peaks and no significant change in background scattering. Simple ferromagnetic trial models (along each crystallographic axis), manually adjusted until they can no longer be accommodated by the data, lead to a maximum ordered moment of 0.4 μ_B Cu^{-1} for the ordering to remain unobservable.

5.5. Discussion

Perturbations from ideality provide a useful method for revealing the properties of an underlying ground-state. This approach is particularly important when searching for ground-states as elusive as quantum-spin-liquids. With this in mind the larger the library of studied materials and the wider the variety of perturbations, the more information can be gleaned about the properties of the different types of quantum-spin-liquids that they display.

For understanding the spin-liquid ground-state in isostructural kapellasite, the less dynamic ground-state in haydeeite will provide important information about the correlations present. Studies of the crystallography and high temperature susceptibility suggest that that these two materials should display near-identical magnetic properties, yet strikingly different low-temperature physics is seen. Spin-glass ground-states are not uncommon in frustrated magnets,[**22**] but typically found in dilute magnetic systems.[**24**] With this in mind it is worth considering the possibility that the incomplete occupation of the kagome lattice by Cu^{2+} ions may result in this disordered ground-state. This hypothesis appears unlikely as it is inconsistent with the dynamic ground-state observed in the more disordered analogue kapellasite despite its greater

loss of Cu^{2+}. Spin-freezing is brought about by another mechanism. However, the DFT calculations do provide a scenario through which this could occur - the Mg^{2+} may be capable of mediating a stronger diagonal exchange, J_{d1} (figure 5.4), than in kapellasite.[**8**] Any effect of disorder on this site would be correspondingly larger.

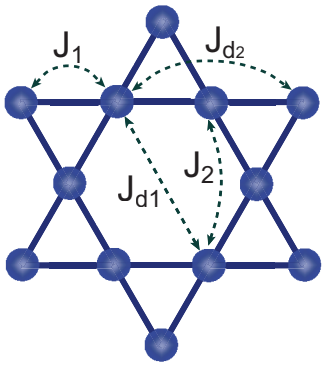

FIGURE 5.4. An illustration of the possible further neighbour exchange pathways within the kagome network.

It is not necessarily clear that the spin glass that this could lead to is conventional as the observed responses could also be due to a slowing down of the spin-liquid responses seen in kapellasite. The low moment observed in the hysteresis data could then be characteristic only of the component of the spin-liquid/spin-glass phase that the field can couple to. If the spin glass component in haydeeite is more conventional, then the low moment could be characteristic of quantum-fluctuations, indicating that haydeeite is close to a quantum critical point between the two phases.

5.6. Conclusions

This chapter shows that haydeeite is isostructural with kapellasite and that the materials possess very similar superexchange pathway bong angles and lengths. Despite this, haydeeite displays a markedly different magnetic ground-state that can be explained by the enhancement of further-neighbour exchange interactions, J_{d1}, upon substitution of Mg on the lattice. Upon cooling below 6 K haydeeite undergoes a magnetic transition to a ground-state with spin glass-like character. This observation may indicate that the field is only capable of coupling to a small component of the spin, or that enhanced quantum fluctuations are present that are reducing its value.

5.7. Future work

Definitive confirmation of the spin-glass ground-state is yet to be found and muon spin relaxation spectroscopy can provide this. A frozen, random-distribution of spins leads to a characteristic, Kubo-Toyabe,[**25**] shape in the muon relaxation spectrum and measurements are currently under way in collaboration with Dr. F. Bert and Prof. P. Mendels.

Understanding the short-range order in this frustrated magnet will also provide insight into the nature of the spin liquid state it displays. To probe these correlations experiments such as magnetic-EXAFS may be used to obtain a spin-pair-distribution function, though such experiments are likely to be challenging.

Additionally, measurements under applied pressure could be of great interest, as pressure-enduced changes in the crystal structure could be used to tune the balance of exchange strengths through this quantum-critical point, potentially melting the frozen disordered state of the spin glass.[**27**]

References

[1] Schluter, J.; Malcherek, T. *N. Jb. Miner. Abh.* **2007**, *184*, 39.
[2] Colman, R. H.; Sinclair, A.; Wills, A. S. *Chem. Mater.* **2010**, *22*, 5774.
[3] Krause, W.; Bernhardt, H-J.; Braithwaite, R. S. W.; Kolitsch, U.; Pritchard, R. *Miner. Mag.* **2006**, *70*, 329.
[4] Shannon, R. D. *Acta Crystallogr.* **1976**, *A32*, 751.
[5] Colman, R. H.; Sinclair, A.; Wills, A. S. *Chem. Mater.* **2011**, *23*, 1811.
[6] Chu, S.; McQueen, T. M.; Chisnell, R.; Freedman, D. E.; Müller, P.; Lee, Y. S.; Nocera, D. G. *J. Am. Chem. Soc.* **2010**, *132*, 5570.
[7] Lee, S. H.; Kikuchi, H.; Qiu, Y.; Lake, B.; Huang, Q.; Habicht, K.; Kiefer, K. *Nature Mater.* **2007**, *6*, 853.
[8] Janson, O.; Richter, J.; Rosner, H. *Phys. Rev. Lett.* **2008**, *101*, 106403.
[9] Janson, O.; Richter, J.; Rosner, H. *J. Phys. Conf. Ser.* **2008**, *145*, 012008.
[10] Colman, R. H.; Ritter, C.; Wills, A. S. *Chem. Mater.* **2008**, *20*, 6897.
[11] Feitknecht, W.; Maget, K. *Helv. Chim. Acta* **1949**, *218*, 1639.
[12] Ostwald, H. R.; Feitknecht, W. *Helv. Chim. Acta* **1964**, *47*, 273.
[13] Feitknecht, W.; Maget, K. *Helv. Chim. Acta* **1949**, *219*, 1653.
[14] TOPAS (Version 4.1), program available from Bruker AXS, Östliche Reinbruckenstrasse 50, 76187 Karlsruhe, Germany.
[15] Rigol, M.; Singh, R. P.; *Phys. Rev. Lett.* **2007**, *98*, 207204.
[16] Hiroi, Z.; Hanawa, M.; Kobayashi, N.; Nohara, M.; Takagi, H.; Kato, Y.; Takigawa, M. *J. Phys. Soc. Jpn.* **2001**, *70*, 3377.

[17] Okamoto, Y.; Toshida, H.; Hiroi, Z. *J. Phys. Soc. Jpn.* **2009**, *78*, 33701.
[18] Malcherek, T.; Schluter, J. *Acta Crystall. B-Stru.* **2007**, *63*, 157.
[19] Wills, A. S. VaList, Program available from www.ccp14.ac.uk
[20] Chu, S. *J. Phys.: Conf. Ser.* **2011**, *273*, 012123.
[21] Matsuda, M.; Katsumata, K.; Kojima, K. M.; Larkin, M.; Lue, G. M.; Merrin, J.; Nachumi, B.; Uemura, Y. J.; Eisaki, H.; Motoyama, N.; Uchida, S.; Shirane, G. *Phys. Rev. B* **1997**, *55*, 11953.
[22] Bisson, W. G.; Wills, A. S. *J. Phys. Condens. Mat.*, **2008**, *20*, 452204.
[23] Wills, A. S.; Harrison, A.; Mentink, S. A. M.; Mason, T. E.; Tun, Z. *E. P. L.* **1998**, *42*, 325.
[24] Domb, E. R.; Tsai, T. H.; Gruzalski, G. R.; Sellmyer, D. J.; Borg, R. J. *B. Am. Phys. Soc.* **1975**, *20*, 345.
[25] Kubo, R. *Hyperfine Interact.* **1984**, *17*, 433.
[26] Schütz, G.; Knulle, M.; Ebert, H. *Phys. Scripta* **1993**, *303*, T49A.
[27] Gehring, G. A. *E. P. L.* **2008**, *82*, 60004.

CHAPTER 6

Vesignieite, $BaCu_3(VO_5H)_2$

Whilst all previously presented examples of kagome magnets studied in this thesis have been from the same family of copper-hydroxy-halide minerals, $S = \frac{1}{2}$ kagome magnets are not limited to this class. Outside the atacamites, the best known examples are the minerals volborthite, $Cu_3V_2O_7(OH_2)\cdot H_2O$, and vesignieite, $BaCu_3(VO_5H)_2$. These minerals add an important new perspective on the physics of $S = \frac{1}{2}$ kagome magnets as they do not retain the three fold rotation symmetry of the triangular lattice; they are instead monoclinically distorted. While it would naively be expected that this symmetry reduction would remove the frustration of the lattice and cause long-range magnetic order, they have been found to still be frustrated and to condense into QSL states. The studies presented in this chapter show that vesignieite is close enough to 3-fold rotation symmetry to be considered a virtually ideal material. This is a key finding as previously reported samples were much poorer in quality, making it impossible to determine whether their magnetic responses are exclusively due to the kagome physics or contributions from magnetic defects and impurities.

This chapter outlines efforts to synthesise better quality samples using a new synthetic approach. Magnetic and structural characterisations of the samples are also presented that show vesignieite to go through a magnetic transition upon cooling below ~ 9 K to an unconventional magnetic ground-state which features both dynamic and disordered-frozen components.

The work was carried out by myself together with the M.Sci. student David Boldrin (UCL), whom I supervised.

6.1. Introduction

Vesignieite, $BaCu_3(VO_5H)_2$, is a barium copper vanadate mineral with distorted Cu^{2+} kagome planes (figure 6.1a).[**1**] The hexagonal voids of the kagome planes are capped above and below by VO_4 tetrahedra that are hydrogen bound by the apical oxygen (O4) to an OH group (O1) of the next plane. Interstitial charge balancing Ba^{2+} ions are also present between planes (figure 6.1b).

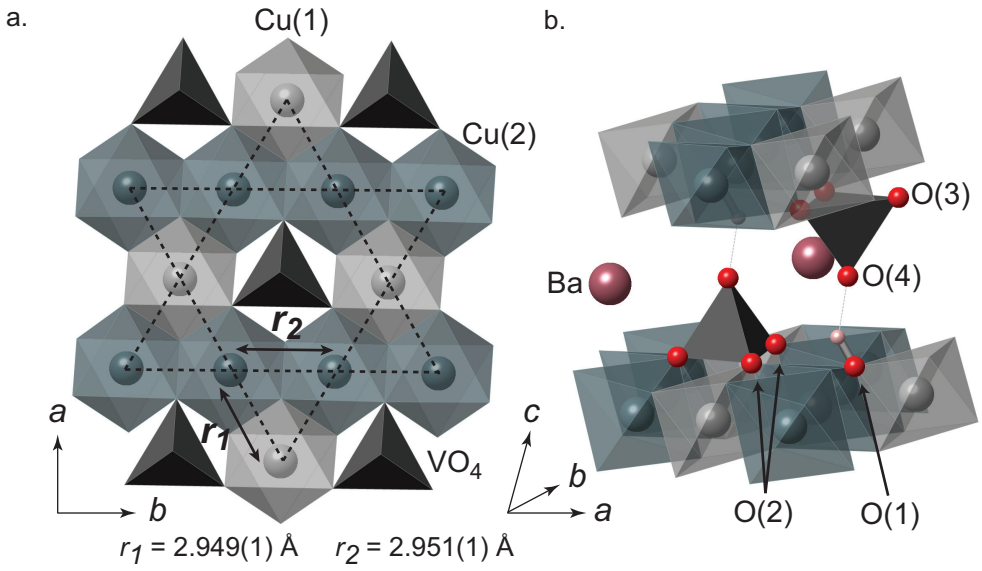

FIGURE 6.1. The crystal structure of vesignieite, showing a. that the kagome lattice of vesignieite has two crystallographically distinct CuO_6 octahedra, and possesses near 3-fold rotational symmetry, and b. that the kagome planes are coupled by VO_4 tetrahedra, hydrogen bonded to hydroxyl groups in the neighbouring planes. The presence of interstitial charge balancing Ba^{2+} ions are also shown.

Vesignieite is described by the monoclinic space-group C12/m1 and the kagome lattice is made up of two crystallographically distinct Cu positions. Consequently, there are formally two unequal exchange pathways between these ions. The difference in Cu_1–Cu_2 (r_1) and Cu_2–Cu_2 (r_2) bond distances between the two sides of the isosceles triangle calculated using the literature mineral structure[**1**] gives rise to a distortion away from equilateral geometry of $(\frac{r_2-r_1}{r_1}) \times 100 = 0.24$ %.

Whilst any distortion of the kagome lattice holds the potential to break the degeneracy and destabilise a spin-liquid ground-state, the closely related compound volborthite[**2**] has shown spin-liquid states can be surprisingly robust to a monoclinic distortion. In volborthite the symmetry lowering is far greater than in vesignieite, $(\frac{r_2-r_1}{r_1}) \times 100 = 3.06$ %.[**4**] The difference in the values of the exchange terms related to this distortion are not yet known, but theoretical calculations suggest it could be as much as 20 %.[**3**] Despite this structural distortion and a large negative Weiss temperature, $\theta_W = -115$ K,[**4**] dc susceptibility measurements, ^{51}V-NMR and muon spin relaxation spectroscopy have shown that the spins in volborthite remain dynamic down to 60 mK.[**5, 6**] These data do, however, show a weak spin glass-like component below $T_g = 1.1$ K, evidenced by a small hysteresis in susceptibility measurements, but this is believed to be due to spin defects in the lattice.[**5**]

Another important difference between volborthite and vesignieite; and the herbertsmithites, kapellasite and haydeeite, is that the kagome lattices in the former are not created by the dilution of another lattice. This circumvents the problems that arise from the possibility of site-exchange between metal ions. As these mineral structures also feature no sites suited for the mediation of 3-dimensional superexchange, highly 2-dimensional kagome physics is expected.

A final consideration, put forward in [**7**], when comparing the vesignieite and volborthite structures, aside from the smaller lattice distortion, is that of the bonding and valence orbitals in these materials. Both of these materials show a room-temperature Jahn-Teller distortion of the Cu^{2+} octahedra, that indicates the valence 3d e_g-orbitals are no longer degenerate. In volborthite, Cu1 octahedra show a *tetragonal compression* suggesting that the unpaired spin will reside in the z^2 orbital, whilst the Cu2 site shows a *tetragonal elongation* and hence the unpaired spin is expected to reside in the $x^2 - y^2$ orbital. This disparity is likely to lead to a further difference in superexchange across the two different paths Cu1–Cu2 *vs.* Cu2–Cu2. In vesignieite, a *tetragonal compression* is found on both the Cu_1 and Cu_2 sites indicating that the unpaired spins reside in the same, z^2, orbital type (shown in figure 6.2, reproduced from reference [**7**]). This suggests that vesignieite is an excellent model system for the observation of a quantum spin liquid ground-state.

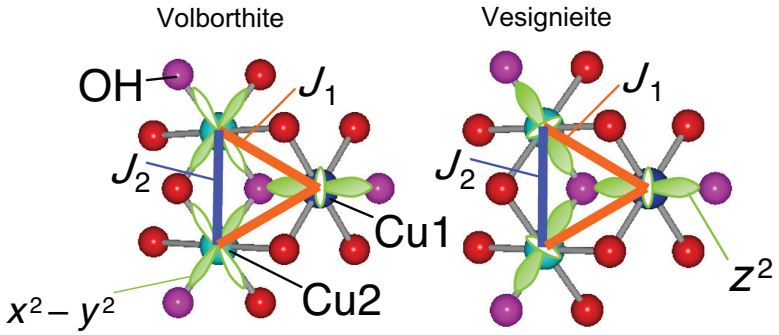

FIGURE 6.2. An illustration of the expected spin-containing valence orbitals of volborthite and vesignieite. Consideration of the Jahn-Teller distortions to the Cu^{2+} ion sites suggests that the unpaired spin on the two sites in volborthite will reside in different, $x^2 - y^2$ and z^2, orbital types. Conversely all unpaired spins in vesigniete are expected to reside in z^2 orbitals. Reproduced from [**7**].

6.2. Synthesis

Previously reported samples of vesigniete have been synthesised by conventional hydrothermal reaction of vanadium pentoxide, barium acetate and copper hydroxide in PTFE-lined steel hydrothermal bombs.[**7**] The X-ray diffraction pattern of the samples (figure 6.3, reproduced from [**7**]) shows broad peaks indicative of low crystallinity and no Rietveld refinement of the structure was presented. Attempts to repeat or improve the reported synthesis all lead to impure and poorly-crystalline samples.

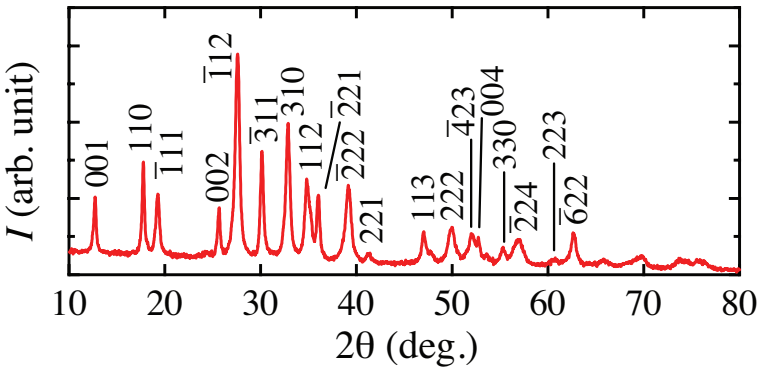

FIGURE 6.3. An X-ray diffraction pattern, using Cu K_α radiation, showing the broad diffraction peaks of previous vesignieite samples indicative of poor crystallinity. Reproduced from [**7**].

Upon consideration of the reaction conditions, it was evident that the insolubility of the $Cu(OH)_2$ reagent is a likely cause of the reaction difficulties, even under elevated temperatures and pressures. With this in mind, strategies to better solubilise the $Cu(OH)_2$ groups were investigated. Complexation of the copper hydroxide with ammonium hydroxide, known as *Schweizer's reagent* $[Cu(NH_3)_4(OH_2)_2]^{2+}{\cdot}2[OH]^-$, was found the most suitable method as slow evaporation of the ammonia allows controlled release of $Cu(OH)_2$ back into solution for crystallisation.[**8**]

The reaction was attempted with a range of ammonium hydroxide solution concentrations and temperatures. Refluxing the solution with a long reflux-condenser was found to slow the ammonia evaporation suitably and give rise to the most crystalline samples, as studied by laboratory X-ray diffraction. Further improvements to sample crystallinity were gained by an additional hydrothermal annealing step after isolation from the initial reaction conditions. This type of additional annealing has previously been shown to allow isolation of high-quality samples of volborthite, minimising the presence of magnetic and structural defects.[**9**]

6.2.1. Optimised conditions

The final synthetic protocol for the synthesis of high-quality samples of vesignieite is as follows:

Copper hydroxide, $Cu(OH)_2$ (0.678 g), was dissolved in a solution of ammonium hydroxide, NH_4OH (100 ml, 28 % NH_3), to produce a dark purple solution of *Schweizer's reagent*. To this solution, vanadium pentoxide, V_2O_5 (0.154 g), and barium acetate, $Ba(CH_3COO)_2$ (0.217 g), was added before heating to reflux with stirring. After $\sim$ 4 hrs all traces of ammonia had fully evaporated to leave a suspension of green polycrystalline product. The product was isolated by filtration and washed with water (3×20 ml). The sample ($\sim$ 1 g) was then hydrothermally annealed in water (or 99.9 atom % D_2O for preparation of a deuterated sample) in a 25 ml, PTFE lined, steel bomb for 48 hrs at 190°C. The recovered product was found to be phase pure by laboratory X-ray diffraction.

6.3. DC SQUID magnetometry

To study the magnetic properties of these new high-quality samples of vesignieite, $BaCu_3(VO_5H)_2$, measurements of magnetic susceptibility *vs.* temperature were performed. Figure 6.4a shows a plot of $\chi \, vs. \, T$. The high temperature region (200 − 300 K) can be fitted to the Curie-Weiss law to give a Weiss temperature $\theta_W = -85(5)$ K, indicative of strong antiferromagnetic correlations and in agreement with published data.[**7**] Despite the strength of the exchange, no sharp features are seen that would indicate a magnetic ordering transition. Instead, below 9 K a weak kink is seen in the susceptibility data (figure 6.4b.) with the opening of a splitting between zero-field-cooled and field-cooled measurements. These features are indicative of a spin glass-like freezing transition to a disordered ground-state. A rise in $\chi(T)$ occurs upon cooling below this transition suggesting that even these higher-quality samples may possess some magnetic defects that have a characteristic Curie-tail. Though at this point such an explanation is by no means confirmed, as attempts made to reproduce the data treatment presented in [**7**] and subtract the Curie-tail χ_{impurity} component led to unphysical values of χ_{kagome}.

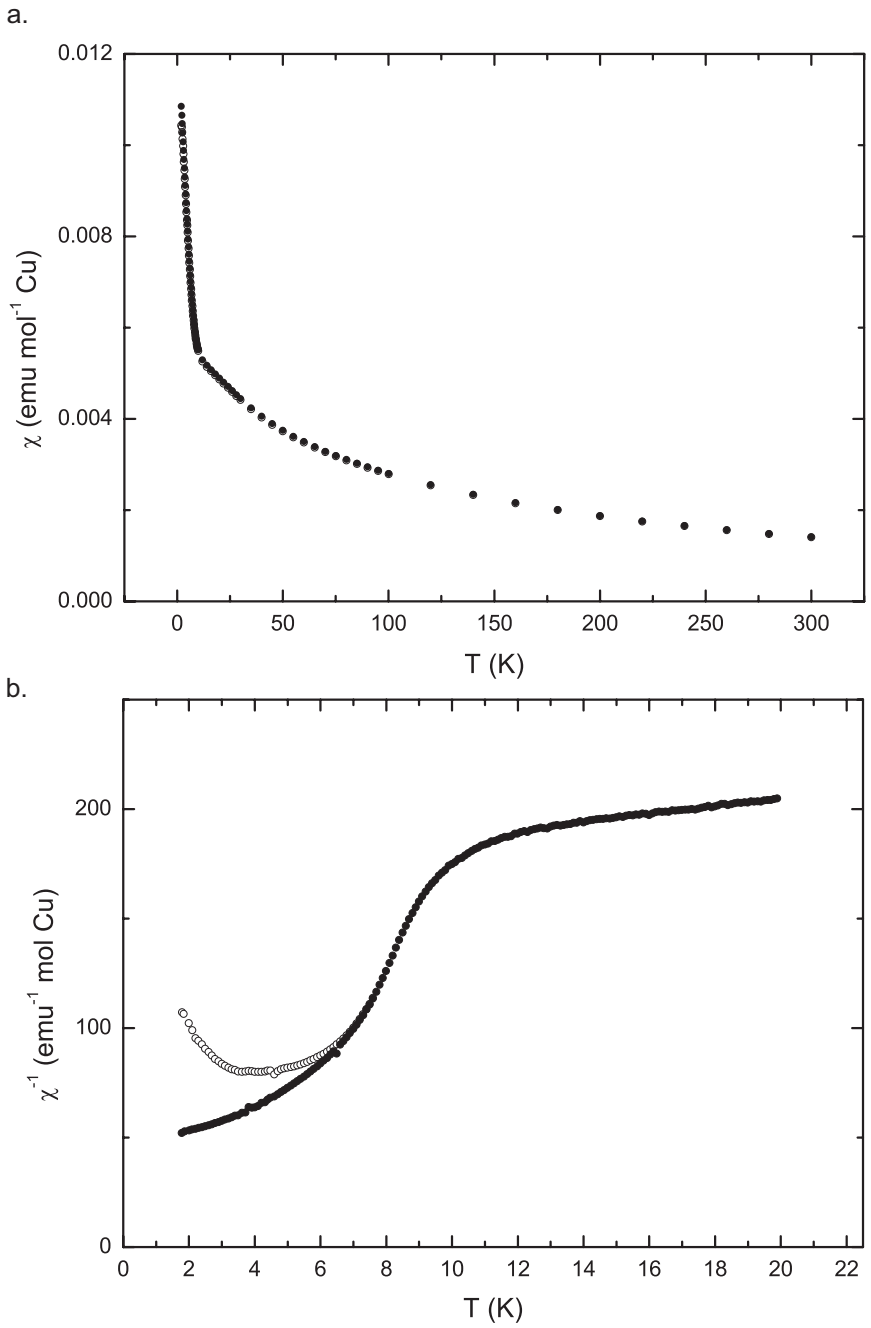

FIGURE 6.4. a. Measurements of field cooled (•) and zero-field cooled (○) magnetic susceptibility χ *vs.* T of a 40 mg sample of vesignieite, $BaCu_3(VO_5H)_2$ in an applied field of 100 Oe. b. Low temperature plot of χ^{-1}(T) showing field-cool / zero-field-cooled splitting below a kink at $T_g = 9\ K$ indicative of spin glass-like component.

6.4. Powder neutron diffraction

To confirm the sample quality, obtain a refined crystal structure and study any changes in magnetic scattering, powder neutron diffraction patterns were collected from a deuterated sample of vesignieite at several temperatures using the WISH *tof* diffractometer at ISIS.

6.4.1. Structural refinements

Diffraction patterns were collected at $T = 1.5$, 6, 10, 15, 30 and 50 K and Rietveld refinements of the crystal structure were performed using the program FullProf.[**10**] The data and refined fit for data taken at 1.5 K are shown in figure 6.5.

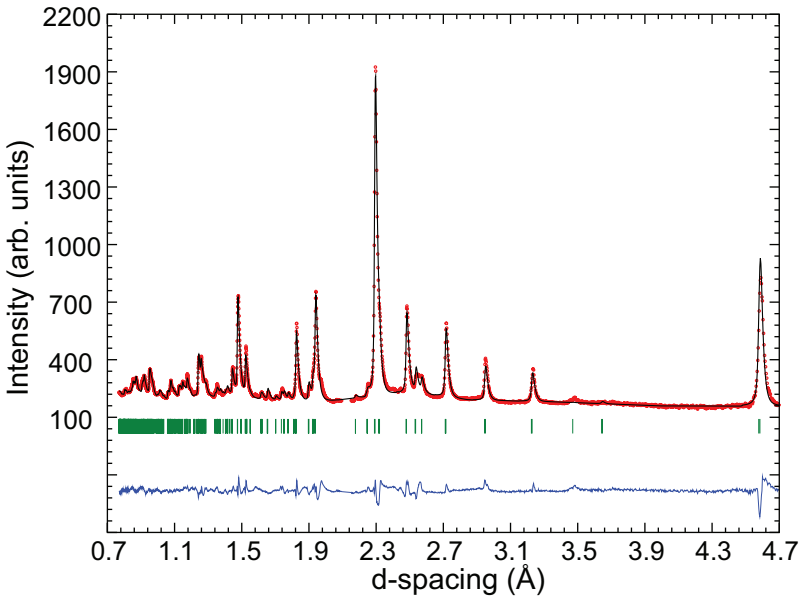

FIGURE 6.5. Powder neutron diffraction data and Rietveld refinement fit collected from a deuterated vesignieite sample, $BaCu_3(VO_5D)_2$, at $T = 1.5$ K. The red points are the data, the black line is the fit, the blue curve is the difference and the tick marks indicate reflection positions. Refined lattice parameters, in the monoclinic spacegroup C12/m1 (# 12) are $a = 10.210(2)$ Å, $b = 5.903(1)$ Å, $c = 7.739(1)$ Å and $\beta = 116.15(1)°$. The final R_{WP} is 3.61.

Refined structural parameters are given in table 6.1. Due to the low neutron scattering length of vanadium (0.0184 fm) attempts to refine its atomic position failed and its parameters were fixed at literature values.[**1**] No significant structural changes were seen across the temperature range studied. Promisingly, the kagome lattice in our synthetic samples is found to be far less distorted than that of the mineralogical

studies of vesignieite: $(\frac{r_2-r_1}{r_1}) \times 100 = 0.07$ % (our samples) and 0.24 % (vesignieite mineral samples).

TABLE 6.1. The refined crystallographic parameters for deuterated vesignieite, $BaCu_3(VO_5D)_2$, at $T = 1.5$ K, using data collected on the WISH time-of-flight diffractometer.

Wyckoff Site	Atom Name	x	y	z	U_{iso}
$2c$	Ba	0	0	$\frac{1}{2}$	0.0041(1)
$2a$	Cu1	$\frac{1}{2}$	$\frac{1}{2}$	0	0.0032(3)
$4e$	Cu2	$\frac{1}{4}$	$\frac{1}{4}$	0	0.0035(2)
$4i$	V	0.08980	$\frac{1}{2}$	0.26970	0.0088(4)
$4i$	O1	0.1682(2)	0	0.1024(2)	0.0038(9)
$18j$	O2	0.4919(14)	0.2462(3)	0.20634(1)	0.0104(11)
$4i$	O3	0.2171(8)	$\frac{1}{2}$	0.1755(3)	0.0053(12)
$4i$	O4	0.2907(1)	0	0.2598(1)	0.0336(16)
$4i$	D	0.2067(2)	0	0.25984(1)	0.0161(10)

6.4.2. Magnetic scattering

The high neutron flux at long wavelength produced by the WISH diffractometer is ideal for studying changes in magnetic scattering. Upon cooling through the spin glass-like transition no evidence was seen for the development of diffuse scattering, characteristic of short-ranged magnetic order around some non-zero Q-vector, as would be expected. There is, however, a change in the high d-spacing (low Q) component to the scattering on cooling. This appears to be paramagnet-like at 50 K, following well the form factor of Cu^{2+} (figure 6.6a). Below $\sim$ 15 K the intensity of this feature drops (figure 6.6b shows the temperature-dependence of the integrated intensity of this d-spacing range normalised to the 50 K data scattering) but no additional features appear. This last point is very curious and suggests that the scattering is either moving outside the kinematic (Q, ω) window of WISH or that the spins are condensing into a state that cannot be characterised with neutrons, *e.g.* an RVB or a valence bond-crystal state made up of non-magnetic singlets.

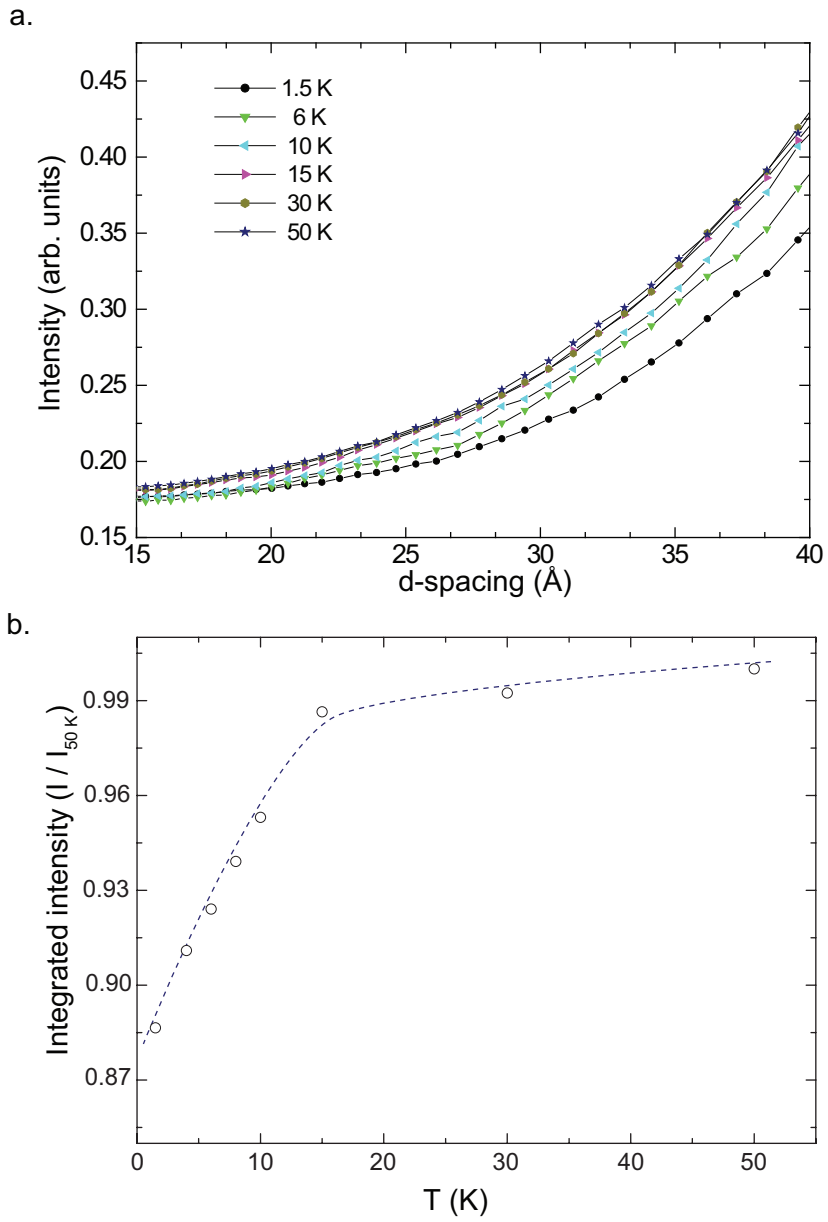

FIGURE 6.6. a. A plot showing the change in high d-spacing scattering upon cooling the sample. The red lines fitted to the 50 K and 1.5 K data show the paramagnetic scattering form-factor for Cu^{2+} moments. b. Integrated intensity of the scattering in the range $15 < d < 40$ Å^{-1} as a function of temperature, normalised to the 50 K scattering. The dashed line is a guide to the eye. A prominent reduction in scattering is seen when cooling below the $T_g = 9$ K transition.

6.5. Discussion

The spin glass-like transition observed in susceptibility data, and further confirmed by the apparent loss of paramagnetic-like scattering in neutrons has also been corroborated by recently published muon spin relaxation (MuSR) measurements.[**11**] The MuSR measurements were performed on these samples of vesignieite as part of a collaboration with Dr. F. Bert and Prof. P. Mendels and will be summarised here. For full details of the data analysis and fitting procedure, performed by Dr. F. Bert, please refer to [**11**].

Due to their intrinsic magnetic moment, when a spin polarised muon is implanted into a sample the depolarisation rate of the muon gives a direct probe of the local spin-dynamics within the sample. Fits to the temperature dependent muon spectra of these high quality vesignieite samples show two distinct features: a loss of initial asymmetry, indicative of a disordered frozen component; and an increase in the muon relaxation rate indicative of slowing spin-dynamics. These responses are shown in figure 6.7, reproduced from [**11**].

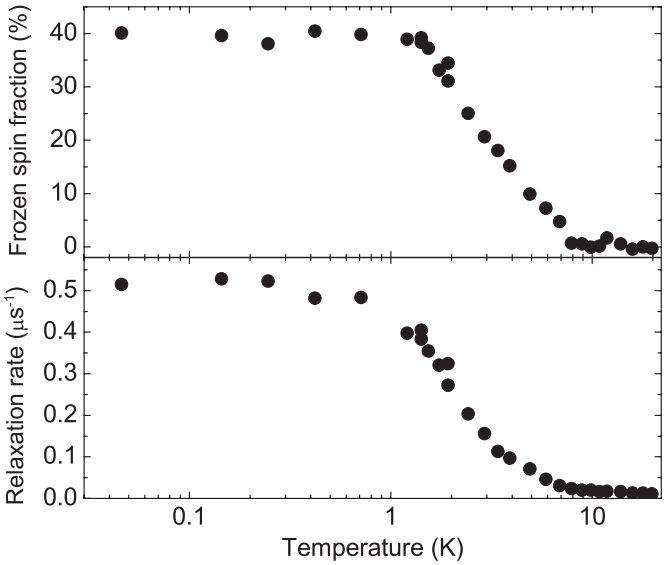

FIGURE 6.7. Plots showing information extracted from fits to temperature dependent muon spin relaxation measurements, reproduced from [**11**]. Top, shows the loss of initial asymmetry in the spectrum, interpreted as the increase in a dissordered frozen spin fraction upon cooling. Bottom. shows an increase in muon relaxation rate upon cooling, indicative of slowing spin dynamics.

The loss of initial asymmetry can be attributed to a fraction of the spins that relax the muons very quickly, outside of the the MuSR time-window. This loss is expected

to occur at a magnetic ordering transition, but the lack of characteristic oscillations in the MuSR spectrum confirms the absence of long-range magnetic order. As such, this loss is assigned to a freezing of the spins into a randomly distributed static state. The temperature dependence of this *frozen fraction* is seen in the top panel of figure 6.7. At the $T_g = 9$ K spin glass-like transition a fraction of the spins are seen to be frozen. This fraction further increases upon cooling down to ~ 1 K by which time it has reached ~ 40 % of the spins, but does not increase further upon cooling past 1 K. This indicates that the remaining 60 % of the sample spins do not freeze into this frozen state, but are remaining dynamic down to 60 mK.

The fitted muon relaxation rate displays a strikingly similar temperature dependence. Upon cooling through the $T_g = 9$ K transition, the remaining *dynamic* fraction of the spins is seen to relax the muons more quickly, indicating a slowing of the spin dynamics. At a conventional spin-glass transition this relaxation rate would quickly rise, resulting in a loss of all initial asymmetry. Instead the dynamics of the remaining fraction is seen to increase much more slowly, and plateaux at ~ 1 K, indicating a persistence of the liquid-like spin component in the magnetic ground-state of this material.

Observation of these two conflicting, dynamic *and* static, responses could usually be assigned to sample inhomogeneity, with distinct responses from the different regions or phases, but the similarities in temperature dependence of these two responses suggests they are intimately linked as part of the same ground-state manifold. This leads to the realisation that vesignieite is a highly unconventional kagome magnet with a ground-state that consists of dynamic and frozen components on the MuSR time-scale, as may occur in a QSL that features a large distribution of time-scales for its spin dynamics.

Despite the expectation from structural analysis that vesigniete should display near-ideal kagome ground-state physics, an additional perturbation must be at play, breaking the degeneracy of the expected QSL state and inducing partial spin freezing. Unlike haydeeite, no evidence of further neighbour exchange is seen in susceptibility measurements and so alternative perturbations must be considered. If large enough, an additional anti-symmetric exchange term, a *Dzyaloshinskii-Moriya* component, in the magnetic Hamiltonian would destabilise a QSL ground-state and could induce spin order. Theoretical studies have shown that for this to occur, the ratio of anti-symmetric exchange, D, to superexchange, J must be larger than $D/J > 0.1$.[**12**]

Analysis of electron spin relaxation (ESR) measurements on the kagome magnet herbertsmithite have found $D/J \sim 0.08$,[**13**] explaining the observed pure-QSL ground-state and we propose that this perturbation is larger in vesignieite leading to partial freezing rather than complete spin order. The observation of a large dynamic component in the ground-state suggests that whilst $D/J > 0.1$, it must be close to the quantum critical point of this D/J phase diagram.

6.6. Conclusions

A new synthetic method for the production of high quality vesignieite samples has been presented, utilising Schweizer's reagent to solve $Cu(OH)_2$ solubility issues. A full structural characterisation of these samples, using powder neutron diffraction data, has led to the confirmation that vesignieite has a near-ideal kagome lattice of $S = \frac{1}{2}$ Cu^{2+} ions.

A kink in the susceptibility data at 9 K showing deviation of zero-field-cooled from field-cooled measurements, coupled with the absence of magnetic Bragg scattering in the diffraction data suggests a transition to a spin glass-like state. The onset of this state is marked by a loss of paramagnetic-like scattering in the neutron diffraction, with no sign of the development of broad features usually associated with the short-range order of a conventional spin glass.

Analysis of muon spin relaxation spectroscopy data, performed by Dr. F. Bert, is also discussed, and confirms the spin glass-like characteristics of one component of the ground-state. The ground-state in vesignieite is shown not to be a conventional spin glass, as a considerable fraction of the spins remain dynamic down to 60 mK. This mixture of both static *and* dynamic components to the ground-state suggests that vesignieite is close to a quantum-critical-point, where the dynamic character of the QSL is being retarded by an additional anti-symmetric exchange term, inducing partial spin freezing.

6.7. Future work

To confirm the presence and magnitude of the anti-symmetric exchange component, measurements of the temperature dependence of the ESR linewidth must be performed. A collaboration with Dr. A. Zorko has recently been established in order to perform these measurements.

The presence of vanadium in this material also opens the opportunity for ^{51}V-NMR measurements to be performed. NMR provides a local probe of the magnetic susceptibility, circumventing complications that arise when measuring bulk susceptibilities as any impurity contributions can be distinguished from the main phase.

To further probe the effects of perturbations to the ground-state properties, the similar ionic radii of Cu^{2+} and Zn^{2+} may allow the possibility of controlled diamagnetic dilution of the kagome lattice. This has been found possible in the synthesis of the related mineral volborthite.

References

[1] Zhesheng, M.; Xiaoling, Z. *Dizhi Xuebao*, **1990**, *64*, 302.

[2] Lafontaine, M.; Lebail, A.; Ferey, G. *J. Solid State Chem.*, **1990**, *85*, 220.

[3] Sindzingre, P. *arxiv:*0707.4264v1.

[4] Hiroi, H.; Hanawa, M.; Kobayashi, N.; Nohara, N.; Takagi, M.; Kato, Y.; Takigawa, M. *J. Phys. Soc. Jpn.*, **2001**, *70*, 3377.

[5] Bert, F.; Bono, D.; Mendels, P.; Ladieu, F.; Duc, F.; Trombe, J. -C.; Millet, P. *Phys. Rev. Lett.*, **2005**, *95*, 087203.

[6] Yoshida, M.; Takigawa, M.; Yoshida, H.; Okamoto, Y.; Hiroi, Z. *Phys. Rev. Lett.*, **2009**, *103*, 077207.

[7] Okamoto, Y.; Yoshida, H.; Hiroi, Z. *J. Phys. Soc. Jpn.*, **2009**, *78*, 033701.

[8] Wu, C. D.; Lu, C. Z.; Lin, X.; Lu, S. F.; Zhuang, H. H.; Huang, J. S. *J. Alloy Compd.* **2004**, *368*, 342.

[9] Yoshida, H. Okamoto, Y.; Tayama, T.; Sakakibara, T.; Tokunaga, M.; Matuso, A.; Narumi, Y.; Kindo, K.; Yoshida, M.; Takigawa, M.; Hiroi, Z.*J. Phys. Soc. Jpn.*, **2009**, *78*, 043704.

[10] Rodriguez-Carvajal, J. *Physica B*, **1993**, *192*, 55.

[11] Colman, R. H.; Bert, F.; Boldrin, D.; Hillier, A. D.; Manuel, P.; Mendels, P.; Wills, A. S. *Phys. Rev. B*, **2011**, *83*, 180416.

[12] Cépas, O.; Fong, C. M.; Leung, P. W.; Lhuillier, C. *Phys. Rev. B* **2008**, *78*, 140405.

[13] Zorko, A.; Nelluta, S.; van Toll, J.; Brunel, L. C.; Bert, F.; Duc, F.; Trombe, J. C.; de Vries, M. A.; Harrison, A.; Mendels, P. *Phys. Rev. Lett.*, **2008**, *101*, 026405.

CHAPTER 7

Conclusions

Quantum spin liquids (QSL) remain some of the most sought after ground states in condensed matter physics. These occur when high ground-state degeneracy couples with strong quantum-fluctuations, giving rise to exotic properties and exciting new physics. The archetypal example of a QSL is the resonating valence bond state (RVB), first put forward by Anderson over 20 years ago to underpin the transition to superconductivity in the high-T_c cuprates. While Anderson proposed that this state should also be observable in frustrated insulators based on $S = \frac{1}{2}$ moments, no experimental systems that match the idealised models have yet been found.

With its macroscopic degeneracy, a kagome lattice of antiferromagnetically coupled $S = \frac{1}{2}$ ions is currently considered the most promising system to find the RVB or other QSL ground-states. In recent years several new candidate materials have been put forward, but none have been found to fully encapsulate the simplicity of the theoretical models. This is because all current model systems display some deviations from ideality, be they further-neighbour exchange, site disorder, dilution of the kagome lattice, distortion of the lattice or other terms in the Hamiltonian such as anti-symmetric exchange. To further this field, the onus clearly lies with the synthetic chemists and the production of new or higher quality materials for study.

This thesis details efforts to broaden the library of candidate $S = \frac{1}{2}$ kagome magnets through the synthesis and study of four compounds: 'Mg-herbertsmithite', kapellasite, haydeeite and vesignieite. These materials show a range of responses and reveal different aspects of kagome physics. 'Mg-herbertsmithite', an isomagnetic relative of the well studied Zn-based herbertsmithite, was found to display a QSL ground-state that shared many features with herbertsmithite, and has a comparable Weiss temperature, $\theta_W \sim -300$ K. Our magnetisation data have revealed that the Cu^{2+} spins present on the interlayer sites possess a weak but significant coupling to the moments of the kagome plane. Further, a ferromagnetic transition seen at $T_C \sim 4$ K can be confidently assigned to a ferromagnetic impurity phase that is also seen in Mg-analogues of the paratacamites.

Polymorphs of the herbertsmithites were also investigated: the then discovered minerals kapellasite and haydeeite. In these materials the kagome lattices are generated by the selective diamagnetic dilution of well separated triangular lattices rather than a 3-dimensional pyrochlore network, as occurs in the herbertsmithites. This leads to the expectation of more 2-dimensional physics in these materials. In both kapellasite and haydeeite, susceptibility measurements suggest the presence of competing exchange interactions, as there is clear curvature of the inverse susceptibility at temperatures well above the the small Weiss temperature, $\theta_{\mathrm{W}} \sim -1$ K. Differences in the superexchange predicted by DFT between diamagnetic Zn^{2+} and Mg^{2+}, in kapellasite and haydeeite respectively, lead to clear differences in ground-state properties. Kapellasite is found to remain a QSL down to 60 mK, whilst spin glass-like properties are seen in haydeeite below $T_{\mathrm{g}} \sim 4$ K. Time-of-flight inelastic neutron scattering experiments on kapellasite have shown that the physics of its spin liquid-like response is very different to that of the herbertsmithites. The Q-dependence of the inelastic responses are not peaked at the position expected for singlets made up of nearest-neighbour spins. Instead, the separation of the spins involved in the correlations appears to be larger, indicating that further neighbour exchange plays a defining role.

Another new system that has been attracting attention is vesignieite, where the kagome planes of Cu^{2+} ions are distorted from the idealised three-fold rotation symmetry. Here we used a completely new approach to synthesise samples that are dramatically better than those previously reported in the literature. These new samples have been found to show a weak transition in the magnetic susceptibility and a loss of paramagnetic-like scattering in neutron diffraction data upon cooling below ~ 9 K. Recently published muon spin relaxation spectroscopy measurements on these samples show that this transition is to a complex state, composed of both partially frozen and dynamic spin components. These responses suggest that vesignieite may be close to a quantum-critical-point between a QSL and a conventionally ordered state, perhaps with antisymmetric exchange as the controlling parameter.

Each of the materials presented in this thesis shows some deviation from the ideal $S = \frac{1}{2}$ kagome antiferromagnet. Remarkably, they all display some dynamic ground-state characteristics. It is hoped that this expanding library of candidate $S = \frac{1}{2}$ kagome magnets may help reveal new physics and answer long-standing questions related to the properties of different flavours of QSL.

APPENDIX A

Refinement of synchrotron X-ray diffraction patterns for the complete series of 'Mg-herbertsmithite' samples discussed in chapter 3.

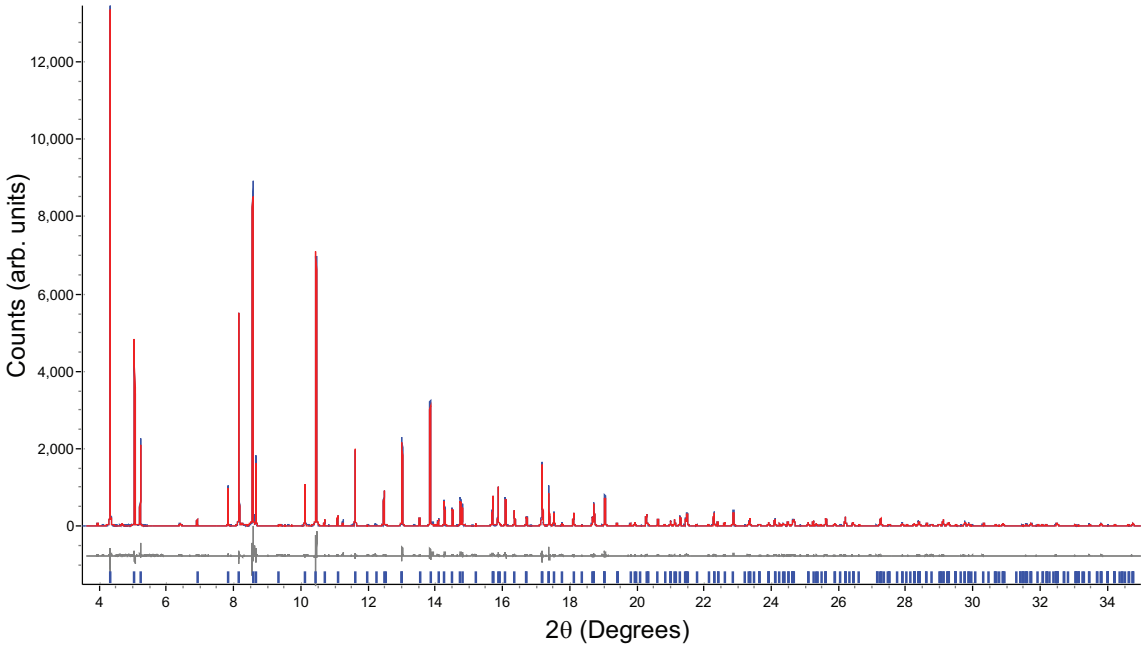

FIGURE A.1. Rietveld refinement using TOPAS of synchrotron powder X-ray diffraction data of Mg-herbertsmithite, γ-$Cu_{4-x}Mg_x(OH)_6Cl_2$ sample **1**, at $T = 295$ K and using X-rays of wavelength $\lambda = 0.412260$ Å. The blue, red, and lower gray lines represent the collected data, fit, and difference plots respectively. The tick marks show reflection positions. The final goodness-of-fit merit factor, χ^2, was 2.449.

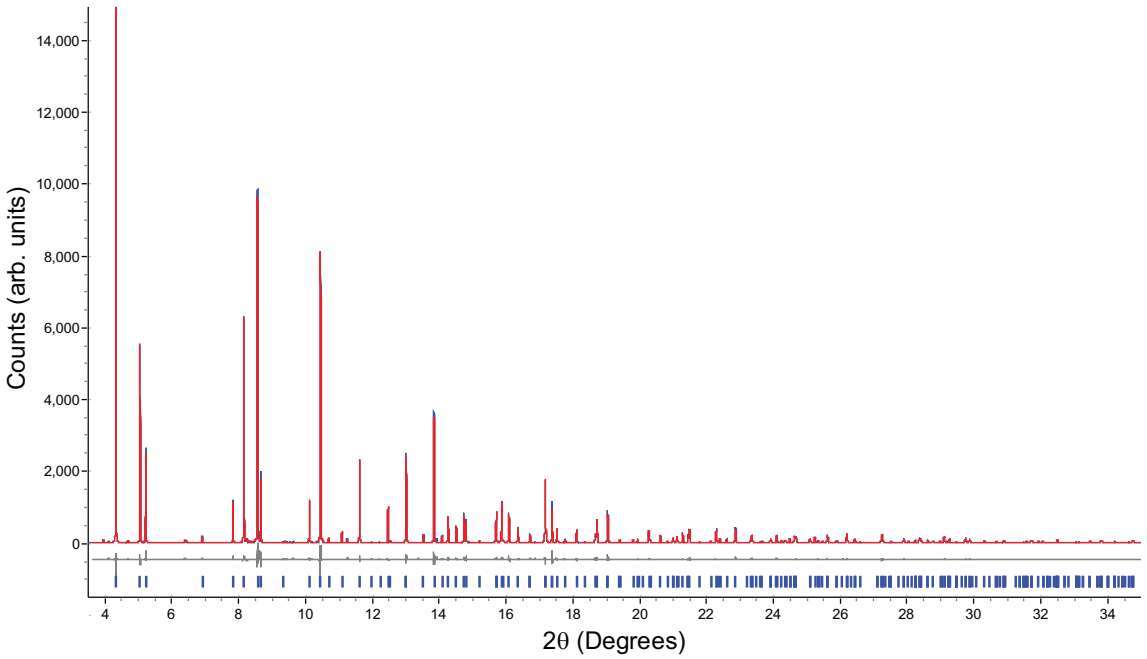

FIGURE A.2. Rietveld refinement using TOPAS of synchrotron powder X-ray diffraction data of Mg-herbertsmithite, γ-$Cu_{4-x}Mg_x(OH)_6Cl_2$ sample **2**, at $T = 295$ K and using X-rays of wavelength $\lambda = 0.412260$ Å. The blue, red, and lower gray lines represent the collected data, fit, and difference plots respectively. The tick marks show reflection positions. The final goodness-of-fit merit factor, χ^2, was 2.228.

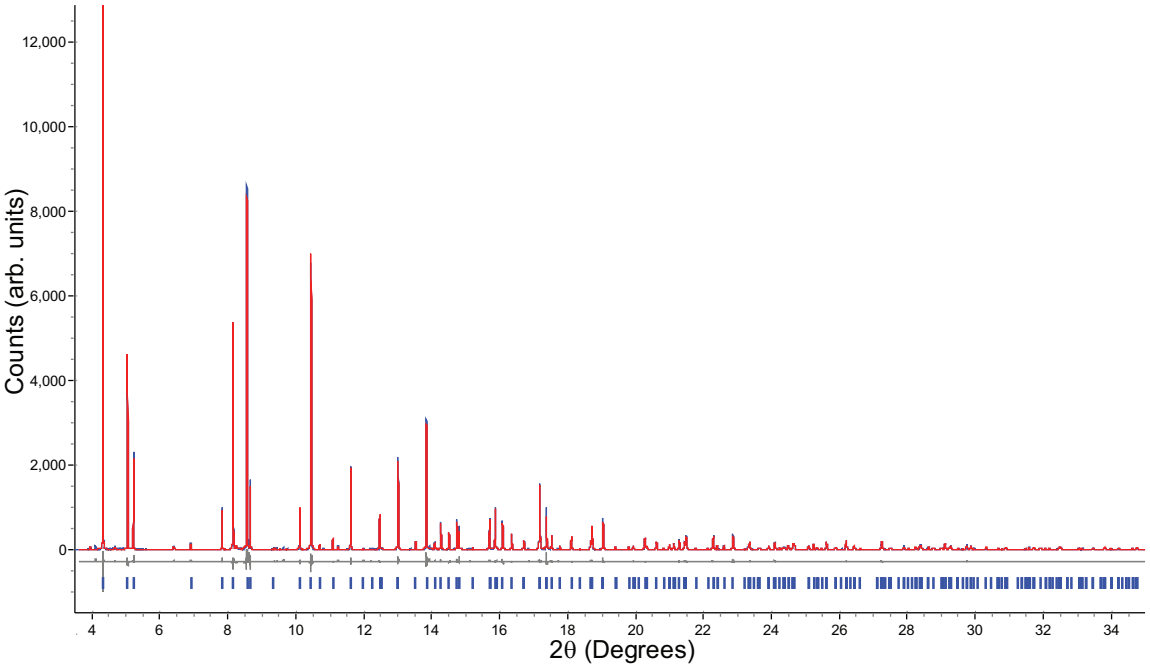

FIGURE A.3. Rietveld refinement using TOPAS of synchrotron powder X-ray diffraction data of Mg-herbertsmithite, γ-$Cu_{4-x}Mg_x(OH)_6Cl_2$ sample **3**, at $T = 295$ K and using X-rays of wavelength $\lambda = 0.412260$ Å. The blue, red, and lower gray lines represent the collected data, fit, and difference plots respectively. The tick marks show reflection positions. The final goodness-of-fit merit factor, χ^2, was 2.080.

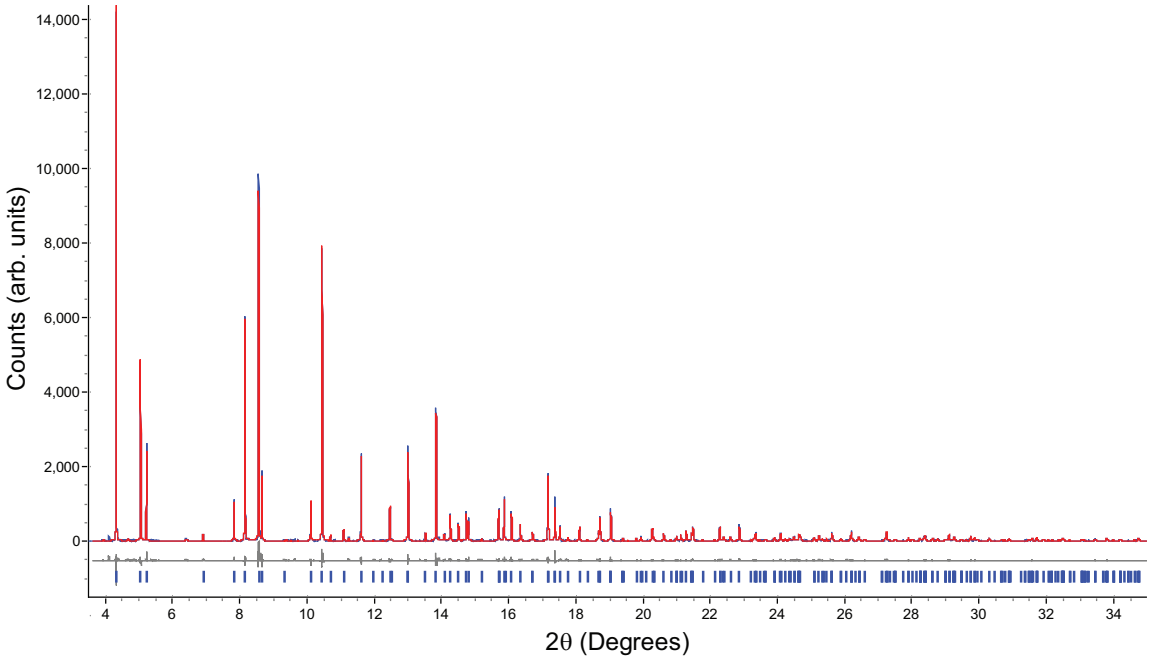

FIGURE A.4. Rietveld refinement using TOPAS of synchrotron powder X-ray diffraction data of Mg-herbertsmithite, γ-$Cu_{4-x}Mg_x(OH)_6Cl_2$ sample **4**, at $T = 295$ K and using X-rays of wavelength $\lambda = 0.412260$ Å. The blue, red, and lower gray lines represent the collected data, fit, and difference plots respectively. The tick marks show reflection positions. The final goodness-of-fit merit factor, χ^2, was 2.206.

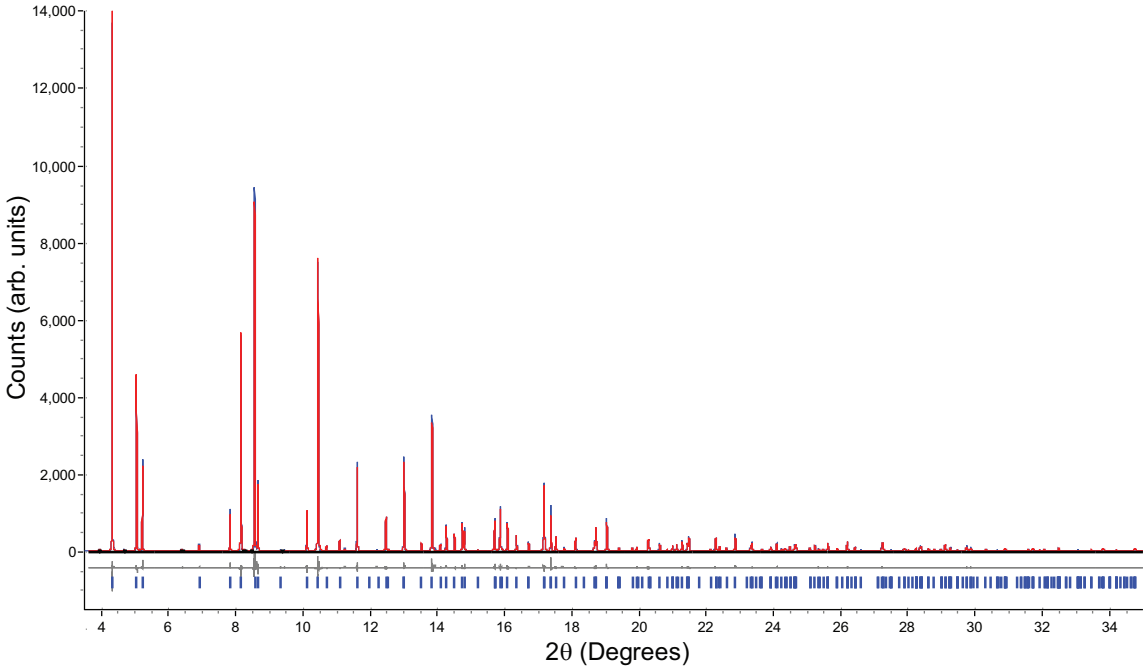

FIGURE A.5. Rietveld refinement using TOPAS of synchrotron powder X-ray diffraction data of Mg-herbertsmithite, γ-$Cu_{4-x}Mg_x(OH)_6Cl_2$ sample **5**, at $T = 295$ K and using X-rays of wavelength $\lambda = 0.412260$ Å. The blue, red, and lower gray lines represent the collected data, fit, and difference plots respectively. The tick marks show reflection positions. The final goodness-of-fit merit factor, χ^2, was 2.138.

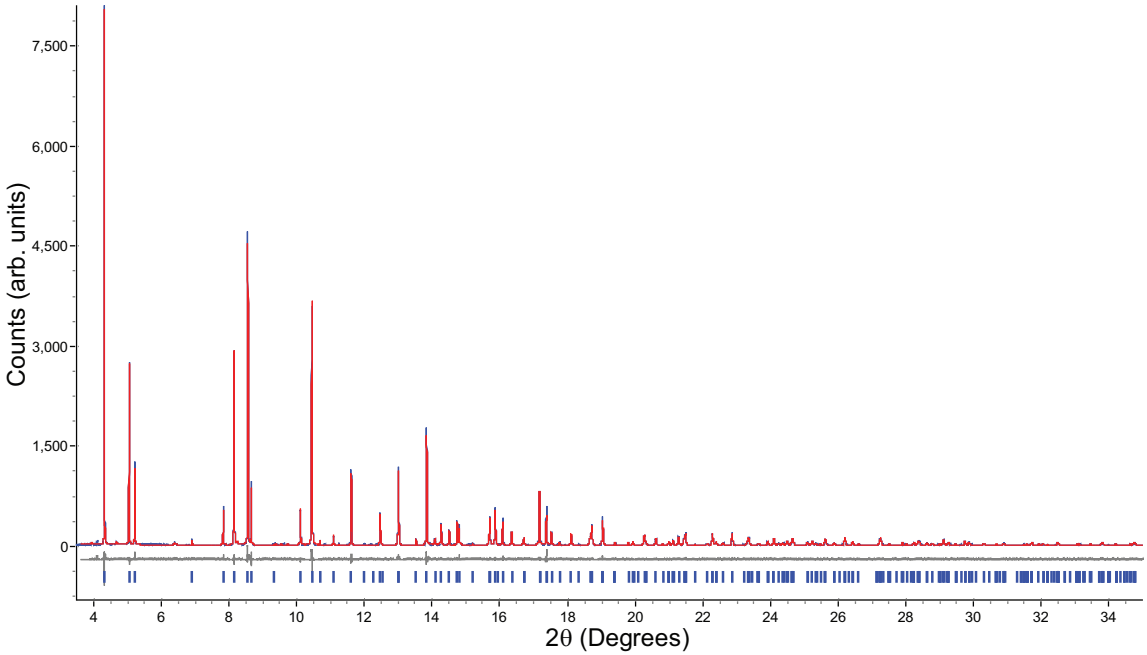

FIGURE A.6. Rietveld refinement using TOPAS of synchrotron powder X-ray diffraction data of Mg-herbertsmithite, γ-$Cu_{4-x}Mg_x(OH)_6Cl_2$ sample **6**, at $T = 295$ K and using X-rays of wavelength $\lambda = 0.412260$ Å. The blue, red, and lower gray lines represent the collected data, fit, and difference plots respectively. The tick marks show reflection positions. The final goodness-of-fit merit factor, χ^2, was 1.849.

APPENDIX B

Refined crystallographic parameters for 'Mg-herbertsmithite' samples discussed in chapter 3.

TABLE B.1. The crystallographic parameters for Mg-herbertsmithite, γ-$Cu_{4-x}Mg_x(OH)_6Cl_2$ sample **1** at $T = 295$ K, using X-rays of $\lambda = 0.412260$ Å. The refined lattice parameters are $a = b = 6.838230(11)$ Å, $c = 14.018570(29)$ Å in the hexagonal setting of the space group $R\ \bar{3}\ m$. The final goodness-of-fit merit factor, χ^2, was 2.449.

Wyckoff Site	Atom Name	x	y	z	Occupancy
$9d$	Cu, Mg	$\frac{1}{3}$	$\frac{1}{6}$	$\frac{1}{6}$	0.956(3), 0.044(3)
$3a$	Mg, Cu	0	0	0	0.803(1), 0.197(1)
$6c$	Cl	0	0	0.30511(4)	1
$18h$	O	0.1997(13)	0.3994(25)	0.0859(12)	1
$18h$	H	0.2021(11)	0.4043(21)	0.0870(10)	1

TABLE B.2. The crystallographic parameters for Mg-herbertsmithite, γ-$Cu_{4-x}Mg_x(OH)_6Cl_2$ sample **2** at $T = 295$ K, using X-rays of $\lambda = 0.412260$ Å. The refined lattice parameters are $a = b = 6.838861(11)$ Å, $c = 14.021250(27)$ Å in the hexagonal setting of the space group $R\ \bar{3}\ m$. The final goodness-of-fit merit factor, χ^2, was 2.228.

Wyckoff Site	Atom Name	x	y	z	Occupancy
$9d$	Cu, Mg	$\frac{1}{3}$	$\frac{1}{6}$	$\frac{1}{6}$	0.955(3), 0.045(3)
$3a$	Mg, Cu	0	0	0	0.827(9), 0.173(9)
$6c$	Cl	0	0	0.30483(4)	1
$18h$	O	0.12778(6)	0.25557(12)	0.10396(6)	1
$18h$	H	0.2021(11)	0.4043(21)	0.0870(10)	1

TABLE B.3. The crystallographic parameters for Mg-herbertsmithite, γ-$Cu_{4-x}Mg_x(OH)_6Cl_2$ sample **3** at T = 295 K, using X-rays of λ = 0.412260 Å. The refined lattice parameters are $a = b = 6.838819(11)$ Å, $c = 14.020101(29)$ Å in the hexagonal setting of the space group $R\ \bar{3}\ m$. The final goodness-of-fit merit factor, χ^2, was 2.080.

Wyckoff Site	Atom Name	x	y	z	Occupancy
9d	Cu, Mg	$\frac{1}{3}$	$\frac{1}{6}$	$\frac{1}{6}$	0.951(3), 0.049(3)
3a	Mg, Cu	0	0	0	0.820(1), 0.180(1)
6c	Cl	0	0	0.30501(4)	1
18h	O	0.12754(6)	0.25508(13)	0.10435(7)	1
18h	H	0.1954(11)	0.3909(22)	0.0904(11)	1

TABLE B.4. The crystallographic parameters for Mg-herbertsmithite, γ-$Cu_{4-x}Mg_x(OH)_6Cl_2$ sample **4** at T = 295 K, using X-rays of λ = 0.412260 Å. The refined lattice parameters are $a = b = 6.839350(12)$ Å, $c = 14.022080(30)$ Å in the hexagonal setting of the space group $R\ \bar{3}\ m$. The final goodness-of-fit merit factor, χ^2, was 2.206.

Wyckoff Site	Atom Name	x	y	z	Occupancy
9d	Cu, Mg	$\frac{1}{3}$	$\frac{1}{6}$	$\frac{1}{6}$	0.951(3), 0.049(3)
3a	Mg, Cu	0	0	0	0.821(9), 0.179(9)
6c	Cl	0	0	0.30480(4)	1
18h	O	0.12741(6)	0.25482(12)	0.10409(6)	1
18h	H	0.2019(10)	0.4038(21)	0.08524(99)	1

TABLE B.5. The crystallographic parameters for Mg-herbertsmithite, γ-$Cu_{4-x}Mg_x(OH)_6Cl_2$ sample **5** at T = 295 K, using X-rays of λ = 0.412260 Å. The refined lattice parameters are $a = b = 6.839584(10)$ Å, $c = 14.021205(28)$ Å in the hexagonal setting of the space group $R\ \bar{3}\ m$. The final goodness-of-fit merit factor, χ^2, was 2.138.

Wyckoff Site	Atom Name	x	y	z	Occupancy
9d	Cu, Mg	$\frac{1}{3}$	$\frac{1}{6}$	$\frac{1}{6}$	0.947(3), 0.053(3)
3a	Mg, Cu	0	0	0	0.815(9), 0.185(9)
6c	Cl	0	0	0.30483(4)	1
18h	O	0.12772(6)	0.25544(12)	0.10415(6)	1
18h	H	0.2034(10)	0.4068(20)	0.08551(97)	1

TABLE B.6. The crystallographic parameters for Mg-herbertsmithite, γ-$Cu_{4-x}Mg_x(OH)_6Cl_2$ sample **6** at T = 295 K, using X-rays of λ = 0.412260 Å. The refined lattice parameters are $a = b = 6.840730(16)$ Å, $c = 14.024902(40)$ Å in the hexagonal setting of the space group $R\ \bar{3}\ m$. The final goodness-of-fit merit factor, χ^2, was 1.849.

Wyckoff Site	Atom Name	x	y	z	Occupancy
9d	Cu, Mg	$\frac{1}{3}$	$\frac{1}{6}$	$\frac{1}{6}$	0.945(3), 0.055(3)
3a	Mg, Cu	0	0	0	0.819(1), 0.181(1)
6c	Cl	0	0	0.30467(4)	1
18h	O	0.12770(6)	0.2554(13)	0.10423(7)	1
18h	H	0.1979(11)	0.3959(23)	0.0882(11)	1

APPENDIX C

Curie-Weiss fits to inverse susceptibility data for the 'Mg-herbertsmithite' samples discussed in chapter 3.

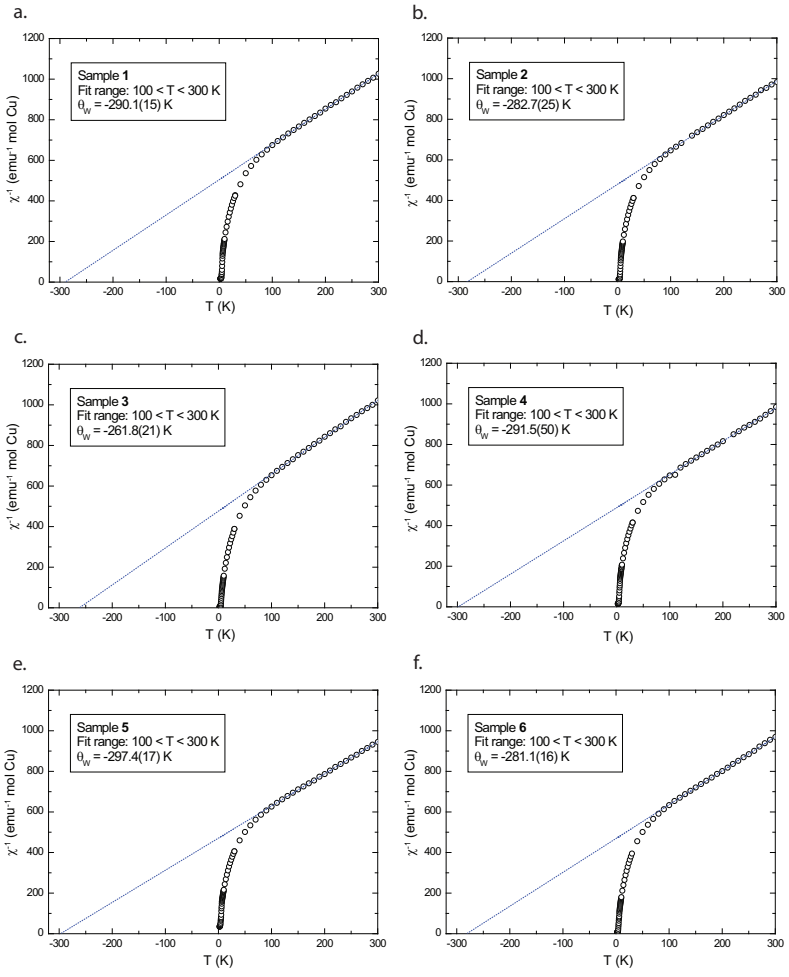

FIGURE C.1. Plots a–f show inverse susceptibility, χ^{-1} *vs.* temperature, T, measured in 100 Oe applied field. The dotted blue lines show fits of the Curie-Weiss law to the linear regions ($100 < T < 300$ K), affording estimates of the Weiss temperature, θ_W. The large negative Weiss temperatures indicate a strongly antiferromagnetic mean-exchange field in all samples.

APPENDIX D

Brillouin function fits to 2 K hysteresis data for the 'Mg-herbertsmithite' samples discussed in chapter 3.

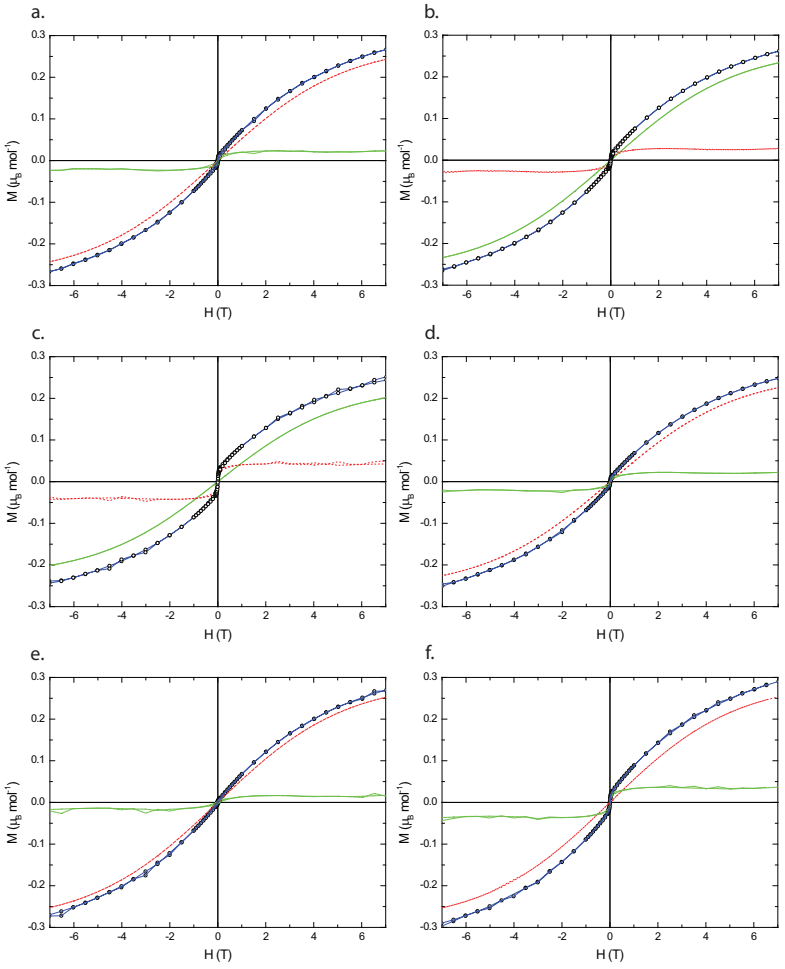

FIGURE D.1. Plots of M *vs.* H at $T = 2$ K show curvature that can be decomposed into two components; A dominant, paramagnetic-like, curvature, fitted with a Brillouin function, $B_f(x)$; and a saturating, weakly-ferromagnetic component, that can then be extracted. This treatment was repeated for all samples **1**–**6** affording plots a–f respectively. In all plots, the ∘ represents the measured data; the red dashed line is the fitted paramagnetic-like component; the green dotted line is the extracted ferromagnetic-like component; and the blue line is the sum of the two components, giving excellent agreement with the data in all samples.